X-RAY CRYSTALLOGRAPHIC STUDIES OF CYTOCHROME *C* OXIDASE FROM *RHODOBACTER SPHAEROIDES*

By

Ling Qin

A DISSERTATION

Submitted to
Michigan State University
in partial fulfillment of the requirement
for the degree of

DOCTOR OF PHILOSOPHY

Department of Biochemistry and Molecular Biology

2005

ABSTRACT

X-RAY CRYSTALLOGRAPHIC STUDIES OF CYTOCHROME *C* OXIDASE FROM *RHODOBACTER SPHAEROIDES*

By

Ling Qin

Cytochrome *c* oxidase (C*c*O) catalyzes the final reaction of aerobic respiration by accepting electrons from its immediate donor, cytochrome *c*, and passing them onto oxygen to form water. It also translocates protons from the inside of the mitochondrial inner membrane of eukaryotes or the periplasmic membrane of prokaryotes to the outside. The proton gradient formed across the membrane is utilized by ATP synthase to make ATP, a universal energy source. Efforts were directed toward developing the methodology of protein production, purification and crystallization in order to reproducibly obtain crystals of cytochrome *c* oxidase from *Rhodobacter sphaeroides* (*Rs*C*c*O), a bacterial homologue of the mammalian enzyme. High resolution structures are needed for progress in understanding the proton pumping mechanism.

By molecular engineering of various strain of *Rhodobacter sphaeroides* (*R. s.*) with different forms of subunits and histidine tag positions, modifying detergent solublization and protein purification protocols, and exploring different crystallization and cryocooling conditions, crystals of the four subunit *Rs*C*c*O were obtained and the crystal structure was solved to 2.9 Å resolution. A new form of the crystal containing the catalytic core of the oxidase, subunits I and II, was also obtained with isotropic

X-ray diffraction to 2.35 Å resolution from an *R. s.* strain with a C-terminal histidine tag on a shortened subunit II, and a short homogeneous version of subunit IV. The re-dissolved I-II subunit crystals were highly active, had native spectral characteristics, and displayed "suicide inactivation" during steady state turnover as previously observed for cytochrome *c* oxidase without subunit III. In the I-II subunit *Rs*C*c*O structure, the histidine tag attached to subunit II was found to chelate cadmium and contribute to strong crystal contacts. The crystal structure clearly revealed the presence of the previously observed covalent bond between the side chain ring atoms of $H284_I$ and $Y288_I$ close to the active site of the enzyme. In both crystal forms, a cadmium binding site was found at the matrix side of the enzyme at the suggested entrance for K-pathway for proton uptake, which could contribute to the observed inhibitory effect of zinc/cadmium on detergent-solublized enzyme. Detergents, detergent headgroups, and alkyl chains of detergents or lipids were also observed in the crystal structure of I-II subunit *Rs*C*c*O. The detergent sugar head groups are associated with aromatic residues in a manner similar to phospholipid head groups. Comparison to other C*c*O crystal structures reveals that alkyl chain positions of membrane lipids and detergent substitutes are conserved, suggesting their importance for obtaining well-ordered crystals. The method developed is readily reproducible and should be applicable to crystallizing other forms and key site-directed mutants of *Rs*C*c*O, whose high resolution crystal structures will benefit our understanding of the mechanism of this critical energy conserving process.

ACKNOWLEDGEMENTS

First and foremost, I would like to express my sincere gratitude to my graduate advisor, Dr. Shelagh Ferguson-Miller, for her constant guidance and support. I am not only greatly benefiting from her wealth of knowledge and experience in the field of study, but also deeply inspired by her enthusiasm and determination in carrying out scientific research.

I am grateful to my graduate committee members, especially Dr. R. Michael Garavito for his constant education and guidance on everything from membrane protein chemistry to x-ray crystallography; and to Dr. James Geiger, Dr. William Smith and Dr. Honggao Yan, for their advice and support throughout my Ph. D. program.

I am also indebted to my present and past lab mates for their help and friendship. I thank Dr. Denise Mills and Dr. Carrie Hiser for their continuous help and insightful discussions on my research and for reading through my dissertation. Dr. Carrie Hiser also generated various strains of bacteria used in my dissertation research and performed most of the protein gels. I thank Dr. Martyn Sharpe, Dr. Bryan Schmidt and Dr. Yasmin Hilmi for their help and insightful discussions. Dr. Yasmin Hilmi taught me initially to do protein purification and crystallization and she also performed all the thin layer chromatography analysis of lipids of my samples. I thank my fellow graduate students Jun Yang, Namjoon Kim, Jian Liu, Xi Zhang, Shujuan Xu for their help and discussions. Xi Zhang did all the mass spectrometry analyses of

various samples from me. Jian Liu helped me with freezing crystals prior to synchrotron trips and assisted me at synchrotron facility. I also thank all the past and present undergraduate students who have helped me growing bacteria, making reagents, and preparing cell membranes, particularly, Sarah House, Jamie Slater, Robert Bauman, Matt Hawkins, Steve Kidd, and Sarah Cloutier.

I am also deeply thankful to past and present members of the Garavito Lab in the BMB Department: Dr. Anne Mulichak for her help and education from crystallization, freezing crystals, and data collection to structural refinement; Dr. Rachel Powers, Christine Harman, Nicole Webb for their help and discussions on crystallization, data collection and structural refinement.

I would also like to thank Dr. Kaillathe Padmanabhan (Pappan) for sharing his insights on crystallography and structural refinement with me and helping me with computer hardware and software problems.

I am also indebted to Dr. Margareta Svensson-Ek and Dr. So Iwata, both of whom were at Uppsala University, Sweden, for their training on crystallization of cytochrome *c* oxidase and for their great hospitality when I was visiting them.

I thank staff scientists at LS-CAT, DND-CAT, and SBC-CAT at Advanced Photon Source, Argonne National Laboratory, particularly Dr. Joseph S. Brunzelle and Dr. Zdzislaw Wawrzak for their training, support and helpful suggestions on data collections.

And finally, I thank my parents and other family members for their support, encouragement, and unconditioned love throughout these years.

TABLE OF CONTENTS

LIST OF TABLES

LIST OF FIGURES

ABBREVIATIONS

aa	amino acid
ATP	adenosine triphosphate
A. U.	asymmetric unit
BSA	bovine serum albumin
C*c*O	cytochrome *c* oxidase
CDL	cardiolipin, diphosphatidylglycerol
CMC	critical micelle concentration
DEAE	diethylaminoethyl
EDTA	ethylenediaminetetraacetic acid
ESI	electrospray ionization
$FADH_2$	reduced form of flavin adenine dinucleotide
FPLC	fast protein liquid chromatography
ICP	inductively coupled plasma emission spectroscopy
kD	kilodalton
MALDI	matrix-assisted laser desorption ionization mass spectrometry
MES	2-(N-morpholino)ethanesulfonic acid
MW	molecular weight
NADH	reduced form of nicotinamide adenine dinucleotide
Ni-NTA	nickel-nitrilotriacetic acid
P. d.	*Paracoccus denitrificans*

PC	phosphatidyl choline
PDC	protein-detergent complex
*Pd*C*c*O	cytochrome *c* oxidase from *Paracoccus denitrificans*
PE	phosphatidyl ethanolamine
PEG-400	polyethylene glycol with an average molecular weight of 400
PG	phosphatidyl glycerol
PI	phosphatidyl inositol
PS	phosphatidyl serine
R. s.	*Rhodobacter sphaeroides*
ROS	reactive oxygen species
*Rs*C*c*O	cytochrome *c* oxidase from *Rhodobacter sphaeroides*
SDS-PAGE	sodium dodecyl sulfate polyacrylamide gel electrophoresis
SQDG	sulfoquinovosyl diacylglycerol
TOF	time of flight
Tris	tris(hydroxymethyl)-aminomethane
UCP	uncoupling protein

Chapter 1. INTRODUCTION

1.1 Structure and Mechanism of Cytochrome *c* Oxidase

1.1.1 Overall reaction

Cytochrome *c* oxidase (C*c*O) is found in both the mitochondrial inner membranes as well as the periplasmic membranes of many prokaryotes. It is the terminal enzyme in the electron transfer chain in eukaryotes and many bacteria that are capable of aerobic respiration. Figure 1.1 shows an overview picture of the respiratory chain. Electrons from food sources are transferred to complex I (NADH dehydrogenase) or complex II (succinate dehydrogenase) through NADH and $FADH_2$, respectively. These electrons are then transferred to complex III (cytochrome bc_1 complex) through coenzyme Q. Electrons are then transferred from complex III to a small soluble or membrane associated protein, cytochrome *c*, which in turn transfers them to complex IV (cytochrome *c* oxidase). Cytochrome *c* oxidase provides the final electron sink by accepting electrons from reduced cytochrome *c* and passing them onto oxygen to form water (for reviews, see Ferguson-Miller and Babcock, 1996; Michel *et al.*, 1998). It utilizes the energy generated from this exothermic reaction to translocate protons across the membrane against the membrane potential and pH gradient (Wikstrom, 1977). The proton gradient formed across the inner mitochondrial membrane or the bacterial periplasmic membrane is then utilized by ATP synthase to generate ATP, a universal energy source.

The overall reaction that cytochrome *c* oxidase catalyzes is:

$$4\ \text{cyt}\ c^{2+} + 8\ H^+_{(in)} + O_2 \rightarrow 4\ \text{cyt}\ c^{3+} + 2\ H_2O + 4\ H^+_{(out)}$$

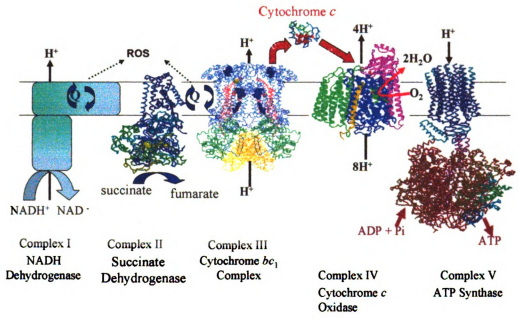

Figure 1.1: The mitochondrial respiratory chain complexes. The crystal structures of Complexes II, III, IV, V, and cytochrome *c* are shown (Bushnell *et al.*, 1990; Iwata *et al.*, 1998; Iverson *et al.*, 1999; Stock *et al.*, 1999; Svensson-Ek *et al.*, 2002). Complex I is shown in cartoon based on structure obtained by electron microscopy (Bottcher *et al.*, 2002). Electrons from food sources are transferred to Complex I or Complex II through NADH and $FADH_2$, respectively. These electrons are then transferred to complex III through coenzyme Q, and subsequently to cytochrome *c*. Cytochrome *c* then transfers the electrons to complex IV, which in turn transfers then to dioxygen to form water. Complexes I, III and IV are know to translocate protons across the inner mitochondrial membrane. The proton gradient formed across the inner mitochondrial membrane is then utilized by Complex V (ATP synthase) to generate ATP, a universal energy source. This figure is adapted from a figure courtesy of Dr. Denise Mills. Images in this dissertation are presented in color.

For each catalytic cycle, a total of eight protons are taken up from inside (N=negative side) of the membrane. Four of them combine with oxygen to form water while four others are pumped to the outside (P=positive side) of the protein.

C*c*O belongs to a superfamily of enzymes called heme/copper terminal oxidases because members of this family all have a conserved feature of having an iron-heme and a copper at the active site where oxygen is reduced. Besides using cytochrome *c* as an immediate electron transfer donor, some bacterial heme-copper terminal oxidases can utilize quinol as their substrate, such as cytochrome bo_3 quinol oxidase from *E. coli*. Some bacteria also have different types of C*c*Os based on the different heme groups involved in internal electron transfer. For example, C*c*O from *Thermus thermophilus* has a heme *b* and a heme a_3. *Rhodobacter sphaeroides* (*R. s.*) has several different types of C*c*Os including the aa_3 type, the cbb_3 type, and the caa_3 type. The aa_3 type C*c*O, which has a heme *a* and a heme a_3, is the one that is the most homologous to that found in the mitochondrial respiratory chain in eukaryotes.

Because of its importance in energy metabolism, defects in C*c*O have been found associated with a variety of diseased states, both neuromuscular and non-neuromuscular in childhood and adulthood such as Leigh Syndrome, Alzheimer's disease, and a variety of other diseases (for reviews, see Robinson, 2000; Borisov, 2002). Extensive work has been performed over the years to understand the enzymatic mechanism and regulation of C*c*O under physiological and pathological conditions.

C*c*O is a multi-subunit transmembrane protein complex. The number of subunits varies from 4 in many bacteria to 13 in mammalian mitochondria. However,

only subunits I, II, and III, all being transmembrane subunits, are highly conserved throughout the species. The rest of the subunits are likely to play regulatory roles in the higher organisms. We have been focusing on understanding the structure/function relationships of cytochrome *c* oxidase from *Rhodobacter sphaeroides* (*Rs*C*c*O), a four subunit bacterial enzyme, as a model to study its mammalian counterpart. *Rs*C*c*O is an excellent model to study the key function of electron transfer and proton pumping by allowing kinetic, spectroscopic, and site-directed mutational analysis, as well as other biochemical studies of C*c*O under different bacterial growth conditions and genetic backgrounds.

1.1.2 Current Understandings of the Structure/Function of C*c*O

The advent of several X-ray crystal structures from bovine heart and two different bacteria, *Paracoccus denitrificans* (*P. d.*) and *Rhodobacter sphaeroides*, together with extensive spectroscopic and functional analyses have greatly enhanced our understanding of the aa_3 type cytochrome *c* oxidase (Iwata *et al.*, 1995; Tsukihara *et al.*, 1995; Tsukihara *et al.*, 1996; Ostermeier *et al.*, 1997; Yoshikawa *et al.*, 1998; Svensson-Ek *et al.*, 2002). We now have a fairly detailed picture of the structure of this enzyme complex and also some of the functional aspects pertaining to its structure. However, the exact mechanism of proton transfer and its coupling to electron transfer is yet to be resolved.

1.1.2.1 Overall Structures of Subunits

Figure 1.2 shows the overall structure of the four subunit *Rhodobacter sphaeroides* cytochrome *c* oxidase (*Rs*C*c*O). Unless otherwise noted, all the amino

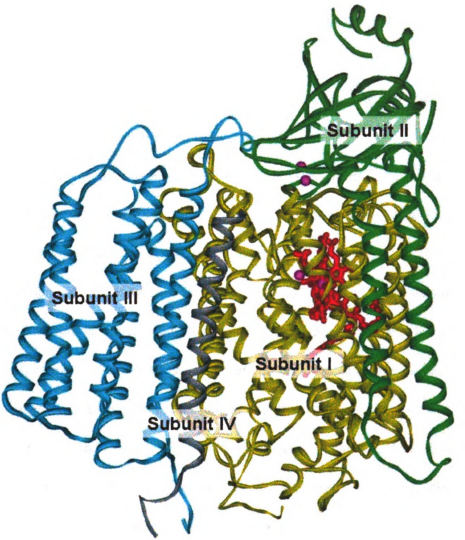

Figure 1.2: Overall structure of *Rs*C*c*O. The four subunits are labeled as shown in the figure. Subunit I is colored in yellow, subunit II in green, subunit III in cyan, and subunit IV is colored in gray. The heme groups and the redox active metal centers are colored in red and purple, respectively.

acid residues herein are labeled by *Rs*C*c*O numbering with the subunit number in subscript. The membrane portion of C*c*O has a trapezoidal shape in a view perpendicular to the membrane normal with an extra-membrane globular domain on the periplasmic side. Subunits I (yellow) and II (green) of *Rs*C*c*O are the core catalytic subunits for both electron transfer and proton pumping activities. All the redox active centers are located within these two subunits.

Subunit I is the largest and the most conserved subunit. It consists of 12 transmembrane helices roughly forming three 4-helix bundles in an anticlockwise sequence viewed from the periplasmic side. These helices provide the scaffold where prosthetic groups heme *a*, heme a_3, and Cu_B reside. Also located within subunit I are two proposed proton uptake channels. Figure 1.3 shows the metal centers in subunits I and II. The iron centers of the two heme groups, heme *a* and heme a_3, are buried approximately 15 Å from the periplasmic side of the membrane. The two porphyrin planes are perpendicular to the membrane plane with a highly conserved inter-porphyrin plane angle of approximately 104° with their propionates pointing to the periplasmic side of the membrane. The hydroxyethylfarnesyl tail of heme *a* extends downward and remains in the hydrophobic core between the transmembrane helices. On the other hand, the hydroxyethylfarnesyl tail of heme a_3 extends sideways and penetrates into the lipid bilayer, although the positions of the farnesyl tails are not highly conserved, unlike the angle of the hemes (Sharpe *et al.*, 2005). Heme *a* has a low spin iron with two conserved axial histidine ligands, $His102_I$ and $His421_I$. Heme a_3 has a high spin iron that is only five-coordinated, with only one conserved axial

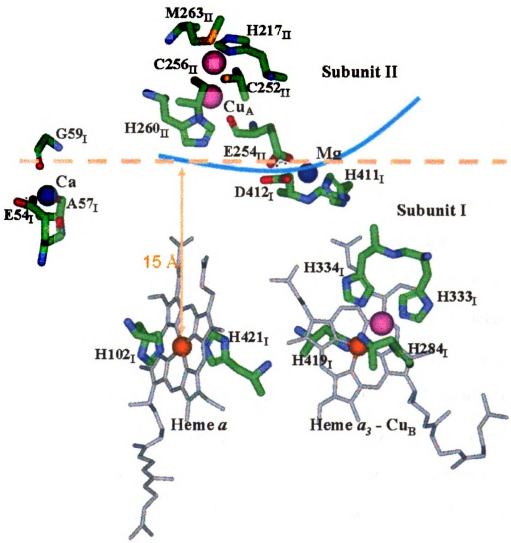

Figure 1.3: Hemes and metal centers in *Rs*C*c*O and their amino acid ligands. The heme groups are colored in gray and the amino acid ligands are colored by the atom types (C: green; O: red; N: blue; S: yellow). Iron, copper, magnesium, and calcium atoms are colored in red, purple, blue and bluish green, respectively. The membrane surface of the periplasmic membrane of *R. s.* is shown as orange dotted line and the interface between subunits I and II is represented by a light blue curve.

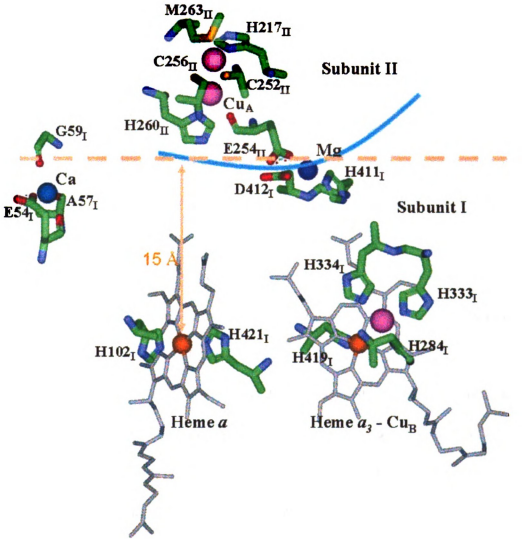

Figure 1.3: Hemes and metal centers in *Rs*CcO and their amino acid ligands. The heme groups are colored in gray and the amino acid ligands are colored by the atom types (C: green; O: red; N: blue; S: yellow). Iron, copper, magnesium, and calcium atoms are colored in red, purple, blue and bluish green, respectively. The membrane surface of the periplasmic membrane of *R. s.* is shown as orange dotted line and the interface between subunits I and II is represented by a light blue curve.

histidine, $His419_I$, which is ligated to the iron on the opposite side (distal side) of the heme a_3 to the Cu_B center. Due to lack of strong liganding interactions from the proximal side, the iron in heme a_3 is slightly out of the porphyrin plane toward the axial histidine. The Cu_B ion is approximately 4.9 – 5.1 Å away from the heme a_3 iron in the structures of C*c*O from different species (Harrenga and Michel, 1999; Svensson-Ek *et al.*, 2002; Tsukihara *et al.*, 2003). Together the Cu_B center and heme a_3 Fe form the binuclear center active site where oxygen binds and is reduced to water. Cu_B has three ligands, $His333_I$, $His334_I$, and $His284_I$. The latter is found to form an unusual covalent linkage to $Tyr288_I$ between the $N\varepsilon_2$ and $C\varepsilon_2$ atoms from the two residues, respectively (not shown in Figure 1.3) (Ostermeier *et al.*, 1997; Yoshikawa *et al.*, 1998; Buse *et al.*, 1999; Tomson *et al.*, 2002). X-ray crystallographic data also suggests that there are more bridging ligands in between the heme a_3 Fe and Cu_B. Different bridging ligands have been proposed including a peroxide (Yoshikawa *et al.*, 1998), or the more widely accepted bridging structure with one hydroxide bound to the Cu_B and a water ligated to the Fe ion of heme a_3 (Ostermeier *et al.*, 1997). The exact nature of the bridging ligand(s) in the X-ray crystal structure is unclear. Besides the heme groups and Cu_B center, subunit I also has a non-redox active calcium binding site in it and the role of the calcium ion is unknown. The ligating residues for the calcium ion include $Glu54_I$, $Ala57_I$, and $Gly59_I$ (Svensson-Ek *et al.*, 2002) (Figure 1.3).

Between subunits I and II, right above the heme a_3 propionate groups, an additional non-redox active metal ion, magnesium, is found in the structure (Figure

1.3). The magnesium binding site is highly conserved with $D412_I$ and $H411_I$ as its amino acid residue ligands and three very closely ligated water molecules in the crystal structure of *Rs*C*c*O (Svensson-Ek *et al.*, 2002). However, its role is not completely understood. It may be involved in stabilizing the interaction between subunit I and II and may have important functions in water exit (Florens *et al.*, 2001; Schmidt *et al.*, 2003).

Subunit II is composed of an N-terminal loop, two transmembrane helices that interact with subunit I and a C-terminal extra-membrane globular domain. X-ray crystal structures indicate that the extramembrane domain is mainly composed of a ten-stranded β-barrel in which the Cu_A center is located. The Cu_A center (Figure 1.3) is formed by two mixed valance copper ions ($Cu^{1.5+}$ - $Cu^{1.5+}$). The ligating residues for one copper are: $Cys252_{II}$, $Cys256_{II}$, $His217_{II}$, and $Met263_{II}$ and those for the other copper atom are: $Cys252_{II}$, $Cys256_{II}$, $His260_{II}$, and the carbonyl oxygen of $Glu254_{II}$. The two cysteines bridge the two copper atoms from two sides and the two sulfur atoms lie in the same plane as the copper atoms. The Cu_A center is the initial electron acceptor from cytochrome *c* (Ferguson-Miller and Babcock, 1996; Malatesta *et al.*, 1998). In *Rs*C*c*O, the polypeptide chain of subunit II has been known to undergo proteolytic cleavage events during its maturation process. As a result, the signal peptide of the N-terminal 25 amino acids from the full length subunit II gene product is completely removed (Steinrucke *et al.*, 1987). Moreover, there is incomplete proteolytic processing of the C-terminal 13 amino acids (Hiser *et al.*, 2001). The reason for this incomplete proteolytic cleavage is unknown and C*c*O containing

mostly the processed or unprocessed forms of subunit II seem to be equally functional (Hosler *et al.*, 1992; Zhen *et al.*, 1998).

Subunit III is also a highly conserved subunit. It is composed of seven helices and has an overall structure of two bundles of helices separated by a V-shaped cleft. It has no metal centers in it and its role is less well defined. Subunit III-less enzyme is highly active but the enzyme undergoes suicide inactivation during catalytic turnovers (Bratton *et al.*, 1999). Within the cleft of the V-shaped bundle, and the interface between subunits III and I, bound membrane lipid molecules are found in the crystal structures of bovine heart C*c*O, *Rs*C*c*O and *Pd*C*c*O (Figure 1.4).

Compared to subunit I, II, and III, subunit IV of C*c*O is not conserved among different species. Subunit IV from *Rs*C*c*O has only one transmembrane helix. Its existence in the *R. s.* enzyme was not known until the crystal structure was solved (Svensson-Ek *et al.*, 2002). As shown in Figure 1.4, subunit IV lacks direct contact in its transmembrane region with its neighboring protein subunits I and III and it associates itself with the enzyme complex via indirect contacts mediated through membrane lipid molecules as revealed by the crystal structure (Svensson-Ek *et al.*, 2002). The role of subunit IV remains unknown. The histidine-rich cytoplasmic portion of the polypeptide chain might be part of the proton collecting antenna system. However, genetic and biochemical studies of *Pd*C*c*O, whose protein sequence and structure are highly homologous to those of *Rs*C*c*O, showed no difference in enzymatic activity when the subunit IV gene was deleted (Witt and Ludwig, 1997). Preliminary experiments of *Rs*C*c*O lacking subunit IV also showed no effects on

mostly the processed or unprocessed forms of subunit II seem to be equally functional (Hosler *et al.*, 1992; Zhen *et al.*, 1998).

Subunit III is also a highly conserved subunit. It is composed of seven helices and has an overall structure of two bundles of helices separated by a V-shaped cleft. It has no metal centers in it and its role is less well defined. Subunit III-less enzyme is highly active but the enzyme undergoes suicide inactivation during catalytic turnovers (Bratton *et al.*, 1999). Within the cleft of the V-shaped bundle, and the interface between subunits III and I, bound membrane lipid molecules are found in the crystal structures of bovine heart C*c*O, *Rs*C*c*O and *Pd*C*c*O (Figure 1.4).

Compared to subunit I, II, and III, subunit IV of C*c*O is not conserved among different species. Subunit IV from *Rs*C*c*O has only one transmembrane helix. Its existence in the *R. s.* enzyme was not known until the crystal structure was solved (Svensson-Ek *et al.*, 2002). As shown in Figure 1.4, subunit IV lacks direct contact in its transmembrane region with its neighboring protein subunits I and III and it associates itself with the enzyme complex via indirect contacts mediated through membrane lipid molecules as revealed by the crystal structure (Svensson-Ek *et al.*, 2002). The role of subunit IV remains unknown. The histidine-rich cytoplasmic portion of the polypeptide chain might be part of the proton collecting antenna system. However, genetic and biochemical studies of *Pd*C*c*O, whose protein sequence and structure are highly homologous to those of *Rs*C*c*O, showed no difference in enzymatic activity when the subunit IV gene was deleted (Witt and Ludwig, 1997). Preliminary experiments of *Rs*C*c*O lacking subunit IV also showed no effects on

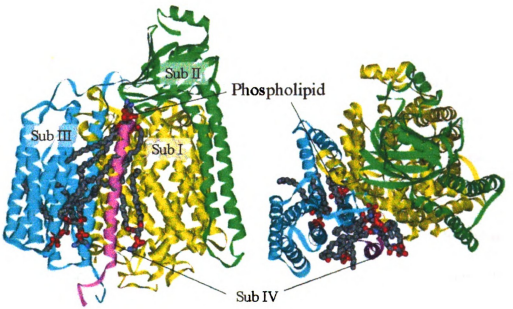

Figure 1.4: Membrane lipids resolved in the crystal structure of *Rs*CcO. The two figures represent a side view on the left and a top view on the right. A total of six phosphatidyl ethanolamine molecules were resolved in the crystal structure of *Rs*CcO. Four of them are found surrounding subunit IV and the other two are found within the V-shaped cleft formed by helix bundles inside subunit III and at the interface of subunit III and subunit I. Subunit IV associates itself with the enzyme complex via indirect contacts mediated through the membrane lipid molecules.

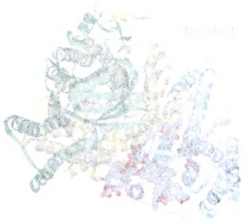

enzymatic activities (Hiser *et al.*, unpublished). However, a role in stability or regulation cannot be ruled out.

C*c*O from the bovine heart mitochondria has 13 subunits (Kadenbach *et al.*, 1983; Tsukihara *et al.*, 1996). The core subunits of I, II and III are encoded by the mitochondrial genes while the other ten subunits are nuclear encoded (Capaldi, 1990). The first three subunits from the bovine enzyme show very high structural homology to the first three subunits of bacterial enzyme as shown in Figure 1.5. The other ten subunits from the bovine enzyme include both transmembrane subunits and extramembrane subunits. The specific roles of these subunits are not well defined and they likely play roles in assembly and/or activity regulation. Subunit VIb binds a zinc ion of unknown function and one of the cholate binding sites on subunit VIa observed from crystal structure might indicate a possible nucleotide binding site for energy production regulation (Tsukihara *et al.*, 1996). Multiple binding sites of ATP/ADP on both core subunits and peripheral subunits were also suggested from biochemical studies of yeast and bovine C*c*O (Kadenbach, 1986; Napiwotzki *et al.*, 1997; Beauvoit and Rigoulet, 2001; Ludwig *et al.*, 2001).

1.1.2.2 Electron Transfer Pathways

The electron transfer pathway within the enzyme is understood in some detail. As shown in Figure 1.6, electrons are transferred from cytochrome *c* first to the Cu_A center, and in turn to heme *a*, then to the binuclear center, heme a_3 and Cu_B, where dioxygen binds and is reduced to water (Ferguson-Miller and Babcock, 1996; Michel *et al.*, 1998).

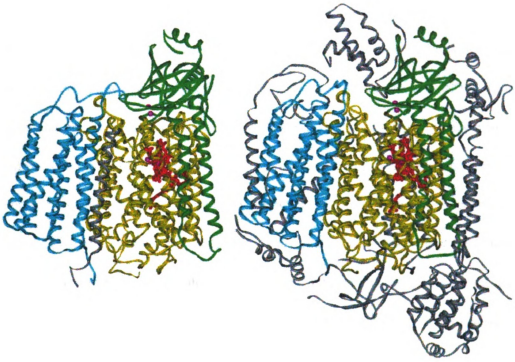

Figure 1.5: Comparison of *R. s.* and bovine mitochondrial CcO structures. The three core subunits I (yellow), II (green), and III (cyan) are highly homologous, as well as the redox active centers (hemes *a* and a_3 are shown in red, and coppers are shown in purple). The non-homologous subunits, including subunit IV of *Rs*CcO and the additional 10 subunits from bovine CcO are shown in gray.

There are two cytochromes *c* in *R. s.* that have been considered as substrates for C*c*O: cytochrome c_y, which is membrane anchored and cytochrome c_2, which is a soluble, mobile protein. Both cytochromes *c* are capable of accepting one electron from the cytochrome bc_1 complex (complex III) and donating it to C*c*O, but a variety of considerations suggest that cytochrome c_y is the physiological electron donor to the aa_3-type cytochrome *c* oxidase (Daldal *et al.*, 2001; Daldal *et al.*, 2003). From molecular modeling using horse heart cytochrome *c*, the binding site for cytochrome *c* is proposed to be on the outside of the membrane on a concave surface created by the globular domain of subunit II and the adjacent flat surface of subunit I (Roberts and Pique, 1999; Flock and Helms, 2002; Maneg *et al.*, 2004). The binding of horse heart cytochrome *c* to C*c*O is basically through electrostatic interactions between the two docking faces involving a number of positively charged residues from cytochrome *c* including Lys8, Lys13, Lys86 and Lys87 and negatively charged residues from subunit II of *Rs*C*c*O including $Glu157_{II}$, $Glu148_{II}$, $Asp195_{II}$, and $Asp214_{II}$, as proposed by protein docking studies (Roberts and Pique, 1999), as well as chemical modification studies of cytochrome *c* (Ferguson-Miller *et al.*, 1978), and biochemical analyses of site-directed mutants of these residues (Ferguson-Miller *et al.*, 1978; Roberts and Pique, 1999; Wang *et al.*, 1999; Zhen *et al.*, 1999).

Modeling studies and biochemical analysis suggest that a highly conserved tryptophan residue in subunit II, $Trp143_{II}$ is the immediate electron acceptor from reduced cytochrome *c* as shown in Figure 1.6 (Witt *et al.*, 1998; Roberts and Pique, 1999; Wang *et al.*, 1999; Zhen *et al.*, 1999). In the C*c*O crystal structure, $Trp143_{II}$ is

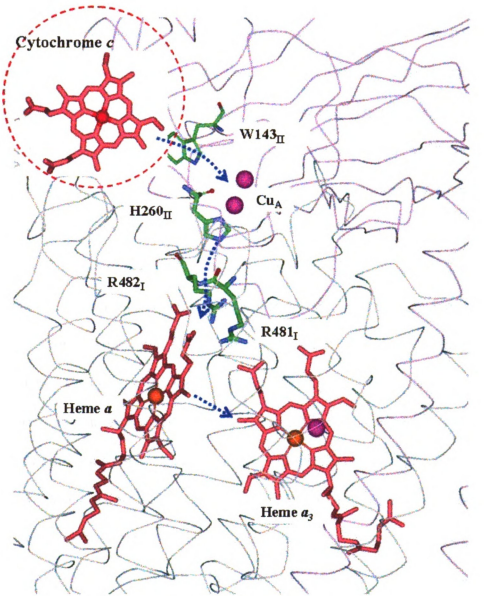

Figure 1.6: Electron transfer pathways in CcO. Cytochrome *c* is represented by a red dotted circle. The heme *c* from cytochrome *c* and heme *a* and a_3 from CcO are shown in red and the copper atoms are shown in purple. The electron transfer pathway is shown as blue dotted arrows.

within van der Waals contact distance to the Cu_A center ligands and the computer docking model also shows its proximity to the heme ring of docked cytochrome *c*. Phenylalanine and alanine mutants of the $Trp143_{II}$ residue reduce the electron transfer rate by 450 and 1200 folds, respectively, while having no effects on the dissociation constant between cytochrome *c* and C*c*O, nor do these mutants affect the Cu_A site (Wang *et al.*, 1999; Zhen *et al.*, 1999). These studies suggest that the indole ring of $Trp143_{II}$ is most likely the conduit of electrons from the heme group in cytochrome *c* to the Cu_A center in the extramembrane domain of C*c*O.

The Cu_A center is located in the extramembrane domain of subunit II and is composed of two mixed-valence copper ions. It transports electrons to heme *a* in subunit I at an extremely fast rate of approximately 2.3×10^4 s^{-1} in bovine heart mitochondrial C*c*O (Pan *et al.*, 1993) and 9×10^4 s^{-1} in *Rs*C*c*O (Wang *et al.*, 1999), considering the distance between the Cu_A center and the Fe in heme *a* of 19 Å and the driving force of just 50 meV (Tsukihara *et al.*, 1995; Winkler *et al.*, 1995). One of the proposed major electron transfer (tunneling) pathways between the Cu_A dinuclear center and heme *a* is composed of 14 covalent bonds and two hydrogen bonds. It starts with a hydrogen bond between Cu_A ligand $His260_{II}$ and a carbonyl group of the peptide bond joining two highly conserved arginine residues, $Arg481_I$ and $Arg482_I$, and then through $Arg482_I$ to one of the propionate groups in heme *a* (Iwata *et al.*, 1995; Ramirez *et al.*, 1995; Regan *et al.*, 1998; Tan *et al.*, 2004). The importance of the residues along the pathway is supported by site-directed mutants $H260_{II}N$ and $R482_IP$, which show an approximately 2000 fold slower electron transfer rate between

Cu

me

be

Alt

tha

bet

19

cou

and

hem

betw

since

appr

Harr

al.,

throu

Fe at

1.1.2.

under

Figure

Cu_A and heme *a*, which cannot be accounted for by altered redox potentials of the metal centers (Wang *et al.*, 2002; Zhen *et al.*, 2002; Qian *et al.*, 2004). The result can be interpreted to support the concept of a "through bond" pathway of electron transfer. Although the distance between Cu_A and the heme a_3 is only about 1.5 Å longer than that between Cu_A and heme *a*, evidence for significant rates of electron transfer between Cu_A and heme a_3-Cu_B binuclear center has not been found (Regan *et al.*, 1998).

Electrons transported from heme *a* to the heme a_3 Fe - Cu_B binuclear center could utilize either of the two different proposed pathways that connect heme *a* Fe and heme a_3 Fe: the closely approaching heme edges, or the histidine ligands to each heme connected through helix VIII (Regan *et al.*, 1998). The direct electron transfer between the two heme porphyrin rings would occur through "edge to edge" transfer since the closest edge to edge distance between the two heme groups is only approximately 4.6 – 5.2 Å in C*c*O from different organisms (Ostermeier *et al.*, 1997; Harrenga and Michel, 1999; Svensson-Ek *et al.*, 2002; Tsukihara *et al.*, 2003; Tan *et al.*, 2004). The center-to-center transfer via the histidine ligands involves some through space jumps and a distance of approximately 13.5 Å between the two heme Fe atoms.

1.1.2.3 Oxygen Chemistry

Spectroscopic and fast kinetic measurements have contributed to our understanding of the chemistry behind the dioxygen reduction reaction as shown in Figure 1.7 (Michel *et al.*, 1998; Zaslavsky and Gennis, 2000; Kim *et al.*, 2004). In this

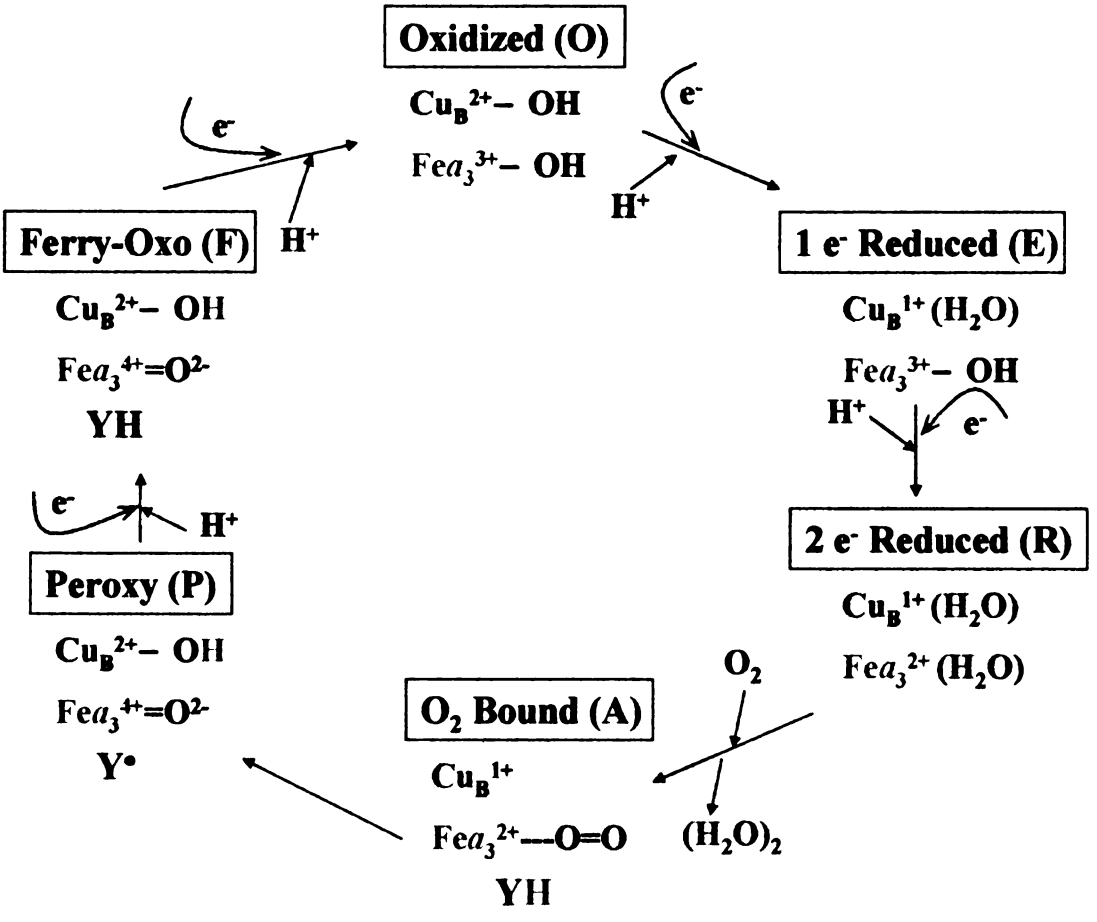

Figure 1.7: The oxygen chemistry cycle of reaction catalyzed by CcO. For each catalytic cycle, four electrons are transferred to the binuclear center and combined with dioxygen and four protons taken from the inside of the membrane to form 2 waters. The four additional protons translocate across the membrane are not shown in the figure since the proton pumping mechanism is unknown.

scheme, the oxidized form of enzyme (usually called intermediate O) has a hydroxyl bound to both heme a_3 and Cu_B. The first electron that enters C*c*O through the electron transfer pathway is expected to go to Cu_B of the binuclear center forming intermediate E, causing the conversion of its bound hydroxyl to water at the Cu_B site. A second electron is then transferred to heme a_3 forming intermediate R with another water formed at heme a_3. The doubly reduced binuclear center can then bind oxygen forming intermediate A. The oxygen bond is rapidly cleaved by a four electron transfer event using two electrons from the heme a_3 to form a ferryl-oxo and one electron from Cu_B to form a cuprous hydroxide, as well as an electron and proton from a nearby $Tyr288_I$ (MacMillan *et al.*, 1999). This state is referred to as the P (peroxy) intermediate even though all evidence indicates that the peroxy form is not present. A third electron is injected and it reduces the $Tyr288_I$ free radical back to its stable state, forming intermediate F with concomitant uptake of a proton. Finally, a fourth electron is injected with accompanying proton to convert the enzyme from the Fe^{4+} ferryl intermediate to its Fe^{3+} oxidized state, with a hydroxyl on both heme a_3 and Cu_B. How and when vectorial translocation of protons occurs during this catalytic cycle is unclear and under debate. Proton pumping is proposed by some to occur during the oxygen reduction cycle (Vygodina *et al.*, 1997), involving the P $\rightarrow$ F and F $\rightarrow$ O steps. Others proposed that one proton is likely to have been translocated before the formation of the P intermediate (Michel, 1999). Still others propose that proton pumping occurs during each one-electron step of reduction of the enzyme (Wikstrom and Verkhovsky, 2002; Tsukihara *et al.*, 2003). The proton pumping mechanism and

its coupling to electron transfer remains a subject of controversy.

1.1.2.4 Proton Uptake Pathways

For each catalytic cycle, four protons (substrate protons) are needed for the reduction of dioxygen to form water and another four protons (pumped protons) are translocated across the membrane to form the proton gradient needed to synthesize ATP (Wikstrom, 1977). Mutagenesis and the crystal structures of bacterial C*c*O reveal two important proton uptake pathways, D and K pathways, each named after a residue whose mutation blocks the pathway, $D132_I$ and $K362_I$, respectively (Fetter *et al.*, 1995; Iwata *et al.*, 1995; Svensson-Ek *et al.*, 2002). Figure 1.8 shows the two proton uptake pathways.

1.1.2.4.1 D Pathway

A chain of crystallographically resolved water molecules were identified in *Rs*C*c*O, which defined the D proton uptake pathway (Iwata *et al.*, 1995; Svensson-Ek *et al.*, 2002) (Figure 1.8). The waters are also seen in the bovine C*c*O crystal structure at 1.8 Å resolution (Tsukihara *et al.*, 2003). It starts with a highly conserved residue, $D132_I$, close to the inside of the bacterial cell membrane, and continues through several polar residues including $N121_I$, $N139_I$, $N207_I$, $S142_I$, $Y33_I$, $S201_I$, $S200_I$, $S197_I$, and onto $E286_I$. How proton transfer is achieved after $E286_I$ is unclear and currently under debate since there are no more waters found in the crystal structure in the hydrophobic cavity between $E286_I$ and the two heme groups. However, water is observed around the heme propionates and a chain of waters is seen to form in a molecular dynamics simulation of *Rs*C*c*O (Cukier, 2004; Seibold *et al.*, 2005).

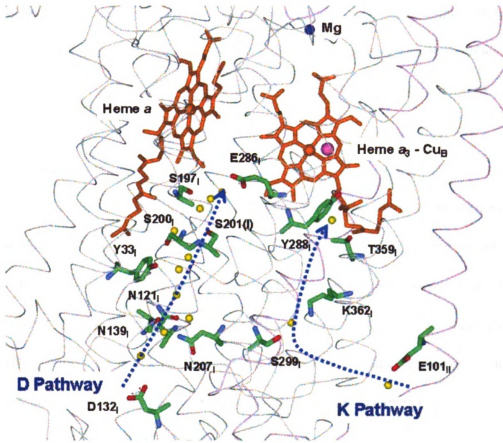

Figure 1.8: Two proton uptake pathways resolved in the crystal structure of *Rs*CcO. The D and K pathways are shown as blue dotted arrow and the crystallographically resolved waters in the two pathways are shown in yellow.

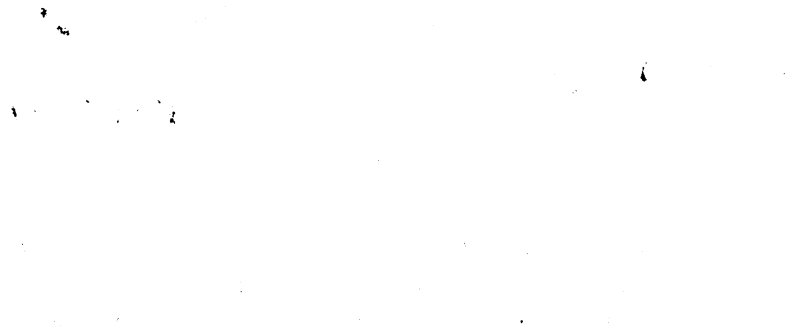

The D pathway is thought to conduct both pumped protons and substrate protons and $E286_I$ is suggested to be functioning as a valve through alternate conformations of its side chain to direct proton flow to either the proton exit pathway or the binuclear center active site (Konstantinov *et al.*, 1997; Hofacker and Schulten, 1998 ; but see Sharpe *et al.*, 2005).

1.1.2.4.2 K Pathway

The K pathway is considered to start with $E101_{II}$ and continue through $S299_I$, $K362_I$, and $T359_I$ up to the binuclear center via the hydroxyl of $Y288_I$ that is hydrogen bonded to the farnesyl hydroxyl of heme a_3 (Branden *et al.*, 2002; Tomson *et al.*, 2003) (Figure 1.8); $Y288_I$ forms an unusual covalent bond with one of the Cu_B ligands, $H284_I$, between the $C\varepsilon_2$ and $N\varepsilon_2$ atoms from the two residues, respectively. Such a covalent linkage was proposed from the crystal structure (Ostermeier *et al.*, 1997) and verified by other high resolution crystal structure (Yoshikawa *et al.*, 1998), and received further experimental verification by mass spectrometry (Ostermeier *et al.*, 1997; Yoshikawa *et al.*, 1998; Buse *et al.*, 1999). The K pathway is believed to transport substrate protons to the active site as shown by the extremely low activity of the $K362_I$ mutants, and relatively low activity of $S299_I$ and $T359_I$ mutants, as well as the observation that impairment in proton uptake could not be compensated by uptake of protons from the outside. In contrast, the activity of the D pathway mutant $D132_I A$ can be significantly enhanced by protons supplied from the outside in he presence of a membrane potential (the controlled state) where the wild type enzyme activity is inhibited (Fetter *et al.*, 1995; Mills *et al.*, 2000). This lack of enhancement of activity

in the K path mutants suggests that the K pathway is exclusively used for substrate proton uptake and not connected to the external surface via any reversible proton path. However, the observation that the $K362_{I}M$ mutant has a much higher activity with H_2O_2 as substrate indicates that the D pathway might also be involved in providing substrate protons (Konstantinov *et al.*, 1997). Yet it remains unclear which and how many of the four required substrate protons are supplied by each pathway, and when and how these protons are used in the oxygen reduction reaction, a central issue in understanding the coupling of proton pumping and electron transfer.

1.1.2.4.3 H Pathway in Bovine Heart Mitochondrial *Cc*O

Besides the D and K pathways, an H pathway, which connects the mitochondrial matrix side of the membrane to the outside, was defined and proposed to be exclusively for pumped proton uptake based on the high-resolution crystal structure of bovine heart mitochondrial *Cc*O and an altered conformation in the oxidized versus the reduced enzyme structure (Tsukihara *et al.*, 1996; Yoshikawa *et al.*, 1998). However, some of the essential residues along this pathway are not conserved in bacterial *Cc*Os and mutations of the equivalent residues have little or no effect on the activity of *Rs*C*c*O, indicating that the H pathway is not likely to be a universal proton uptake pathway conserved across the different species (Lee *et al.*, 2000).

1.1.2.5 Oxygen Pathway

One of the substrates of the enzyme, dioxygen must be accessible to the binuclear center. Since dioxygen is nonpolar, oxygen could simply reach the active

site through diffusion in the hydrophobic regions of the enzyme and perhaps a defined oxygen pathway is not completely necessary. However, three proposed specific oxygen pathways were defined in the bovine enzyme based on the crystal structure (Tsukihara *et al.*, 1996). In one of them, which is supported by molecular dynamics studies, oxygen is proposed to reach the binuclear center through a hydrophobic hole connecting from the V-shaped cleft formed by helices of subunit III, through subunit I to the binuclear center active site (Hofacker and Schulten, 1998). Based on the positions of the xenon atoms resolved in the structure of *Rs*C*c*O crystal pre-pressurized with xenon, an alternative oxygen pathway was proposed which accessed the binuclear center through subunit I between two transmembrane helices (Svensson-Ek *et al.*, 2002).

1.1.2.6 Proton and Water Exit Pathway

One possibility for the proton exit is that protons transported through the D pathway are picked up by $E286_I$. Via conformation movement of $E286_I$ and water chain formation, protons could be moved to the vicinity of the D-ring propionate group of heme a_3 (Hofacker and Schulten, 1998; Cukier, 2004). The latter is connected to the bulk phase through several hydrogen-bonded water networks. However, it is not clear whether there is a specific proton exit path, nor if the route is through the active site or via the $E286_I$/propionate connection.

It is argued that product water can simply randomly diffuse out of the protein and a specific water exit pathway is not necessary. However, this is not likely to be the case because water can serve as a pathway for proton movement, and random

diffusion of product water would potentially short-circuit the C*c*O system which requires unidirectional movement of electrons and protons. A water exit path was first proposed in the crystal structure of bovine C*c*O that involved the non-redox active Mg center right above the active site at the interface of subunit I and II (Tsukihara *et al.*, 1996). Evidence from ESEEM studies of the enzyme with Mn substituted at this Mg site using ^{17}O and $H_2{}^{17}O$ indicates that the Mn site is rapidly accessed by water from the outside and, importantly, water produced at the active site arguing for a discrete pathway rather than exit by random diffusion (Schmidt *et al.*, 2003).

1.1.2.7 Proton Pumping Theories and Coupling of Electron Transfer and Proton Translocation

Although the structure of C*c*O is well defined and the oxygen chemistry is now fairly clear, this has not led to a resolution of the question of how proton pumping occurs. A number of different proton pumping models have been proposed, but most are difficult to test. Currently no single model is supported by compelling experimental evidence. Proton pumping theories are generally grouped into direct coupling and indirect coupling mechanisms. However a combination of both is possible.

In a direct coupling mechanism, change of redox state of the metal center facilitates proton uptake and release from one of the active site ligands. A prototype "ligand-exchange" model proposed by Chan and colleagues involved ligand exchange upon reduction of Cu_A, leading to a proton release from one of its cysteine ligands (Larsen *et al.*, 1992). This is an example of a redox-coupled pumping mechanism that

has been discounted because of the ability of C*c*O without Cu_A to pump, and mutants of the Cu_A site to retain pumping activity (Zhen *et al.*, 2002). Another example of a direct coupling mechanism, that involves changes at the active site, is the histidine cycle model proposed first by Wikstrom and colleagues (Wikstrom *et al.*, 1994). Similar to the histidine cycle model, the histidine shuttle model was elaborated by Michel and colleagues. It suggests that one of the Cu_B ligands, $His333_I$, undergoes cycles of protonation states and swings between ligated and unligated conformations (Ostermeier *et al.*, 1995). However, later crystal structures suggested that there was no Cu_B ligand change upon reduction, lessening the interest in the histidine shuttle model (Harrenga and Michel, 1999).

In an indirect coupling mechanism, oxygen chemistry or redox changes are coupled to a structural change a distance away from the active site which leads to proton movement and finally proton pumping. Based on the high resolution crystal structures observed for oxidized and reduced bovine C*c*O, a residue $D51_I$ (bovine numbering) at the top of the proposed H channel was suggested to be involved in proton pumping (Yoshikawa *et al.*, 1998). In the oxidized state of enzyme, $D51_I$ is buried under the protein surface and connected to the matrix side via a hydrogen bonded network and internal water pools. Its conformation changes upon reduction of the enzyme, leading to exposure of its protonated carboxyl oxygen to the outer surface to release a proton (Yoshikawa *et al.*, 1998). Such a proton pumping mechanism bypasses the binuclear center and is proposed to be driven by heme *a* redox changes (Tsukihara *et al.*, 2003). However, the residue $D51_I$ is not conserved in bacterial

enzymes. Another indirect coupling model originally proposed by Rich and colleagues (Rich *et al.*, 1996) states that charge neutralization is the driving force for proton uptake from the inside, such that when an electron moves to a redox active site, a proton moves to the vicinity to neutralize the negative charge. However, the pumped protons are not bound directly to the metal center ligands and follow a path that is separate from the binuclear center.

Recently the importance of $E286_I$ at the end of the partially defined D pathway is getting much attention. Molecular dynamics simulations suggest that $E286_I$ can deliver a proton via water chain formation to the binuclear center or to the heme a_3 propionate group by alternating its side chain conformation (Hofacker and Schulten, 1998; Cukier, 2004). The flipped conformation of $E286_I$, in which the carboxyl oxygen is closer to the D ring propionate of heme a_3, is proposed to be stabilized by two water molecules originally located at the active site (Hofacker and Schulten, 1998), or by other residue and water movements in the vicinity (Seibold *et al.*, 2005).

In a recently proposed model from our research group (Sharpe *et al.*, 2005), the $H284_I$–$Y288_I$ covalent pair is suggested to go through cycles of ligation and deligation of Cu_B in response to changes in charge and ligand state of the copper. The rotation of its imidazole-tyrosine rings leads to alternate opening and closing of the K pathway. Protons move into this site from the D and K pathways, depending on the Cu_B ligating state and the charge present in the binuclear center. They are transported either to the active site to form water or to a conserved water molecule bound between

the propionates of heme a_3, via the histidine ligands of Cu_B. The latter proton is released to the outside of the membrane. This is a new version of the histidine cycle model which is yet to be tested by experimental analysis.

1.1.2.8 Function of Subunit III of *Cc*O

Although subunits I, II and III are highly conserved throughout the species, only subunits I and II contain the redox active centers and are required for both electron transfer and proton pumping functions. The exact function of subunit III is not completely understood and is being studied using subunit III-less enzyme. Subunit III-less *Cc*O can be prepared by Triton X-100 detergent treatment after enzyme purification or by genetically removing the subunit III gene (Mills *et al.*, 2003). Although the initial activity and stability of subunit III-less enzyme is similar to that of the four subunit holoenzyme, subunit III-less *Cc*O undergoes spontaneous and irreversible inactivation (suicide inactivation) during steady state turnover (Bratton *et al.*, 1999). The mechanism of suicide inactivation is apparently not due to the production of reactive oxygen species since adding catalase and superoxide dismutase had no effect on the rate of inactivation (Bratton *et al.*, 1999). Suicide inactivation is ultimately associated with the loss of Cu_B at the heme a_3-Cu_B binuclear center as measured by EPR spectroscopy and metal analysis, possibly due to the dissociation of one or more of Cu_B's ligands (Hosler, 2004).

It was also found that the rate of proton uptake through the D pathway, as well as the proton exit/back flow pathway, was slowed down in the absence of subunit III (Gilderson *et al.*, 2003; Mills *et al.*, 2003). A similar inactivating effect was observed

for mutants that affect the D pathway, such as $D132_IA$, but not for K the pathway mutant $T359_IA$. A severe inactivating effect on CcO was observed for a double mutant $D132_IA/R481_IK$ even in the presence of subunit III. On the other hand, arachidonic acid, which enhances the D pathway proton uptake, slows down the rate of inactivation of subunit III-less CcO. Therefore, the role of subunit III could be to maintain a conformation of CcO that facilitates proton flow to the active site through the D pathway and proton backflow through the exit path to the active site. The prolonged lifetime of the heme a_3 oxoferryl ($Fe^{4+}=O$) or a tyrosine radical intermediate, or the deprotonated form of $E286_I$ due to the slowed proton supply might be responsible for the observed suicide inactivation (Mills and Hosler, 2005).

1.1.3 Regulation of CcO Activity and Energy Metabolism

Mitochondria consume 85-90% of the total oxygen transported into the cells and generate most of the energy in the cell under aerobic conditions through the respiratory chain complexes. Cytochrome *c* oxidase and the general energy metabolism are constantly being regulated by different mechanisms. When there is an energy excess indicated by a higher membrane potential difference across the membrane, different uncoupling routes are triggered which lead to proton backleak across the membrane to dissipate the high membrane potential to prevent potential buildup of reactive oxygen species (ROS) (also see Figure 1.1 for where ROS are formed) which have been associated with mitochondrial damage and the aging process (Harper *et al.*, 2004). There exists a feedback loop between H^+ leak and ROS formation (Brookes, 2005). There are two types of uncoupling mechanisms, extrinsic

uncoupling and intrinsic uncoupling. Extrinsic uncoupling leads to increased proton leakiness across the membrane via various pathways, while intrinsic uncoupling lowers the proton pumping efficiency of respiratory chain complexes.

Extrinsic uncoupling is carried out through different types of uncoupling proteins. Uncoupling protein 1 (UCP1) is found in membranes of brown adipocytes and it serves as a fatty acid anion carrier that results in a net proton leak through the membrane to produce heat to maintain body temperature (Green and Brand, 2004). Other UCPs may have more complicated physiological functions including controlling the production of ROS and pathogenesis of type-2 diabetes (Green and Brand, 2004; Krauss *et al.*, 2005). Besides the leak mediated by specific proteins such as UCPs, the mitochondrial membrane itself may also be permeable for proton backleak, although there is evidence suggesting that this basal leak of H^+ is mediated via small molecules such as free fatty acids or superoxide species (Brookes, 2005).

The activity of C*c*O itself can be altered by a variety of small molecules, including nitric oxide (Antunes *et al.*, 2004), fatty acids (Sharpe *et al.*, 1996), thyroid hormones (Kadenbach and Arnold, 2000), zinc (Mills *et al.*, 2002), and by the direct energy indicator, the ATP/ADP ratio, although the exact bindings sites for nucleotides are still unclear (Kadenbach, 1986; Beauvoit and Rigoulet, 2001). Besides changes in the substrate binding affinity and in oxygen reduction activity, proton pumping efficiency as expressed by H^+/e^- stoichiometry is also regulated. There is evidence in C*c*O for a proton backflow pathway that allows protons to be taken up from the outside to support activity in the presence of a membrane potential, decreasing the

proton pumping efficiency (Mills *et al.*, 2002). This pathway could suppress formation of ROS. The backflow pathway has been proposed to be the reverse of the exit pathway for pumped protons. Zinc inhibition of C*c*O reconstituted into lipid vesicles in the presence of a membrane potential is proposed to be due to the blockage of the proton exit/backflow pathway (Mills *et al.*, 2002).

Although there have been enormous amounts of effort put into the understanding of the structure/function and regulation of C*c*O and great achievements have been made over the years, our collective knowledge of the enzyme, particularly in the underlying mechanism of the vectorial translocation of protons and how proton pumping is coordinated with electron transfer and oxygen reduction, is still quite limited (Mills and Ferguson-Miller, 2003). When the crystal structures of both bovine heart mitochondrial and *Pd*C*c*O came out simultaneously, it was predicted that only a few years' time would be needed for the proton pumping mechanisms to be solved. However, to date there seems to be more questions than answers. To address this central issue in bioenergetics, high resolution crystal structures are needed of various redox states and key mutants with altered biochemical properties in the proton pumping process. Towards this end, we have been trying to develop a reproducible method of obtaining crystals of *Rs*C*c*O, a bacterial homologue of the mammalian enzyme, that diffract X-rays to high resolution for further mechanistic studies.

1.2 Membrane Protein Crystallography

1.2.1 Overview of Macromolecular Crystallography

Structural information on biomacromolecules, such as proteins and nucleic acids, has been extremely helpful in our understanding of their function and regulation and has aided in rational drug designs to fight diseases. With the completion of various genomic sequencing projects, the need for structural information of the macromolecules has become more pressing in functional genomic projects. Of the different techniques, X-ray crystallography has been the most successful technique to date in solving the three-dimensional structure of macromolecules to atomic resolution.

X-rays have the wavelength of about 1 Å, which is close to the bond lengths in biomolecules. The diffraction of X-rays by the electron clouds of atoms from ordered molecules in a crystal can provide invaluable information about the structure of the biomolecule at atomic resolution. Our understanding of the structure/function relationships of the protein of interest often takes a leap with the advent of its high resolution crystal structure, as was the case in C*c*O from a few different sources (Iwata *et al.*, 1995; Tsukihara *et al.*, 1995; Tsukihara *et al.*, 1996; Ostermeier *et al.*, 1997; Svensson-Ek *et al.*, 2002).

It is estimated that a third of all open reading frames in the human genome encode for membrane proteins, including peripheral and integral membrane proteins. These proteins perform vital cellular functions such as energy metabolism, signal transduction, and material transport; thus, they are particularly important targets for

drug development. However, despite their abundance and importance in cellular functions, a mere 75 unique structures of membrane proteins had been deposited in the Protein Data Bank (PDB) by the end of 2003, compared with about 20,000 structures of water-soluble proteins (White, 2004). X-ray crystallography has been the major technique of obtaining 3-D structure of membrane proteins. Currently the most time-consuming step in successfully solving a membrane protein structure is the growth of a well-ordered membrane protein crystal, which can often take many years of effort.

1.2.2 Challenges in Membrane Protein Crystallography

1.2.2.1 Membrane Protein Production

The first step in membrane protein biochemistry and crystallography is to obtain the protein of interest in sufficient amount. However, this is often difficult because many membrane proteins are present at low levels in membranes, and expressing recombinant proteins in host cells such as *E. coli* often leads to severe problems such as protein precipitation and improper posttranslational modifications. Those membrane proteins that are naturally abundant in biological membranes such as enzymes involved in energy metabolic processes like photosynthesis and aerobic respiration were among the first ones whose structures were solved successfully, including C*c*O from bovine heart mitochondria and from the soil bacterium *Paracoccus denitrificans* (Iwata *et al.*, 1995; Tsukihara *et al.*, 1995). Therefore, the ability to produce high yields of membrane protein from the expression system is often crucial in obtaining a crystal structure successfully. Since a membrane protein

may undergo active posttranslational modification, such as glycosylation and proteolytic cleavage, efforts must be made to obtain a molecularly homogeneous form of the protein as a suitable candidate for crystallization. There is also accumulating evidence that the nature of the lipids that make up the membrane may be critical for expression and correct folding of membrane proteins (Dowhan *et al.*, 2004).

1.2.2.2 Membrane Protein-Detergent Complexes

In order to extract membrane proteins from the bilayer into aqueous solution, detergent molecules are needed to solubilize the proteins and therefore crystallization of a membrane protein is essentially crystallization of the membrane protein-detergent complex (PDC). Membrane protein molecules, once out of their native membrane bilayer, are often less stable due to loss of their native conformations. The search for a suitable detergent that can maximally retain a stable and homogeneous conformation of a particular membrane protein can be extremely time-consuming.

A detergent molecule is a small, amphipathic molecule with a hydrophilic headgroup and a hydrophobic tail which can interact with the transmembrane portion of a membrane protein (for reviews, see le Maire *et al.*, 2000; Garavito and Ferguson-Miller, 2001; Gohon and Popot, 2003). Detergent molecules are grouped into three classes depending on their biochemical features of their headgroups, namely, ionic, nonionic, and zwitteronic detergents. Detergents with nonionic sugar based headgroups, such as alkyl glucosides or alkyl maltoside, are often found to have relatively little denaturing effects on membrane proteins and therefore are often used in both membrane solublization and membrane protein crystallization. Zwitterionic

detergents, e.g. LDAO, have been successfully used in quite a few membrane protein crystallization experiments although they are considered to be more inactivating. Until now, there has not been a magic detergent which leads to universal success in membrane protein crystallization and the choice of detergent is usually by extensive screening. Moreover, it is very common that the detergent used in membrane solublizaton is different from what is used for crystallization trials.

Apart from the chemical composition of the detergent headgroup, the chain length of a detergent's hydrophobic tail is also of critical importance in membrane protein crystallization due to the difference in the interaction of the alkyl tail with the transmembrane portion of the protein as well as the effect on the overall size of the PDCs. During the crystallization experiments of *Pd*C*c*O, crystals were obtained in both dodecyl (C_{12}) maltoside and undecyl (C_{11}) maltoside detergents. Strikingly, the one carbon difference in chain length was responsible for a drastic difference in the X-ray diffraction limit of 8 Å using dodecyl maltoside compared to 2.5 Å using undecyl maltoside. Additionally, when decyl (C_{10}) maltoside was used, no crystals were obtained (Ostermeier *et al.*, 1997). Such strong dependence on chain length of alkyl tails of detergents has been reported in several other membrane protein crystallization experiments as well (Shinzawa-Itoh *et al.*, 1995; Marone *et al.*, 1999).

Detergent molecules are surfactants with their own particular phase behaviors. The most important one is the critical micelle concentration (CMC), above which detergent monomers tend to form into micelles and an increase in detergent concentration will only increase the micelle concentration with no change in the

detergent monomer concentration. In a detergent-solublized membrane protein solution, there exits a dynamic equilibrium between detergent monomers, detergent micelles and protein-detergent complexes. It is conceivable that too many detergent micelles in the crystallization mixture is bad for intermolecular contacts during crystal nucleation and growth, while insufficient detergent can lead to instability and rapid aggregation of membrane proteins. Therefore, the detergent concentration used in the crystallization mixture is of critical importance in obtaining highly ordered membrane protein crystals, and because the CMC of detergents is affected by protein, salts, and other crystallization reagents as well as the presence of other detergent(s), the entire system is very complicated and an exact optimal detergent concentration can only be worked out by repeated trial and error procedures.

Another important characteristic of detergents is the cloud point, where detergent molecules from a single phase solution partition into two immiscible phases, one detergent-rich and the other detergent-depleted, possibly due to the interactions between the detergent headgroups. The consolute boundary where such phase behavior occurs depends on temperature and the presence and concentration of crystallization reagents such as polyethylene glycol, salt, etc. Unwanted phase behavior in a crystallization solution can be detrimental to the crystallization efforts with membrane proteins, while attractive detergent micelle interactions can also be useful in membrane protein crystallization as some membrane protein crystals are formed under the conditions close to the consolute boundary of the detergent (Garavito and Picot, 1990).

Close to half a century and approximately 25,000 structures later, successful macromolecular crystallization to date still largely occurs through a process of trial and error. Although progress has been made in understanding the different theoretical aspects of crystallization in order to guide our practices, protein crystallization remains empirical with many variables that can affect crystal formation and X-ray diffraction quality, such as concentrations of protein sample and precipitating reagents, pH values, temperature, and exogenous crystallization additives, etc. When detergent is added into the system, the crystallization of membrane proteins (membrane protein-detergent complexes) involves several-fold more variables. Therefore, obtaining membrane protein crystals that diffract X-rays to high resolution is often a combination of hard work and serendipity.

1.2.3 Progress in Membrane Protein Crystallization

Since the first reported membrane protein crystal structure more than 20 years ago (Michel, 1982), a great amount of progress has been made in membrane protein crystallography which has produced many new high resolution crystal structures. Very high resolution (<2 Å) membrane protein structures have been obtained for a number of membrane proteins including bovine cytochrome *c* oxidase (Tsukihara *et al.*, 2003). Currently the membrane protein structure with the best resolution is the structure of the ammonia channel at 1.35 Å resolution (Khademi *et al.*, 2004). Besides extensive screening of detergents and other crystallization conditions, methods that can help increase the diffraction resolution of soluble protein crystals are also generally helpful in membrane protein crystallization. Micro- and macro-seeding (Fromme and Witt,

1998), crystal dehydration (Kuo *et al.*, 2003), heavy atom soak (Chang and Roth, 2001), and semi-directed mutagenesis of selected surface residues (Pautsch *et al.*, 1999) have all been successfully applied to obtain diffracting crystals of individual membrane proteins or improve crystal diffraction. New reagents and concepts are also used that target protein-detergent complexes. Besides the conventional crystallization methods, several novel techniques have been developed that aid in membrane protein crystallization.

1.2.3.1 Manipulation of Protein-Detergent Complex

It was proposed that small amphiphiles such as 1,2,3 heptanetriols have the ability to incorporate themselves into the membrane protein-detergent complex and decrease the size of the PDC, which is helpful in membrane protein crystallization (Timmins *et al.*, 1991; Gast *et al.*, 1994; Rosenow *et al.*, 2003). The use of heptanetriol facilitated the crystallization of the first membrane protein, the *Rhodopseudomonas viridis* photosynthetic reaction center (Michel, 1982), as well as cytochrome *c* oxidase from *Paracoccus denitrificans* (Iwata *et al.*, 1995) and it is commonly used as an additive for membrane protein crystallization experiments.

It is proposed that interactions between detergent micelles are responsible for the cloud point behavior observed in a detergent system when temperature or other conditions change (Loll *et al.*, 2001). Methods and crystallization screenings have been developed to take advantage of this attractive force that promotes interactions between detergent molecules in PDCs to facilitate crystallization (Wiener and Snook, 2001).

1.2.3.2 Antibody Assisted Membrane Protein Crystallization

One of the main reasons membrane proteins are hard to crystallize is their lack of polar residues on the protein surface of the transmembrane portion, which are essential in forming inter-molecular crystal contacts. The concept of antibody-mediated crystallization is to expand the hydrophilic surface area of a membrane protein to form more crystal contacts. It may also help to stabilize a particular conformation of the protein. In the crystal structure of the four subunit cytochrome *c* oxidase from *Paracoccus denitrificans*, all crystal contacts were found between attached antibody molecules (Ostermeier *et al.*, 1995). Such a technique was also successful in crystallization of the two subunit form of *Pd*CcO (Ostermeier *et al.*, 1997), yeast cytochrome bc_1 complex (Hunte *et al.*, 2000), and KcsA K^+ channel (Zhou *et al.*, 2001). A variation of the antibody mediated crystallization is the fusion protein approach described in the crystallization of *E. coli* cytochrome bo_3 ubiquinol oxidase, in which case a small peptide (peptide Z) was engineered into the membrane protein with the hope of forming crystal contacts (Byrne *et al.*, 2000). The fusion protein approach has not produced well-diffracting crystals yet, presumably because of the flexible nature of the linker region.

1.2.3.3 Crystallization of Membrane Protein in Lipid Cubic Phase

Crystallization of membrane protein in lipid cubic phase was first successfully applied to bacteriorhodopsin (Landau and Rosenbusch, 1996). In this method, a bicontinuous membrane formed by mixing lipids and water is used as a support matrix for nucleation and crystal growth. The exact mechanism of how membrane

protein crystals grow from the lipid cubic phase is unclear. Since membrane proteins tend to be less stable when they are extracted from native membranes and incorporated into detergent micelles, crystallizing membrane proteins in a quasisolid membrane environment throughout the crystallization process seems to have an advantage. This method has been particularly successful with a class of membrane proteins with seven robust transmembrane helices including bacteriorhodopsin (Landau and Rosenbusch, 1996; Luecke *et al.*, 1999), halorhodopsin (Kolbe *et al.*, 2000), and sensory rhodopsin II (Gordeliy *et al.*, 2002). Its applicability to general membrane protein crystallization is being explored.

1.2.4 Membrane Lipids and Membrane Protein Crystallization

1.2.4.1 Overview of Membrane Lipids

The membrane bilayer is formed by various types of membrane lipids. The composition of membrane lipids can vary between eukaryotes and prokaryotes and between cell organelle membranes and plasma membranes. Besides, the growth conditions of bacteria have a profound impact on the lipid composition of bacterial cell membranes (Benning *et al.*, 1995).

Phosphoglycerides are the most common membrane lipids. They all have a glycerol backbone and fatty acids are esterified to the hydroxyls at the sn1 and sn2 positions. At the sn3 position, the hydroxyl is linked to a phosphate group, which is in turn linked to different polar headgroups to form different phosphoglycerides including phosphatidyl ethanolamine (PE), phosphatidyl choline (PC), phosphatidyl inositol (PI), phosphatidyl serine (PS), phosphatidyl glycerol (PG) and

bis-phosphatidyl glycerol (cardiolipin; CDL). The structures of these phospholipids are shown in Figure 1.9. Although PC is rarely found in bacteria, it is quite common in *R. s.*, while PI is not found in many bacteria including *R. s.* (Haselkorn *et al.*, 2001). Besides phosphoglycerides, in animal cell membranes there are also phosphosphingolipids and glycosphingolipids. Another important lipid group found in chloroplast and bacterial membranes is glycoglycerolipids, including monogalactosyl diglyceride (MGD), digalactosyl diglyceride (DGD) and sulfoquinovosyl diacylglycerol (SQDG) (Figure 1.10). Sterols are also found in membranes, with cholesterol being the most commonly found type in membranes of cells and organelles such as lysosomes, endosomes and the Golgi complex.

In *R. s.* membranes, except for phospholipids and glycolipids, ornithine-containing lipids as well as betaine lipids can also be found in substantial amounts especially under phosphate-limited conditions (Benning *et al.*, 1995) (Figure 1.10). Monounsaturated and saturated fatty acids are the dominant fatty acid species found in *R. s.* lipids with oleic acid (18:1) being the most common (Imhoff, 1991).

1.2.4.2 Membrane Lipids and Membrane Protein Crystallization

In the early days of membrane protein crystallography, extensive efforts were made to obtain a clean, lipid free membrane protein sample after purification. This concept is now being questioned as more and more evidence suggests that native membrane lipids may be an important component in membrane protein crystallization. Membrane lipids not only provide the matrix for membrane proteins to reside in and serve as a diffusion barrier, they also have a profound functional impact on the

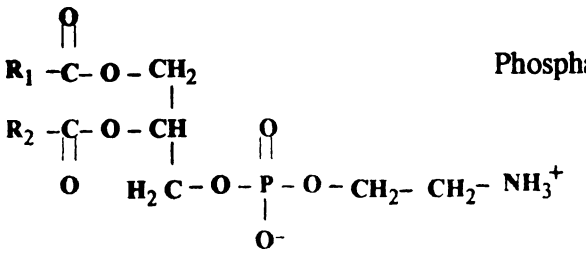

Phosphatidyl Ethanolamine (PE)

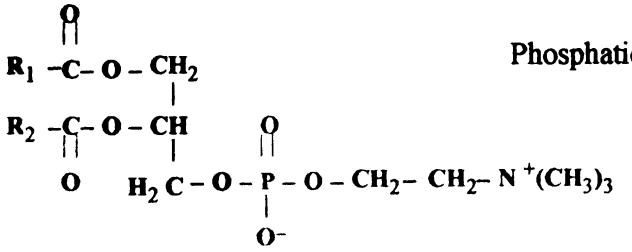

Phosphatidyl Choline (PC)

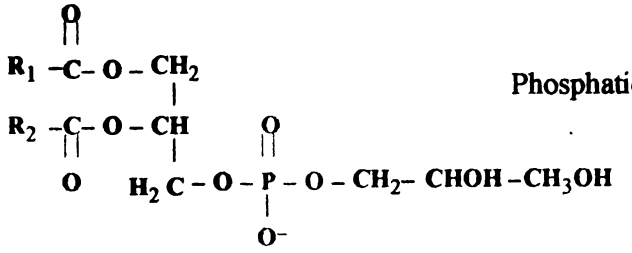

Phosphatidyl Glycerol (PG)

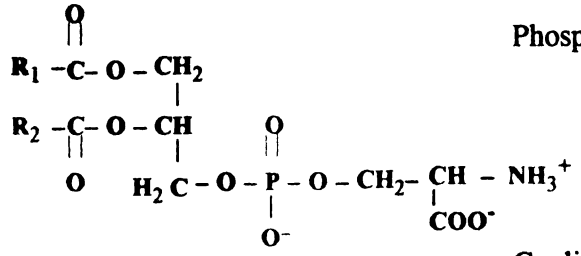

Phosphatidyl Serine (PS)

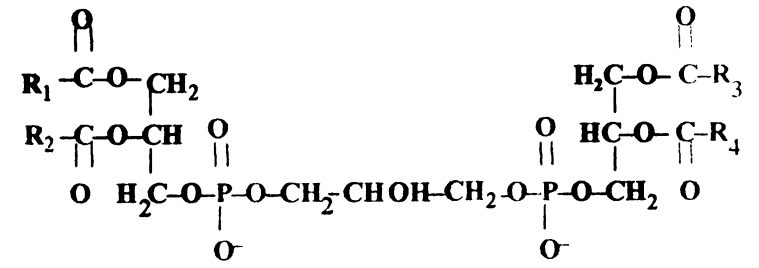

Cardiolipin (CDL)

Figure 1.9: Structures of phospholipids found in *Rhodobacter sphaeroides*.

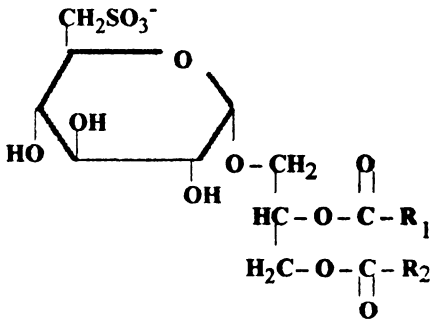

Sulfoquinovosyl Diacylglycerol (SQDG)

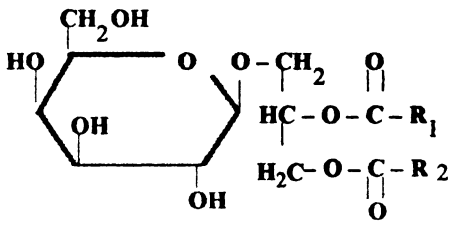

Monogalactosyl Diacylglycerol (MGD)

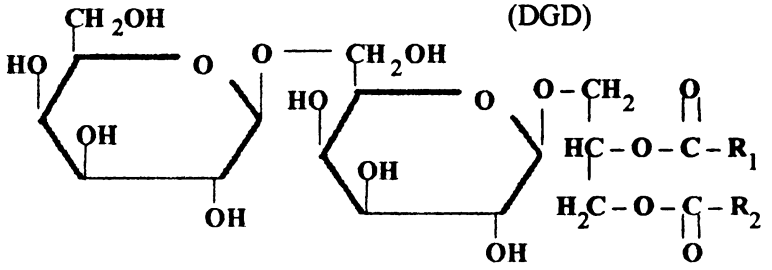

Digalactosyl Diacylglycerol (DGD)

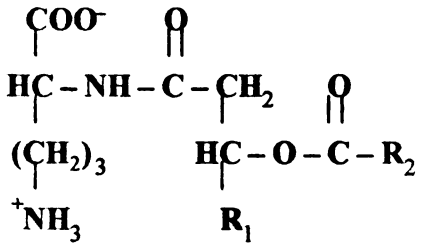

Ornithine Lipid

Figure 1.10: Structures of non-phospholipids found in *Rhodobacter sphaeroides*.

membrane protein, by maintaining lateral pressure to support the conformation of a membrane protein and by building to specific sites. Sometimes delipidation can cause loss of activity and dissociation of membrane protein subunits as shown in cytochrome *c* oxidase (Robinson, 1982; Sedlak and Robinson, 1999) and the cytochrome bc_1 complex (Yu and Yu, 1980; Schagger *et al.*, 1990). Lipid molecules are important in maintaining a more stable and homogeneous conformation of the membrane protein, which is of critical importance in crystallization. In fact, lipid molecules are resolved in many high resolution membrane protein crystal structures including cytochrome *c* oxidase from a few different sources (Yoshikawa *et al.*, 1998; Harrenga and Michel, 1999; Svensson-Ek *et al.*, 2002). Moreover, as the X-ray diffraction limit of the bovine C*c*O crystal increases, more and more lipids are found in the crystal structure, which may suggest a causal role for bound lipids in obtaining well diffracting crystals (Tsukihara *et al.*, 1996; Yoshikawa *et al.*, 1998; Tsukihara *et al.*, 2003). Therefore, during detergent solublization and protein purification steps, retention of the specifically bound lipid molecules on membrane proteins may be critical. Moreover, in crystallization experiments for the Ca^{2+} pump and the cytochrome b_6f complex, lipids were added into the crystallization mixture in order to get better diffracting crystals (Toyoshima *et al.*, 2000; Zhang *et al.*, 2003).

1.2.4.3 Lipid Analysis of C*c*O Using Thin Layer Chromatography and Mass Spectrometry

As the importance of lipids in membrane protein crystallization is getting more and more attention, efforts are being made to analyze the lipid components in

the C*c*O preparation. Results from such studies provide critical information about the bound lipids on C*c*O under different bacterial growth conditions and at different purification stages using various purification techniques. Thin layer chromatography is a common method of separating lipid species based upon their different hydrophobicities. Lipid extracts from different C*c*O samples were subjected to thin layer chromatography and semi-quantitative results on the amount of bound lipid on the protein samples could be obtained (Hilmi, 2002).

Matrix-assisted laser desorption-ionization time of flight mass spectrometry (MALDI-TOF) is a sensitive and relatively quick method of obtaining lipid component information in a membrane protein sample. It only requires picomole amounts of sample without the need for lipid extraction, thereby reducing the chance of lipid loss due to oxidation during lipid extraction processes. Combined with the optimal choice of matrix, it is sometimes capable of showing molecular ions that represent the lipid-bound protein subunits (Distler *et al.*, 2004). Although MALDI mass spectrometry is generally considered to be not quantitative, efforts are being made to find the appropriate controls for quantification. Lipid detection using MALDI-TOF mass spectrometry could be used as a routine assay during the membrane protein purification at each step and provide valuable information to improve the purification procedure in an effort to retain important bound lipid species.

Another ionization technique used in mass spectrometry could also be useful for detecting lipid content in membrane protein samples. Electrospray ionization (ESI) has the advantage of being both sensitive and quantitative. However, this method

requires that the lipids be extracted from the membrane protein sample, which could lead to the oxidation and degradation of lipids.

Chapter 2. METHODS

2.1 Molecular Engineering of Various Strains of *Rhodobacter sphaeroides* that Produce C*c*O with Various Subunit Contents

The molecular engineering of various strains of *Rhodobacter sphaeroides* was performed by Dr. Carrie Hiser in our lab. Figure 2.1 shows the amino acid sequences of the four subunits of *R. s.* cytochrome *c* oxidase. The positions of the engineered histidine tag at either the C terminus of subunit I or the shortened C-terminus of subunit II are shown in blue and red, respectively. For some of the constructs expressing subunit I histidine-tagged C*c*O, the truncated form of the subunit II was incorporated into the overexpression plasmid. The truncation site is indicated by a space between $Y287_{II}$ and $E288_{II}$. Two different forms of subunit IV were cloned and inserted into the overexpression plasmid under the control of the subunit I promoter: the long form (complete subunit IV sequence) and the short form (complete sequence of subunit IV less the underlined N terminal 10 amino acid residues).

In order to obtain crystals of C*c*O that diffract X-rays to high resolution, different strains of *R. s.* that express forms of C*c*O with different subunit contents were made. All four subunits are inserted into the overexpression plasmid (Zhen *et al.*, 1998) in different combinations, with the histidine tag attached to either the C terminus of subunit I or the shortened C terminus of subunit II. The overexpression plasmid was then transformed into *R. s.* cells via biparental conjugation (Shapleigh and Gennis, 1992; Hiser *et al.*, 2001). Table 2.1 summarizes the different strains of *R. s.* and the subunit contents of C*c*O produced.

Subunit I :

MADAAIHGHEHDRRGFFTRWFMSTNHKDIGVLYLFTGGLVGLISVAFTVYMRMELMAPGVQFMCAEHLESGLVKGFFQSL
WPSAVENCTPNGHLWNVMITGHGILMMFFVVIPALFGGFGNYFMPLHIGAPDMAFPRMNNLSYWLYVAGTSLAVASLFAP
GGNGQLGSGIGWVLYPPLSTSESGYSTDLAIFAVHLSGASSILGAINMITTFLNMRAPGMTMHKVPLFAWSIFVTAWLIL
LALPVLAGAITMLLTDRNFGTTFFQPSGGGDPVLYQHILWFFGHPEVYIIVLPAFGIVSHVIATFAKKPIFGYLPMVYAM
VAIGVLGFVVWAHHMYTAGLSLTQQSYFMMATMVIAVPTGIKIFSWIATMWGGSIELKTPMLWALGFLFLFTVGGVTGIV
LSQASVDRYYHDTYYVVAHFHYVMSLGAVFGIFAGIYFWIGKMSGRQYPEWAGKLHFWMMFVGANLTFFPQHFLGRQGMP
RRYIDYPEAFATWNFVSSLGAFLSFASFLFFLGVIFYTLTRGARVTANNYWNEHADTLEWTLTSPPPEHTFEQLPKREDW
ERAPAH + (SNHHHHHH)

Subunit II:

MRHSTTLTGCATGAAGLLAATAAAAQQQSLEIIGRPQPGGTGFQPSASPVATQIHWLDGFILVIIAAITIFVTLLILYAV
WRFHEKRNKVPARFTHNSPLEIAWTIVPIVILVAIGAFSLPVLFNQQEIPEADVTVKVTGYQWYWGYEYPDEEISFESYM
IGSPATGGDNRMSPEVEQQLIEAGYSRDEFLLATDTAMVVPVNKTVVVQVTGADVIHSWTVPAFGVKQDAVPGRLAQLWF
RAEREGIFFGQCSELCGISHAYMPITVKVVSEEAYAAWLEQ**ARGGTY** ELSSVLPATPAGVSVE
(HHHHHH)

Subunit III:

MAHAKNHDYHILPPSIWPFMASVGAFVMLFGAVLWMHGSGPWMGLIGLVVVLYTMFGWWSDVVTESLEGDHTPVVRLGLR
WGFILFIMSEVMFFSAWFWSFFKHALYPMGPESPIIDGIFPPEGIITFDPWHLPLINTLILLCSGCAATWAHHALVHENN
RRDVAWGLALAIALGALFTVFQAYEYSHAAFGFAGNIYGANFFMATGFHGFHVIVGTIFLLVCLIRVQRGHFTPEKHVGF
EAAIWYWHFVDVVWLFLFASIYIWGQ

Subunit IV:

MAETNKGTGPMADHSHPAHGHVAGSMDITQQEKTFAGFVRMVTWAAVVIVAALIFLALANA

Figure 2.1: Amino acid sequences of *Rs*C*c*O. The position of the histidine tag attached to the C-terminus of subunit I and subunit II is shown in blue and red, respectively.

Strain Name	Parental Strain & Subunit Deletions	Plasmid Name	His-tag Position	Subunit Compositions			
				Sub I	Sub II	Sub III	Sub IV
25-1	YZ200 [2], ΔII ΔIII	pCH25	Sub I	natural #	truncated §	natural	—
120	JS100 [1], ΔI	pCH120	Sub I	natural #	natural	natural	long ¥
157	JS100 [1], ΔI	pCH157	Sub I	natural #	natural	natural	short £
119	JS100 [1], ΔI	pCH119	Sub I	natural #	truncated §	natural	long ¥
156	YZ200 [2], ΔII ΔIII	pCH156	Sub I	natural #	truncated §	natural	long ¥
163	YZ200 [2], ΔII ΔIII	pCH163	Sub I	natural #	truncated §	natural	short £
167	YZ200 [2], ΔII ΔIII	pCH167	Sub II	natural	truncated *	natural	long ¥
169	YZ200 [2], ΔII ΔIII	pCH169	Sub II	natural	truncated *	natural	short £
169Δ4	Δ1Δ4 [3], ΔI ΔIV	pCH169	Sub II	natural	truncated *	natural	short £
37Δ4	Δ1Δ4 [3], ΔI ΔIV	pCH37	Sub II	natural	truncated *	natural	—

References: (1) Shapleigh and Gennis, 1992 (2) Zhen, et al. 1998 (3) Hiser, et al. unpublished

#: natural subunit I with histidine tag attached to the C terminus

§: subunit II artificially truncated at -16 aa from the C terminus of native subunit II

*: histidine tag attached to the near C terminus (-22 aa) of native subunit II

¥: complete subunit IV gene starting with the first potential starting codon

£: subunit IV gene starting with the second potential starting codon at 10 aa downstream

Table 2.1: Different *R. s.* strains and their subunit compositions used in this study.

2.2 UV-Visible Spectroscopy

UV-Visible spectra were taken using a Perkin-Elmer Lambda 40P UV-visible spectrophotometer. For a reduced minus oxidized C*c*O difference spectrum, sodium dithionite and ferricyanide were used to fully reduce or oxidize the enzyme samples, respectively. The enzyme was first diluted in a buffer containing 100 mM HEPES, pH 7.9, 1 mM EDTA, and 0.1% dodecyl maltoside prior to the spectra being taken. The extinction coefficient used was $\Delta\varepsilon_{606\text{-}630} = 24\ cm^{-1}mM^{-1}$ (Zhen *et al.*, 1998). For absolute spectra of the dithionite-reduced C*c*O, the extinction coefficient used was $\Delta\varepsilon_{606\text{-}640} = 40\ cm^{-1}mM^{-1}$ (Zhen *et al.*, 1998).

2.3 SDS-PAGE

Sodium dodecyl sulfate polyacrylamide gel electrophoresis (SDS-PAGE) was used to detect the C*c*O subunit composition including different forms of subunits and the impurities contained in C*c*O sample. Approximately 10 μg of protein in sample buffer containing 25 mM Tris, pH 6.5, 40% glycerol, 8% SDS and 0.08% bromophenol blue was loaded onto an 8% acrylamide stacking gel at pH 6.8 on top of an 18% acrylamide separating gel at pH 8.8. The gel was electrophoresed at 100 V at room temperature (Peiffer *et al.*, 1990). The gel was then stained with Coomassie blue and destained with 7.5% glacial acetic acid for 3 times (Hiser *et al.*, 2001). Polypeptide sizes were estimated from low-molecular weight range markers from Bio-Rad.

2.4 Cytochrome *c* Oxidase Activity Assay

The oxidase activity of *Rs*C*c*O was measured polarographically by using a

Gilson model 5/6H oxygraph at 25°C in a 1.75ml reaction cell containing 50 mM KH_2PO_4, pH 6.5, 0.05% dodecyl maltoside, 2.8 mM ascorbate, 0.55 mM TMPD and 30 μM of horse heart cytochrome *c*. The oxidase concentrations were in the range of 5 nM to 50 nM.

2.5 Protein Concentration Assay

To measure the total protein concentration in the membrane sample, the BCA (bicinchoninic acid) Protein Assay Reagent Kit from Pierce was used (Smith *et al.*, 1985). Such an assay kit has detergent-compatible formulations. Membrane samples and bovine serum albumin (BSA) standards were diluted in a buffer containing 10 mM Tris, pH 11.2, 40 mM KCl, and 0.25% deoxycholate. Two ml mixture of reagent A containing 1% BCA-Na_2, 2% $Na_2CO_3.H_2O$, 0.16% Na_2 tartrate, 0.4% NaOH, 0.95% $NaHCO_3$, pH 11.25 and reagent B containing 4% $CuSO_4 \cdot 5\ H_2O$ mixed in a 50:1 ratio was added to each of the diluted sample tubes and BSA standard tubes. All the tubes were incubated at 60°C for 30 min and the absorbance at 562 nm was measured. Protein concentration was calculated for the membrane samples against the standard curve generated with the absorbance measurements at 562 nm for the BSA standards with known protein concentration.

2.6 Phosphorous Assay

Phosphate contents in C*c*O samples at different purification stages were measured using an adapted standard method (Bartlett, 1959). In a typical assay, 10 μl of 480 μM C*c*O were mixed with H_2O to a final volume of 2 ml in a glass tube tightly sealed with glass stopper. Water alone was used as the blank control. Samples and

blanks were heated in an oven at 150-160°C for at least 3 hours. Fifty μl of phosphorous-free hydrogen peroxide was added to each sample and the tubes were tightly sealed again and incubated for at least another 1.5 hours to decompose all the peroxide. After that, 4.4 ml of H_2O was added to each of the tubes followed by 0.2 ml of Fiske-SubbaRow reagent (15 g anhydrous sodium bisulfite, 0.25 g 1-amino-2-naphthol-4-sulfonic acid, 0.5 g anhydrous sodium sulfite in 100 ml water, filtered and kept in dark) and 0.2 ml of 5% ammonium molybdate. The solutions were mixed thoroughly and heated for 10 minutes in a boiling water bath. The tubes were cooled and the absorbance at 830 nm was measured for each tube. The absorbance readings at 830 nm were then compared to the phosphate standards containing 0, 0.02, 0.04, 0.06, 0.08, 0.10 μmole of KH_2PO_4 treated with the same procedure to calculate the phosphorous content in the C*c*O samples.

2.7 Mass Spectrometry Analysis of Membrane Lipids

All the mass spectrometry analyses of membrane lipids in protein samples and re-dissolved *Rs*C*c*O crystals using the matrix-assisted laser desorption ionization (MALDI) method were performed by Xi Zhang at the Proteomics Facility in the Department of Biochemistry of Michigan State University using PerSeptive Biosystems Voyager STR in linear positive and negative ion modes. Post-source decay (PSD) negative ion mode was also used to identify lipid species. Different matrices including 2, 5-dihydroxybenzoic acid (DHB) and α -cyano-4-hydroxycinnamic acid (CHCA), saturated in 50% water/50% acetyl nitrile,

were used. Samples spots were prepared by mixing equal volumes of matrix and C*c*O sample. Lipid standards were purchased from Avanti Polar Lipids.

2.8 Growth and Harvest of *R. s.* Cells

R. s. cells were grown on Sistrom's plates with 50 μg/ml spectinomycin, 50 μg/ml streptomycin and 1 μg/ml tetracycline pH 7.0 at 30°C for 3-5 days. Cells were picked up from the plates and inoculated in small flasks with 100ml of Sistrom's media with the same antibiotics and grown for two days at 30°C with vigorous shaking at 250 rpm. Fifty ml of starter culture were used to inoculate a 2.8 L Fernbach flask with 800 ml Sistrom's media containing 1 μg/ml tetracycline and 25 μg/ml spectinomycin, and 25 μg/ml streptomycin. The Fernbach flasks were shaken at 250 rpm at 30°C for 2-3 days until the absorbance reading at 660 nm was above 1.7 and a pH over 8.5. *R. s.* cells were harvested by centrifugation in a GS-3 rotor at 14,000 x g for 20 minutes at 4°C. The cell pellets were resuspended in buffer containing 50 mM KH_2PO_4 and 1 mM EDTA, pH 6.5 and stored at -80°C (Zhen *et al.*, 1998).

Sometimes the *R. s.* cells in a liquid culture undergo genetic recombination in its overexpression plasmid. As a result, the gene(s) encoding all or part of C*c*O can be cleaved off from the overexpression plasmid, leaving essentially no C*c*O expression. In order to circumvent this problem, prior to inoculating liquid cultures, *R. s.* cells were streaked on a Sistrom's plate to single colonies. Small single colonies which contained the intact overexpression plasmid were picked up and inoculated onto another Sistrom's plate. The plate with *R. s.* cells from a single small colony was then used to start up small liquid culture. On the other hand, big colonies, which had

presumably cleaved overexpression plasmid and therefore grew faster on the Sistrom's plate, were discarded. Alternatively, *R. s.* cells from an entire plate that was grown from a single small colony were picked up and inoculated into a big flask directly in order to minimize the chance of the occurrence of the cleavage of the overexpression plasmid.

2.9 Preparation of *R. s.* Cytoplasmic Membranes

Resuspended *R. s.* cells were thawed and small amounts of DNase I and RNase were added. The cell resuspension was then homogenized and cells were broken with two passages through the French press at 20,000 psi. Whole cells and debris were removed by centrifugation at 30,000 x g for 30 minutes at 4°C. The supernatant was collected and cell membranes were pelleted by using ultracentrifugation at 200,000 x g for 1.5 hours. Depending on whether the histidine tag was attached to the C-terminus of subunit I or to the shortened C-terminus of subunit II, the pellet was resuspended in buffer containing 10 mM Tris, pH 8.0 with either 40 mM KCl or 220 mM KCl, respectively. The membrane resuspensions were quick-frozen in liquid nitrogen and stored at –80°C.

2.10 Detergent Solublization of *R. s.* Cytoplasmic Membrane

Before detergent solublization of the cell membranes, the protein concentration in the membranes was analyzed by using the BCA Protein Assay Reagent Kit as described earlier in this chapter. The *R. s.* cell membrane sample was diluted to a protein concentration of 10 mg/ml with buffer containing 10 mM Tris (pH 8.0), 40 mM or 220 mM KCl depending on the position of the histidine tag as

described above, and 1 mM imidazole. Dodecyl maltoside was then added to the membrane resuspension sample at a final concentration of 1% (w/v). The solution was stirred for 20 minutes at 4°C and unsolublized material was removed by ultracentrifugation at 200,000 x g for 30 minutes. The supernatant containing *Rs*C*c*Owas collected and used immediately for further column purification.

2.11 Column Chromatography for Purification of Enzyme Used for Crystallization of the Four Subunit *Rs*C*c*O

In order to obtain crystals of the four subunit enzyme complex, a two-step column purification protocol was used. The following protocols were adapted from what was described previously (Svensson-Ek *et al.*, 2002). To purify *Rs*C*c*O that had a histidine tag attached to the C-terminus of subunit I, the first step was Ni-NTA affinity column purification and the second step was either Mono Q ion-exchange column purification, or DEAE Sepharose ion-exchange column purification. To purify *Rs*C*c*O with a histidine tag attached to the shortened C-terminus of subunit II, the first step was Ni-NTA affinity column purification and the second step was either DEAE Sepharose ion-exchange column purification, or Superdex 200 size-exclusion column purification.

2.11.1 Purification of C*c*O with the Histidine-Tag Attached to the C-Terminus of Subunit I for Crystallization

2.11.11.1 Ni-NTA Column Chromatography

For enzyme with a histidine-tag attached to the C-terminus of subunit I, the detergent solublized membrane sample containing typically 30-60 mg *Rs*C*c*O was

loaded onto a home-packed Ni-NTA (Qiagen) column (typical volume: 18 ml) connected to an AKTA FPLC system (Pharmacia) that was pre-equilibrated with 80 ml buffer A containing 10 mM Tris (pH 8.0), 40 mM KCl, 10 mM imidazole and 0.05% dodecyl maltoside. The column was washed extensively with 12 column volumes of buffer A before a linear gradient of 0 – 100% buffer B containing 10 mM Tris (pH8.0), 40 mM KCl, 150 mM imidazole, 0.05% dodecyl maltoside was applied. The length of the gradient was typically 15 column volumes. The green fractions containing *Cc*O were pooled, and imidazole was removed by washing and concentrating 2 times by using a Centriplus YM100 filter unit (MW cutoff 100 kDa; maximum volume 15ml, Millipore). Sometimes, the green fractions from the Ni-NTA column were simply pooled and loaded onto the next ion-exchange column without any washing and concentrating, which will be described later in the Results section. The yield of this column purification step was typically around 50%.

2.11.1.2 Ion-exchange Column Chromatography Using Either Mono Q Column or DEAE Sepharose Column

Pooled and washed fractions of enzyme with a histidine tag attached to the C-terminus of subunit I were loaded onto a Mono Q column (Pharmacia) (column volume: 8 ml) pre-equilibrated with 50 ml buffer A containing 10 mM Tris, pH 8.0, 0.05% dodecyl maltoside. The column was washed with buffer A for two column volumes before a linear gradient of 0-100% buffer B containing 10mM Tris, pH 8.0, 0.5M KCl, 0.05% dodecyl maltoside was applied. The length of the gradient was 20 column volumes. Green fractions from the linear gradient were then pooled,

concentrated and the buffer was exchanged to 10 mM Tris, pH 8.0, 0.16% - 0.24% decyl maltoside by washing and concentrating 3-6 times by using a Centriplus YM100 filter unit. The yield of this column purification step and the washing and concentrating was typically around 50%.

When a DEAE Sepharose column was used instead of Mono Q column, pooled and washed fractions of enzyme were loaded onto the DEAE Sepharose column (Pharmacia) (column volume: 20 ml) pre-equilibrated with 100 ml buffer A containing 10 mM Tris, pH 8.0, 0.05% dodecyl maltoside. The column was washed with buffer A for three column volumes before a linear gradient of 0-100% buffer B containing 10 mM Tris, pH 8.0, 0.5 M KCl, 0.05% dodecyl maltoside was applied. The length of the gradient was typically 15 column volumes. Green fractions from the linear gradient were then pooled, concentrated and the buffer was exchanged to 10mM Tris, pH 8.0, 0.16% - 0.24% decyl maltoside by washing and concentrating 3-6 times by using a Centriplus YM100 filter unit. Typical yield for this column purification step with washing and concentrating is around 50%.

2.11.2 Purification of C*c*O with the Histidine-Tag Attached to the Shortened C-Terminus of Subunit II for Crystallization

2.11.2.1. Ni-NTA Column Chromatography

For enzyme with a histidine-tag attached to the shortened C-terminus of subunit II, the detergent solublized membrane sample containing typically 30 – 60 mg *Rs*C*c*O was loaded onto a home-packed Ni-NTA (Qiagen) column (typical column volume: 18 – 20 ml) connected to an AKTA FPLC system that was pre-equilibrated

with 80 ml buffer A containing 10 mM Tris (pH 8.0), 220 mM KCl, 2.5 mM imidazole and 0.05% dodecyl maltoside. The column was washed extensively with 12 column volumes of buffer A before a linear gradient of 0 – 100% buffer B containing 10 mM Tris (pH8.0), 220 mM KCl, 150 mM imidazole, 0.05% dodecyl maltoside was applied. The length of the gradient was 15 column volumes. Often there were two very closely associated peaks in the elution profile. In order to completely separate the two peaks, sometimes a two-step linear gradient was applied. First the percentage of buffer B was increased to approximately 8-10% (approximate imidazole concentration: 15 mM) and held constant for approximately 6 column volumes to elute off the first peak containing cytochrome *c* oxidase bound to a major contaminating species. After this washing step, the concentration of buffer B was further increased to 100% (final imidazole concentration: 150 mM) with a linear gradient (the length of the gradient: 13 column volumes) and the second peak containing purer *Rs*CcO was eluted and the green fractions under the second peak were pooled. Typical yield after this column purification step is approximately 40% - 50%.

If the second purification step was a DEAE Sepharose column, the fractions from the Ni-NTA column were pooled and diluted 4-5 times with buffer containing 10 mM Tris, pH 8.0, 0.05% dodecyl maltoside and loaded onto the DEAE Sepharose column. If the second purification step was Superdex 200 size exclusion chromatography, the fractions were pooled and concentrated to approximately 1 ml in volume in a stirred ultrafiltration cell under N_2 pressure by using a YM100 ultrafiltration membrane (MW cutoff 100 kDa; maximum volume 50 ml, Millipore).

2.11.2.2 Ion-exchange Column Chromatography Using DEAE Sepharose Column

Pooled fractions of enzyme were diluted as described above and loaded onto DEAE Sepharose column (column size: 20 ml) pre-equilibrated with 100 ml buffer A containing 10 mM Tris, pH 8.0, 0.05% dodecyl maltoside. The column was washed with buffer A for three column volumes before a linear gradient of 0-100% buffer B containing 10 mM Tris, pH 8.0, 0.5 M KCl, 0.05% dodecyl maltoside was applied. The length of the gradient was 15 column volumes. Green fractions from the linear gradient were then pooled, concentrated and the buffer was exchanged to 10 mM Tris, pH 8.0, 0.16% - 0.24% decyl maltoside by washing and concentrating 2 - 3 times by using a Centriplus YM100 filter unit or in a stirred ultrafiltration cell as described above. The typical yield of this column purification step with washing and concentrating was around 50%.

2.11.2.3 Superdex 200 Size Exclusion Chromatography

Fractions of enzyme with a histidine tag attached to the shortened C-terminus of subunit II from the Ni-NTA column in 10 mM Tris, pH 8.0, 150 mM NaCl, 0.16% decyl maltoside were loaded onto a Superdex 200 column (Pharmacia) (column volume: 120 ml) pre-equilibrated with the same buffer. The same buffer was then used to wash the column. Green fractions containing C*c*O were pooled and concentrated by using a Centriplus YM100 filter unit. Typical yield after this column purification step was around 60%.

2.12 Crystallization of the Four Subunit *Rs*C*c*O

In a typical crystallization experiment to obtain crystals of the four subunit

*Rs*C*c*O, hanging drop or sitting drop crystallization set-ups were used. Figure 2.2(A) and Figure 2.2(B) show the hanging-drop crystallization set-up and sitting-drop crystallization set-up, respectively. Both crystallization set-ups help to achieve supersaturation of the protein solution through vapor diffusion. However, in a sitting-drop crystallization experiment, a much larger volume can be used in order to obtain larger crystals. All the crystallization experiments were set up in the cold room. In a typical hanging-drop crystallization experiment, 2 µl of enzyme solution containing 10 mM Tris, pH 8.0, 0.16-0.24% decyl maltoside and 120-160 µM C*c*O was mixed with 1 µl of reservoir solution containing 100 mM sodium citrate, pH 5.6-5.8, 100 mM NaCl, 18-22.5% PEG-400 and 1 µl of crystallization additive solution containing 5% heptanetriol, 33 mM $MgCl_2$, and 0.026% dodelcyl maltoside. The crystallization drop was incubated at 14°C overnight to increase the rate of vapor equilibrium, then the temperature of the incubator was lowered to 4°C at a rate of 1°C per hour and held at 4°C for up to 2 weeks. Triangular crystals of four subunit *Rs*C*c*O usually appeared after 5-7 days and continued growing to up to $0.2 \times 0.2 \times 0.1$ mm in approximately two weeks.

If the sitting drop crystallization set-up was used instead of the hanging-drop method, the typical volume of the drop solution increased to 10 µl of enzyme solution containing 10 mM Tris, pH 8.0, 0.16-0.20% decyl maltoside and 80-120 µM C*c*O mixed with 5 µl of reservoir solution and 5 µL of crystallization additive solution as described above. The crystallization drop was incubated at 4°C and triangular crystals

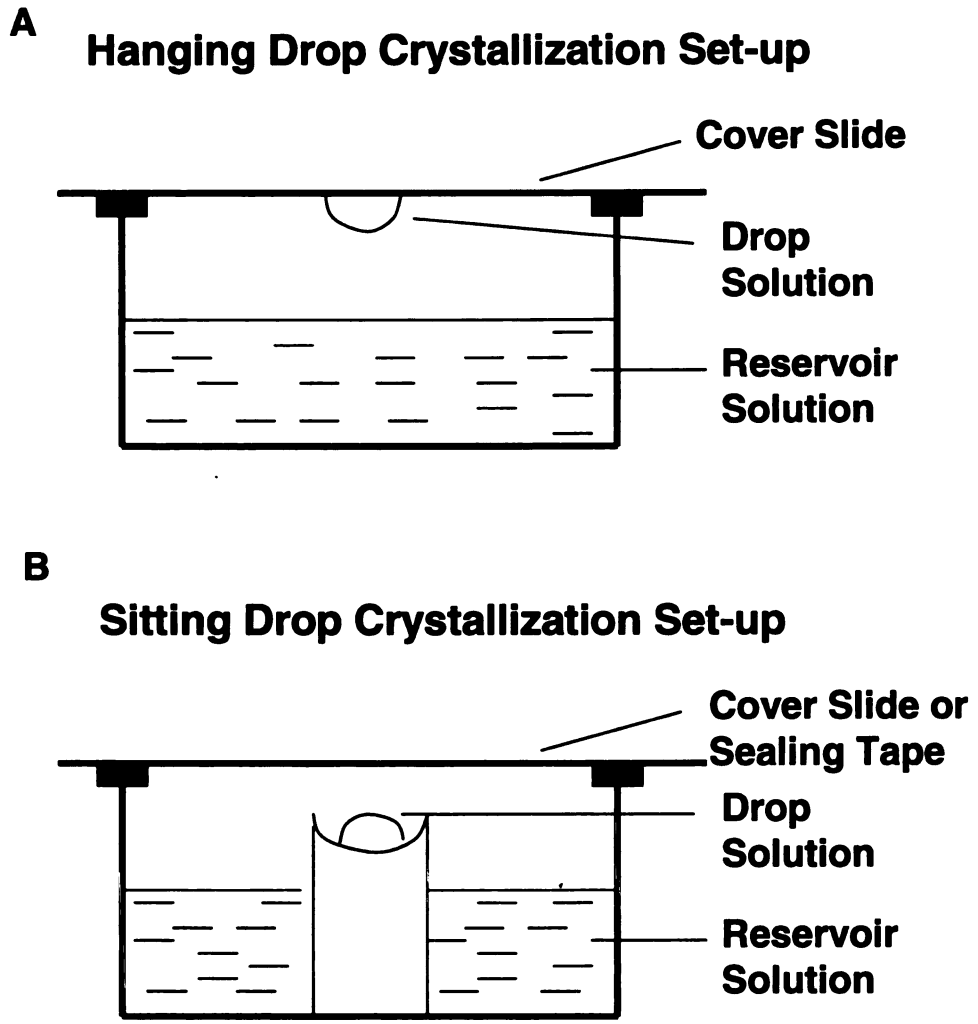

Figure 2.2: Hanging drop (A) and sitting drop (B) vapor diffusion crystallization set-ups.

of the four subunit *Rs*C*c*O started to appear after approximately 10 days and continued growing to their full size of up to 0.3 × 0.3 × 0.15 mm in approximately 4 weeks.

2.13 Flashcooling of the Four Subunit *Rs*C*c*O Crystals

Because the crystals were grown at 4°C, and would quickly dissolve under room temperature, the flashcooling procedures were performed in the cold room. In order to lessen the humidity in the cold room, which could lead to ice formation during the crystal flashcooling, Drierite or liquid nitrogen was used as a desiccant.

Crystals of the four subunit *Rs*C*c*O were picked up from the original crystallization drop with a cryoloop and soaked in approximately 30 μL of stabilizing solution in a sitting drop well. The stabilizing solution was made to mimic the assumed concentration of ingredients in the crystallization drop after equilibrium except for a little less detergent in a sitting drop well. In more detail, the stabilizing solution contained 91 mM sodium citrate, pH 5.6-5.8, 91 mM NaCl, 18 mM Tris, pH 8.0, 30 mM $MgCl_2$, 2.5% heptanetriol, 0.16% decyl maltoside, 0.016% dodecyl maltoside, and 18-20% PEG-400. A small aliquot of the cryosolution which contained the same ingredients as those in the stabilizing solution except for a higher (30-32%) PEG-400 concentration was then added to the stabilizing solution containing the crystals and the two solutions were carefully mixed. A small aliquot was then taken out from the sitting drop well to return the drop volume to 30 μl. The same procedure was repeated several times until approximately the entire solution in the sitting drop well had been exchanged to the cryosolution. The entire procedure took

approximately 8-10 minutes. Adding small aliquots of the cryosolution ensured the gradual increase in PEG-400 concentration and thus protected the crystals from being damaged due to dramatic increase in the osmotic pressure in the surrounding environments. The crystals were then picked up again using a cryoloop and submerged into liquid propane prechilled with liquid nitrogen or directly into liquid nitrogen itself. The flashcooled crystals were then stored in liquid nitrogen in cryovials until data collection.

2.14 Soaking of Four Subunit *Rs*C*c*O Crystals in Cadmium Solutions Prior to Flashcooling

Crystals of the four subunit *Rs*C*c*O were soaked in a solution containing cadmium in order to determine the cadmium binding site(s) responsible for the observed inhibitory effect on the enzyme. In a typical soaking experiment, crystals of the four subunit *Rs*C*c*O were picked up with a cryoloop and transferred to approximately 30 μL of stabilizing solution (see the previous paragraph for the detailed concentrations of ingredients) containing varying concentration of $CdCl_2$ from 1.5 mM to 9 mM. The crystals were soaked in the stabilizing solution containing $CdCl_2$ for half an hour to a few days to allow binding of Cd^{2+} to the enzyme. After soaking, the crystals underwent the same flashcooling procedure as described in the previous paragraph except that the cryosolution was supplemented with the same concentration of $CdCl_2$ as in the stabilizing solutions. The crystals were flashcooled in liquid nitrogen directly and stored until data collection.

2.15 Column Chromatography for Purification of Enzyme Used for Crystallization of the I-II Subunit *Rs*C*c*O

To purify *Rs*C*c*O in order to obtain crystals of the I-II subunit *Rs*C*c*O, a single step of Ni-NTA affinity column purification was used. Different C*c*O forms all had histidine tags attached to the shortened C-terminus of subunit II and the purification protocol was similar to the modified Ni-NTA purification protocol for subunit II histidine-tagged *Rs*C*c*O. (section 2.11.2.1)

The detergent solublized membrane sample was loaded onto a home-packed Ni-NTA column (column volume: 18-20 ml) connected to an AKTA FPLC system that was pre-equilibrated with 80 ml buffer A containing 10 mM Tris (pH 8.0), 220 mM KCl, 2.5 mM imidazole and 0.05% dodecyl maltoside. The column was washed extensively with 12 column volumes of buffer A. A two step gradient of increasing concentration of buffer B containing 10 mM Tris, pH 8.0, 220 mM KCl, 150 mM imidazole, 0.05% dodecyl maltoside was applied. First the percentage of buffer B was increased to approximately 8-10% (approximate imidazole concentration: 15 mM) and held constant for approximately 6 column volumes to elute off the first peak containing cytochrome *c* oxidase bound to a major contaminating species. After this washing step, the concentration of buffer B was further increased to 100% (final imidazole concentration: 150 mM) with a linear gradient and the second peak containing purer C*c*O was eluted and the green fractions under the second peak were pooled.

The pooled fractions containing reasonably pure *Rs*C*c*O were washed and

concentrated in a stirred ultrafiltration cell as described above. The buffer was exchanged to 10 mM Tris, pH 8.0, 150 mM NaCl, with 0.16% decyl maltoside by washing and concentrating 2 – 3 times. The typical yield of purified protein is approximately 30-50%.

2.16 Crystallization of the I-II Subunit *Rs*C*c*O

In a typical crystallization experiment to obtain crystals of the I-II subunit *Rs*C*c*O, sitting drop crystallization set-up was used as shown in Figure 2.2(B). All the crystallization experiments were set up in the cold room at 4°C. In a typical crystallization experiment, 6 µl of enzyme solution containing 10 mM Tris, pH 8.0, 50 mM NaCl, 0.20% decyl maltoside and 120 µM C*c*O was mixed with 3 µL of reservoir solution containing 100 mM MES, pH 6.3-6.9, 24-26% PEG-400 and 3 µl of crystallization additive solution containing 5% heptanetriol, 32 mM $MgCl_2$, 1.3 mM $CdCl_2$ and 0.026% dodecyl maltoside. Heavy protein precipitation occurred immediately after mixing of the drop contents.

The crystallization drop was incubated at 4°C and crystal showers of tiny triangular crystals of the four subunit *Rs*C*c*O started to appear after approximately 3-4 days. Bigger, football-shaped crystals of I-II subunit *Rs*C*c*O crystals started to appear after approximately 2 weeks and continued to grow to their full size of up to 0.2 × 0.2 × 0.1 mm in 3-4weeks.

2.17 Flashcooling of the I-II Subunit *Rs*C*c*O Crystals

The flashcooling method of the I-II subunit crystals was the same as the method used for flashcooling four subunit crystals (section 2.13) except that 1.3 mM

$CdCl_2$ was supplemented in both the stabilizing solution and the cryosolution.

2.18 Data Collection and Processing

X-ray diffraction data were collected at DND-CAT, Station 5ID-B, and at COM-CAT, Station 32ID-B, Advanced Photon Sources, Argonne National Laboratory. The detector used was MARCCD-M165. The data set was collected by the rotation method. During the data collection from the four subunit C*c*O crystals, the crystal was rotated about the ϕ angle for a total of 120° with 0.4° rotation per frame. During the data collection from the I-II subunit C*c*O crystals, an 180° rotation about ϕ angle was performed with 0.3° per frame. Sometimes two data sets were collected on a single crystal, one for the high resolution range with a crystal-to-detector distance of about 180 mm and a longer X-ray exposure time, and another data set for the low resolution range with a crystal-to-detector distance of approximately 260 mm and a shorter X-ray exposure time. The data were processed with Denzo and scaled and merged using Scalepack (Otwinowski and Minor, 1997).

2.19 Molecular Replacement and Structural Refinement

For the crystal structure determination of the four subunit *Rs*C*c*O, a rigid body refinement using the coordinates of the published structure of the four subunit *Rs*C*c*O (PDB entry 1M56) as the initial phasing model was performed with CNS 1.1 (Brunger *et al.*, 1998), followed by simulated annealing, and cycles of energy minimization, model visualization and manual model building. A group B factor refinement was performed at later stages of the refinement. Molecular visualization and model building were performed by using the program CHAIN (Sack and Quiocho, 1997).

For the crystal structure determination of the I-II subunit *Rs*C*c*O, an initial molecular replacement search was performed by using the program Phaser (Storoni *et al.*, 2004), using the coordinates of the four subunit cytochrome *c* oxidase (PDB entry 1M56) as the original search model. The molecular replacement search was successful and yielded two protein molecules per asymmetric unit. However, analysis of the crystal packing after initial rigid body refinement indicates there were severe clashes between C*c*O molecules in subunit III and subunit IV. Further analysis of the electron density maps revealed that there was no subunit III or subunit IV in the crystal structure. The coordinates of the polypeptide chains of subunit I and II were used as initial phasing model for structural refinement. Refinement of the structure was performed with CNS 1.1 using cycles of simulated annealing, and energy minimization (Brunger *et al.*, 1998). B factors were refined at the later stages. Molecular visualization and model building were performed by using the program CHAIN (Sack and Quiocho, 1997). The structure was first refined at 2.5 Å resolution and then the resolution was extended to include all data up to 2.35 Å. Towards the end of refinement, restrained refinement with TLS refinement were performed using Refmac5 (Bailey, 1994; Murshudov *et al.*, 1997; Winn *et al.*, 2001).

Chapter 3. RESULTS

3.1 X-ray Crystallography of the Four Subunit *Rs*C*c*O

3.1.1 Importance of Subunit IV in Crystallization of the Four Subunit *Rs*C*c*O and Overexpression of Subunit IV

Before the crystal structure of cytochrome *c* oxidase from *Rhodobacter sphaeroides* was solved by Iwata and colleagues (Svensson-Ek *et al.*, 2002), only three subunits (subunits I, II, and III) had been observed in the protein complex (Hosler *et al.*, 1992), although C*c*O from a very closely related bacterium, *Paracoccus denitrificans*, has four subunits (Ostermeier *et al.*, 1995). The crystal structure of *Rs*C*c*O showed that there are indeed four subunits in the complex. As shown in Figure 1.4, the single transmembrane helix of subunit IV of *Rs*C*c*O is partially surrounded by transmembrane helices from subunit I and subunit III. However, there is little direct protein-protein contact between subunit IV and its neighboring subunits. Most of the interactions are mediated through the phospholipid molecules immediately surrounding the transmembrane helix of subunit IV as shown in the crystal structure (Svensson-Ek *et al.*, 2002). Due to its lack of direct protein-protein contacts with its neighboring subunits, subunit IV could easily dissociate from the protein complex if those lipid molecules were lost during detergent solublization and column purification steps. As a result, subunit IV may not have been detected earlier because it was either completely absent or present but at a low stoichiometry in the purified protein. In fact, in the usual gels run to assess the protein purity (14% acrylamide), the ~6,000 dalton subunit is not observed (Hosler *et al.*, 1992). In addition, it was difficult to stain

subunit IV with Coomassie Blue in SDS-PAGE and when it did stain, the band representing subunit IV was always diffuse possibly due to different levels of lipid molecules associated with the protein.

The loss of subunit IV in the *Rs*C*c*O purification proved to be detrimental to the formation of well-ordered four subunit *Rs*C*c*O crystals. Analysis of the *Rs*C*c*O surface crystal contacts indicates that the key crystal contact occurs between the bottom part of one molecule, the flat surface formed by subunits I, III and IV, and the top of another, including the globular domain of subunit II. Figure 3.1 shows the importance of subunit IV in forming the key crystal contacts mediated through the interaction of the cytoplasmic portion (N terminus) of subunit IV and nearby residues from subunit I, II and III from a second molecule. Therefore, it is intuitive to conclude that loss of subunit IV leads to the inability of crystal formation.

Previously our lab was engaged in active pursuit of crystallization of *Rs*C*c*O using a strain of *R. s.* which overexpressed only subunits I, II and III. The purification procedure we applied involved two column purification steps, a Ni affinity column followed by a DEAE-5PW ion exchange column. The latter column was thought to extract lipid from the enzyme sample. In retrospect, the main reason for the inability to obtain *Rs*C*c*O crystals may have been due to substoichiometric amounts of subunit IV in the protein complex at the beginning of purification due to lower expression of subunit IV compared with the other three over-expressed subunits, and/or loss of subunit IV due to delipidation during the protein purification steps, particularly during the DEAE-5PW column purification step.

Figure 3.1: Major crystal contact regions in the crystal of the four subunit *RsCcO*. Subunits I, II, III, and IV are colored yellow, green, cyan, and purple, respectively. The N-terminal region of subunit IV (purple) of one *Rs*C*c*O molecule takes part in the major crystal contact during crystal formation.

In order to obtain the *Rs*C*c*O protein product which has all four subunits in stoichiometric amounts, the subunit IV gene was cloned, sequenced and inserted into the overexpression plasmid under the control of the strong subunit I promoter. It was found that there are two potential starting codons in the gene sequence of subunit IV in the *R. s.* genome and therefore there are two forms of subunit IV with different N terminus (Figure 2.1). In an earlier attempt, the complete subunit IV gene, starting with the first starting codon, was cloned and inserted into two different overexpression plasmids, which were then conjugated into parental *R. s.* strains individually, to make two new *R. s.* strains, 120 and 119. Strain 120 overexpresses all four subunits with a histidine tag attached to the C-terminus of subunit I and the other three subunits at their full lengths, while strain 119 is identical except for a shortened form of subunit II instead of the native full length subunit II (see Table 2.1 in Chapter 2, Method section). Successful expression of the plasmid would theoretically ensure the presence of all four subunits in *Rs*C*c*O in stoichiometric amounts. In fact, *Rs*C*c*O obtained from strains 120 and 119 did produce four subunit crystals when modified protein preparation procedures were applied (see below).

3.1.2 Modifications of Detergent Solublization and Protein Purification Procedures for Crystallization of *Rs*C*c*O

Since lipids were found to be crucial in securing subunit IV in the enzyme complex, efforts were made to try to standardize and optimize the protein purification procedure in order to retain more lipids. The first step in protein preparation is detergent solublization of *R. s.* cell membranes. This step is crucial in that too little

detergent fails to extract all the protein into the aqueous solution, while too much detergent can completely remove the membrane lipid molecules. In order to find the optimum detergent/protein ratio for solublization, a protein concentration assay was performed using a modified BCA method (see section 2.5). After the protein concentration determination, the *R. s.* cytoplasmic membrane sample was diluted with buffer to make solutions with different protein concentrations. Different concentrations of dodecyl maltoside were added and the effects of the amount of detergent on the yield of purified protein and the protein crystallization ability were observed. It was found that a final dodecyl maltoside concentration of approximately 1.0% in a protein solution of approximately 10mg/ml was suitable. At this relatively low detergent concentration, not all of the protein was solublized from the membrane, as seen from the fact that only about 50% of the enzyme bound to the Ni^{2+}-NTA column. However, using this level of detergent concentration, apparently more lipids were retained during the process and crystals of the enzyme could be obtained reproducibly.

Purification of *Rs*C*c*O involved two purification steps, a Ni affinity column purification followed by an ion exchange column purification. In order to obtain crystals of C*c*O, the second column purification step was changed from a DEAE-5PW column, which might be more lipid-extracting due to the more hydrophobic nature of its column matrix material, to a Mono Q column, which was used by Iwata's group to obtain *Rs*C*c*O crystals (Svensson-Ek *et al.*, 2002).

Figure 3.2 shows the picture of a single crystal of *Rs*C*c*O obtained from *R. s.*

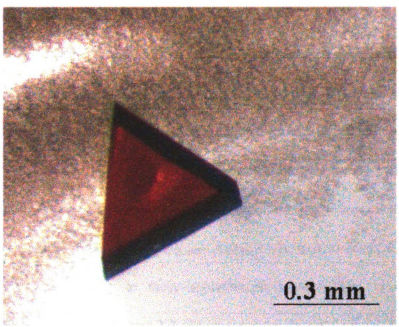

Figure 3.2: Crystal of the four subunit *Rs*CcO which belongs to a space group of *R*3.

strain 120 using the modified purification protocols. The exact crystallization conditions are as listed in section 2.12. The crystal has a triangular prism shape and belongs to the space group of *R*3 with a unit cell dimensions of $a = b = 340.7$ Å, $c = 90.6$ Å, $\alpha = \beta = 120°$, and $\gamma = 90°$.

3.1.3 UV/Visible Spectrum and Enzymatic Activity Assay of Purified *Rs*C*c*O

Figure 3.3 (A) shows the UV/visible spectra of purified oxidized *Rs*C*c*O (blue) and dithionite-reduced enzyme (purple) using the modified protein purification protocol. The purity of the enzyme preparation was judged by the ratio of A_{280}/A_{421} ratio for oxidized enzyme, which was approximately 2.0. In the case of the reduced enzyme, the Soret to α-band ratio ($A_{445\text{-}490}$/ $A_{606\text{-}630}$) was approximately 5.5. Both of these values were similar to those reported previously (Zhen *et al.*, 1998; Svensson-Ek *et al.*, 2002). Figure 3.3 (B) shows the reduced – oxidized difference spectrum of purified *Rs*C*c*O for crystallization. The α peak at approximately 606 nm appeared to be normal (Hosler *et al.*, 1992; Zhen *et al.*, 1998).

The turnover number of the purified wild type *Rs*C*c*O was determined polarographically to be about 1400 s^{-1} at room temperature by measuring the oxygen consumption rate. The turnover number was similar to that from wild type enzyme purified using the previous purification procedure (Zhen *et al.*, 1998).

3.1.4 Retention of Subunit IV during the Purification and Crystallization of *Rs*C*c*O

One important question to ask was whether the fourth subunit was overexpressed and successfully retained after the protein purification procedure and

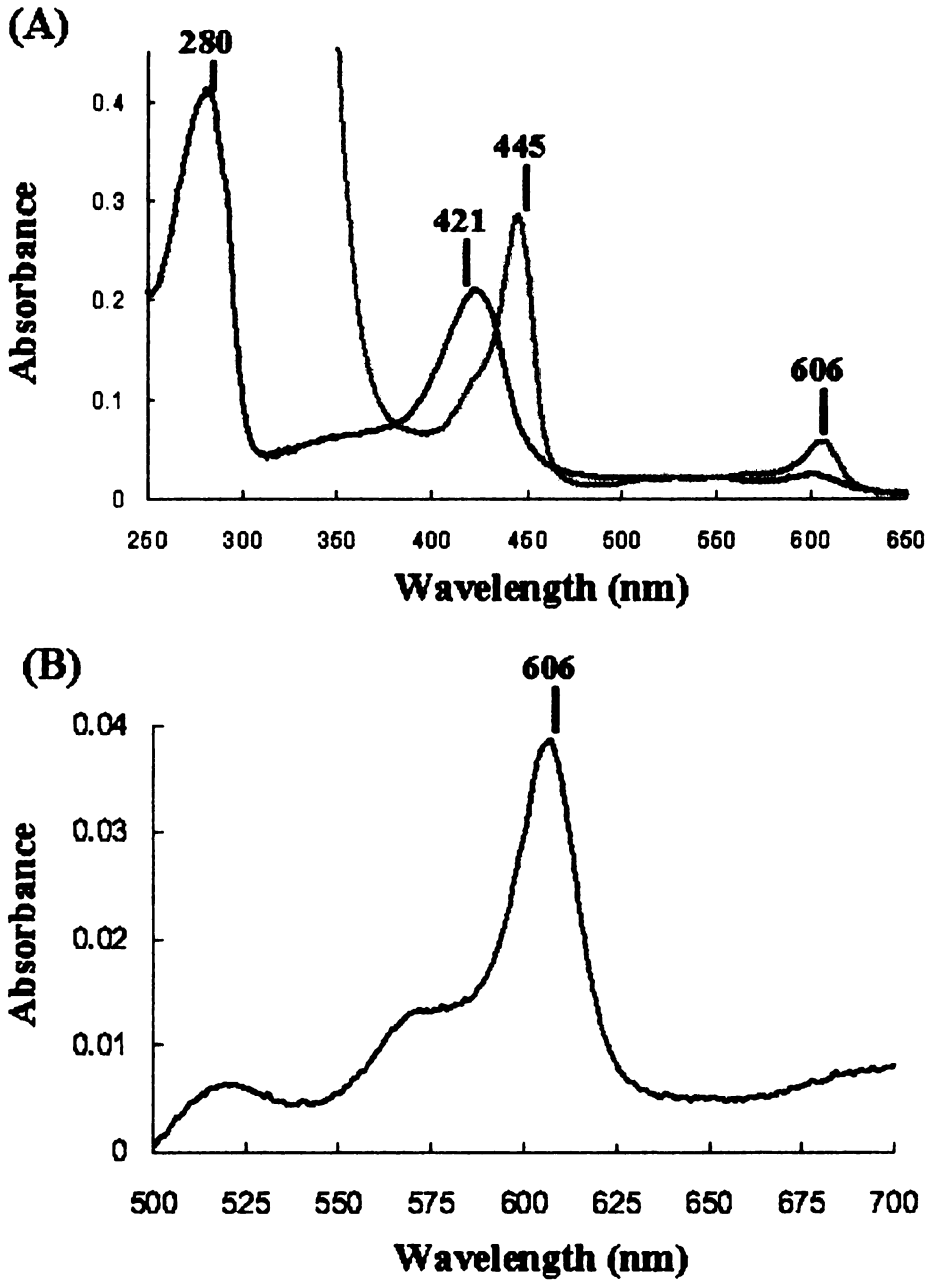

Figure 3.3: UV-visible spectra of purified *Rs*CcO. (A): Oxidized (blue) and dithionite-reduced (purple) spectra of *Rs*CcO. The A_{280}/A_{421} in the oxidized spectra is approximately 2, and the Soret to α-band ratio ($A_{445\text{-}490}$ / $A_{606\text{-}630}$) is approximately 5.5. (B): Dithionite-reduced minus ferricyanide-oxidized difference spectrum (green) of *Rs*CcO.

whether the crystals formed had stoichiometric amounts of subunit IV in them. In order to answer this question, both purified enzyme samples and re-dissolved *Rs*C*c*O crystals were subjected to a series of SDS-PAGE gels and the subunit contents were analyzed.

Figure 3.4 (A) shows the SDS-PAGE of purified *Rs*C*c*O from two different *R. s.* strains: 119, which expressed all four subunits of *Rs*C*c*O; and 25-1, which was used for crystallization trials previously and only overexpressed subunits I, II, and III. *Rs*C*c*O from strain 119 (Lane 1) was purified with both a Ni column and a Mono Q column, while *Rs*C*c*O from strain 25-1 (Lane 2) was purified with a Ni column only. It can be seen that the intensity of the band representing subunit IV in Lane 1 was greater than that in Lane 2 although the latter sample underwent only Ni column purification. Therefore, the relative amount of subunit IV in C*c*O from *R. s.* strain 119 is much higher than that from strain 25-1. Although quantitative assessment of the subunit IV content in the enzyme preparation was not possible, the density of the subunit IV band in SDS-PAGE did qualitatively indicate a higher subunit IV content, presumably due to overexpression of its gene and the modified purification procedures. Also in Figure 3.4 (A), two different bands with different apparent molecular weights in SDS-PAGE can be seen. The upper band represents the long form of subunit IV, which was overexpressed in strain 119. The lower band of subunit IV found in the C*c*O sample from 25-1 represents the short form of subunit IV. Since in strain 25-1, subunit IV was not overexpressed in plasmid, such an observation seems to indicate that native translation of subunit IV starts with the second starting

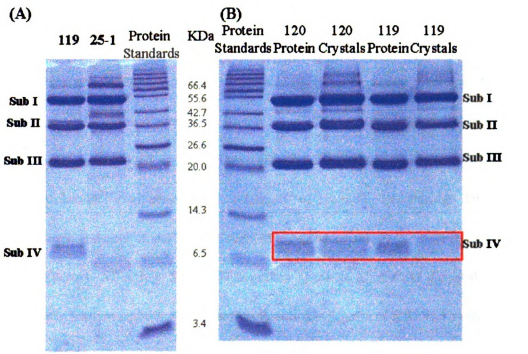

Figure 3.4: SDS-PAGE of purified enzyme and re-dissolved crystals of *Rs*CcO. (A): Purified *Rs*CcO from *R. s.* strain 119 and 25-1 with the different subunits labeled. (B): Purified enzyme and re-dissolved crystals of *Rs*CcO showing the different subunits as labled. The overexpression plasmid of *R. s.* strain 119 contains: his-tagged subunit I, shortened subunit II, complete subunit III, and long form of subunit IV. The overexpression plasmid of *R. s.* strain 120 contains: his-tagged subunit I, complete subunit II, complete subunit III, and long form of subunit IV. The overexpression plasmid of *R. s.* strain 25-1 contains: his-tagged subunit I, shortened subunit II, and complete subunit III only.

codon, although it is also possible that the long form of subunit IV undergoes proteolytic cleavage with the product being the short form of subunit IV. Identification of alternative starting points of translation and proteolytic cleavage processes of subunit IV of *Rs*C*c*O samples from other strains of *R. s.* were examined using mass spectrometry and will be discussed in later sections (see section 3.2.1).

Figure 3.4 (B) shows the SDS-PAGE of purified *Rs*C*c*O together with re-dissolved crystals from *R. s.* strains 120 and 119. It can be seen that subunit IV was present in significant amounts in all four lanes of C*c*O samples, in both the purified enzyme and re-dissolved crystals. Therefore, the overexpression of subunit IV by using molecular engineering and retention of subunit IV during detergent solublization and column purification seemed to be successful.

3.1.5 Factors Affecting X-Ray Diffraction Quality of *Rs*C*c*O Crystals and Systematic Improvements of Diffraction Resolution Limits of *Rs*C*c*O Crystals

3.1.5.1 Effect of Homogeneous Form of Subunit II

Although crystals of *Rs*C*c*O could be routinely obtained using the new *R. s.* strains and with the modified protein purification procedures, the X-ray diffraction quality of the C*c*O crystals obtained from strains 120 and 119 was poor. The best C*c*O crystals from strain 119 diffracted X-rays to a limit of 3.6 Å resolution, while all C*c*O crystals from strain 120 only diffracted to > 4 Å. Since the difference between strains 120 and 119 was the overexpression of native subunit II vs. truncated subunit II, such an observation suggested that different forms of subunit II could play an important role in the crystal diffraction quality.

It was well known that subunit II of *Rs*C*c*O undergoes incomplete proteolytic processing of its C-terminal amino acid residues (Hosler *et al.*, 1992). The processing site was thought to be after the residue $Ser290_{II}$ based on mass spectrometry analysis (Hiser *et al.*, 2001). Such a processing could not be prevented by adding different protease inhibitors to protein samples during purification, nor would it go to completion, and FPLC purification could only partially separate these two forms (Hosler *et al.*, 1992; Zhen *et al.*, 1998).

Figure 3.5 (A) shows the FPLC elution profile from Mono Q column purification of C*c*O obtained from *R. s.* strain 120. It can be seen that there were two very closely associated elution peaks, peak 1 and peak 2, followed by an elongated tail, as the concentration of KCl increased. As shown in Figure 3.5 (B), SDS-PAGE of the two peaks indicated that the first peak had mostly the long, intact form of subunit II, while the second peak contained mostly the short, processed form of subunit II. Although *R. s.* strain 120 expresses the full length subunit II sequence in its overexpression plasmid, due to natural processing of the C terminus, mixed populations of both intact and naturally processed forms of subunit II were present. These two different forms of subunit II coexisted in the purified *Rs*C*c*O complex and *Rs*C*c*O molecules with both forms of subunit II were incorporated into the crystal as shown in Figure 3.5 (C). Such an inhomogeneity in the protein sample might be the reason why C*c*O crystals obtained from strain 120 were of significantly less quality than those from strain 119.

In order to improve the crystal diffraction resolution, two forms of the subunit

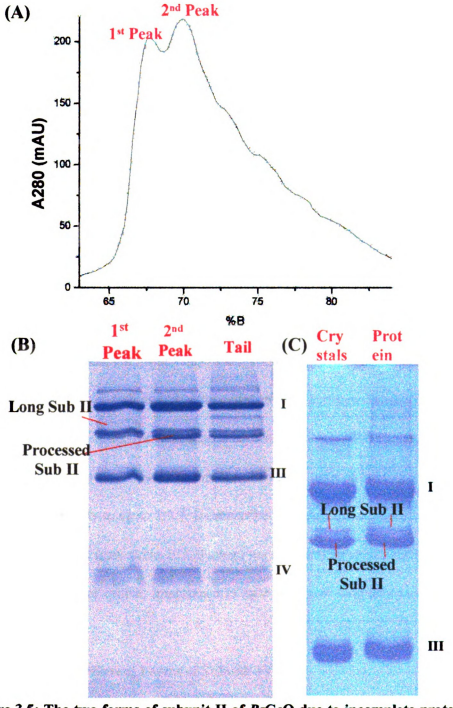

Figure 3.5: The two forms of subunit II of *Rs*CcO due to incomplete proteolytic processing of the C-terminal 13 amino acids. (A): FPLC elution profile of Mono Q column purification of *Rs*CcO obtained from *R. s.* strain 120 showing the two closely associated peaks. (B): SDS-PAGE of the fractions under the first and second peak from the FPLC purification shown in (A). The first and second peaks represent *Rs*CcO with the intact and processed subunit II, respectively. (C): SDS-PAGE of the purified enzyme and re-dissolved crystals of *Rs*CcO from strain 120. The two forms of subunit II coexist in both purified enzyme and in the re-dissolved crystals.

IV gene, the long form of subunit IV starting with the first starting codon, and the short form of subunit IV starting with the second starting codon, were individually inserted into an overexpression plasmid which contained the artificially truncated form of subunit II. The overexpression plasmid was then conjugated into a parental *R. s.* strain YZ200 that contained no subunit II or subunit III (Zhen *et al.*, 1998), to eliminate any expression of native subunit II from the bacterial genome. Two new *R. s.* strains, 156 and 163, overexpressed *Rs*C*c*O containing all four subunits with the histidine tag on the C terminus of subunit I, the artificially truncated form of subunit II, and the long form and short form of subunit IV, respectively (see Table 2.1). For some reason that was not completely understood, the protein expression levels of strains 156 and 163, as well as 119, were extremely low compared to those from other strains, which made extensive screening of crystallization and flashcooling conditions very difficult. However, it was clear that the diffraction limit of the C*c*O crystals was improved moderately to up to 3.3 Å for *Rs*C*c*O crystals obtained from strain 156 and to 3.2 Å for crystals from strain 163. Such an improvement in crystal diffraction limit indicated that it is of critical importance to have only one form of subunit II in the C*c*O sample.

3.1.5.2 Effects of Different Forms of Subunit IV

Since the natural subunit IV gene contained two potential starting codons, efforts were made to clone the long and short forms of subunit IV gene separately and the effects of the two forms on the crystal diffraction quality were compared (see Figure 2.1 for the amino acid sequence of subunit IV and two potential N termini).

Comparisons of effects of different subunit IVs on crystals were made on C*c*O crystals obtained from strains 120 and 157, and from strains 156 and 163. While crystals obtained from strain 120, which overexpressed the long form of subunit IV, diffracted generally > 4 Å, crystals obtained from strain 157, which overexpressed the same subunits as strain 120 except for the short subunit IV, diffracted X-rays to approximately 4 Å. A slightly better diffraction limit for crystals from the *R. s.* strain overexpressing the short subunit IV was also observed by comparing C*c*O crystals obtained from strain 163 and 156 as shown in the previous section. Therefore, it seems that the presence of short subunit IV was more beneficial to the *Rs*C*c*O crystal diffraction than the long subunit IV.

It should be noted that the above observations of diffraction limits of C*c*O crystals were not based on just a few crystals from each strain of *R. s.* Because of the great crystal to crystal variation, usually tens of crystals from each strain, sometimes from different batches of bacterial growth and protein purification, were tested at the synchrotron for diffraction limits before a generalized idea of the resolution limit could be made.

3.1.5.3 Crystallization of Subunit II Histidine-Tagged *Rs*C*c*O and its Crystal Structure

Previously, subunit II histidine-tagged *Rs*C*c*O was engineered and expressed in our group in an effort to improve the purity of vesicles of C*c*O by allowing metal affinity purification of only those reconstituted vesicles with correctly oriented C*c*O molecules in them (Hiser *et al.*, 2001). In this form of enzyme, a 6-histidine tag was

attached to the shortened C terminus of subunit II as shown in Figure 2.1. In order to test if subunit II histidine-tagged *Rs*C*c*O was a better candidate for crystallization, long and short forms of subunit IV were incorporated into the overexpression plasmid containing the histidine-tagged subunit II. The overexpression plasmids were then conjugated into parental *R. s.* strain YZ200 to make strains 167 and 169, respectively (see Table 2.1). The histidine tag at the C-terminus of the truncated subunit II not only facilitated Ni-affinity column purification of the enzyme, but also provided a uniform form of subunit II, whose critical importance in crystal quality had been observed. It was thought that since the C-terminal end of subunit II is located on the surface of the extra-membrane domain, which is very close to the crystal contact surface as shown in Figure 3.1, the presence of six histidine residues at this region might contribute to new crystal contacts via polar interactions between the histidine tag and residues from another molecule.

The protein expression levels of both strains 167 and 169 were satisfactory and moderate improvements in the diffraction limits of C*c*O crystals were observed. When combined with other modifications during protein purification, crystallization and flashcooling of crystals (see later sections in this part), the best crystals obtained from *R. s.* strain 167 diffracted X-rays up to 3.1 Å and the best crystals obtained from strain 169 diffracted X-rays up to 2.9 Å. Datasets were collected from both crystals and structural refinement were carried out by using the original published four subunit *Rs*C*c*O structure (PDB entry 1M56) as the initial phasing model (Svensson-Ek *et al.*, 2002).

Table 3.1 shows the data collection and structural refinement of the two crystals obtained from *R. s.* strains 167 and 169, respectively. Due to the strong anisotropic diffraction, the completeness of both data sets was significantly lower than 100%. Such an anisotropic behavior is very common among the X-ray diffraction patterns from membrane proteins, and the published wild type four subunit *Rs*C*c*O crystal structure has an overall completeness of only close to 70%. Although the diffraction limit of the C*c*O crystal from strain 169 was a little further than that from strain 167 (2.9 Å vs. 3.1 Å), the quality of the electron density maps and the final R-factor and R_{free} were very close to each other at about 27% and 32% for R-factor and R_{free}, respectively. The refined structure discussed here was from the crystal obtained from *R. s.* strain 167. In fact, the electron density maps of the crystal from strain 167 revealed more interesting features than that from strain 169, as described later.

3.1.5.3.1 Overview of the Subunit II Histidine-Tagged Four Subunit *Rs*C*c*O Structure

The structure of the subunit II histidine-tagged C*c*O was highly homologous to that of the published four subunit C*c*O structure with a histidine tag attached to the C-terminus of subunit I. The electron density maps of the main chains of the transmembrane helices were clear, including the single transmembrane helix of the newly-found subunit IV. The amino acid residues in transmembrane helices, particularly those buried in the center of the protein were generally better resolved compared with those on the surface and in the loop regions. Due to the relatively low

R. s. Strain	167	169
A. Unit Cell Parameters		
Space Group	*R*3	*R*3
Cell Dimensions (Å)	*a*=*b*=339.5 *c*=89.1	*a*=*b*=339.4 *c*=89.3
No. Molecules per A.U.	2	2
B. Data Collection		
Resolution Range (Å)	40-3.1 (3.21-3.1)	30-2.9 (3.0-2.9)
Completeness (%)	73.0 (42.8)	74.7 (33.4)
No. Unique Reflections	50,721 (2,966)	63,444 (2,841)
Overall Redundancy	6.3 (2.6)	5.1 (3.7)
Overall R_{merge} (%)	6.5 (32.8)	8.2 (30.5)
C. Structural Refinement		
R-factor / R free (%)	27.1 / 32.5	26.7 / 31.5
Average B-factor	101.4	113.5
Non Cryst. Symmetry	restrain	restrain
F / sigma Cutoff	2.0	2.5
R.m.s.d Bond Lengths (Å)	0.011	0.011
R.m.s.d Bond Angles (°)	1.50	1.48
No. of Atoms	17878	17809

$R_{merge} = \Sigma \mid I_h - \langle I_h \rangle \mid / \Sigma I_h$ over all h, where I_h is the intensity of reflection h. R-factor= $\Sigma \mid |Fo| - |Fc| \mid / \Sigma |Fo|$; where Fo and Fc are the observed and calculated structure factors, respectively. The completeness and number of unique reflections values were obtained from CNS refinement result file after F/sigma cutoff was applied. Redundancy and R_{merge} values were obtained from the program Scalepack. Values in parentheses are parameters for the highest resolution shell.

Table 3.1: X-ray data collection and refinement statistics of *Rs*CcO crystals obtained from *R. s.* strain 167 and 169.

resolution and quality of the dataset, as well as possibly more mobility of the side chains, several amino acids on the surface of the protein, most of which should have been lysines and arginines, were assigned as alanines because no side chain electron densities were observed. Solvent molecules, such as waters, were not assigned due to the relatively low resolution limit of the data.

The redox active metal centers and the porphyrin rings of the heme groups were better resolved, as well as the important ligating amino acid residues. Figure 3.6 shows the structure of heme a_3 – Cu_B binuclear center with the $(2F_o - F_c)$ difference electron density map contoured at 1σ level. The ligating residues of the heme a_3 Fe and Cu_B atoms are also shown in Figure 3.6, together with a nearby residue $Y288_I$. Although there is strong evidence for a linkage of $Y288_I$ to one of the Cu_B ligands, $H284_I$, through the side chain ring atoms from the two residues (Tsukihara *et al.*, 1996; Ostermeier *et al.*, 1997; Buse *et al.*, 1999), no efforts were made to try to model in such a covalent bond due to the limited resolution.

3.1.5.3.2 Partial Lipid Molecules

In the published four subunit C*c*O crystal structure, a total of 6 phosphatidyl ethanolamine (PE) molecules per C*c*O molecule were resolved. Four of them were found to surround subunit IV at the interface between subunit IV and subunits I and III, while the other two PEs were found in the V-shaped cleft formed by transmembrane helix bundles inside subunit III and close to the interface of subunits I and III as shown in Figure 1.4 (Svensson-Ek *et al.*, 2002). In the current structure, although no complete PE molecules were resolved, a total of 11 partial PE molecules

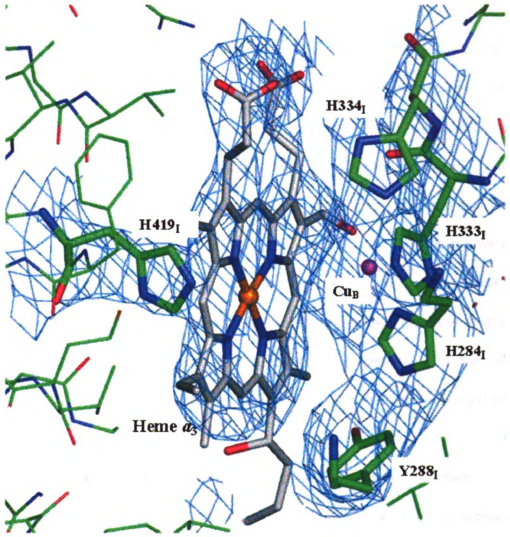

Figure 3.6: The active site consisting of heme a_3 and Cu_B in the structure of the four subunit *Rs*CcO. The $(2F_o - F_c)$ difference electron density map contoured at 1σ is shown in blue. The amino acid residues including the ligands of the heme a_3-Fe (orange) and Cu_B (purple) are colored by atom type.

were found in the two C*c*O molecules in an asymmetric unit. Figure 3.7 shows some of these partially resolved PE molecules (colored by atom type) together with the resolved PE molecules in the published structure (yellow). For some of these molecules, only the phosphate group, the glycerol backbone, and the beginning of the ester linkage were resolved as shown in Figure 3.7 (A). For some others, the ethanolamine head group was additionally resolved as shown in Figure 3.7 (B). Sometimes, part of one or two fatty acid chains of the lipid molecules were also resolved as shown in Figure 3.7 (C) and (D). It can also be seen that both the overall positions and detailed conformations of these lipid molecules are almost identical in the two structures in spite of the differences in the histidine-tag positions, and the slight differences in purification and crystallization procedures. Therefore, the presence of these partial PE molecules indicated that these lipids are an integral part of the entire structure.

3.1.5.3.3 Potential Histidine-Tag Resolved at the Crystal Contact Interface

As shown in Figure 3.1 and Figure 3.8 (A), the key crystal contact occurs at the interface between the bottom part of one molecule including mostly the N-terminal cytoplasmic region of subunit IV, and the corner between the globular domain of subunit II and the flat surface formed by subunits I and III. The C-terminus of subunit II is not located within the crystal contact interface, but is in close proximity. Part of the reason why subunit II histidine-tagged C*c*O was used as a crystallization candidate was that the histidine-tag might contribute to formation of new crystal contacts in this region by assuming a new, stable conformation different

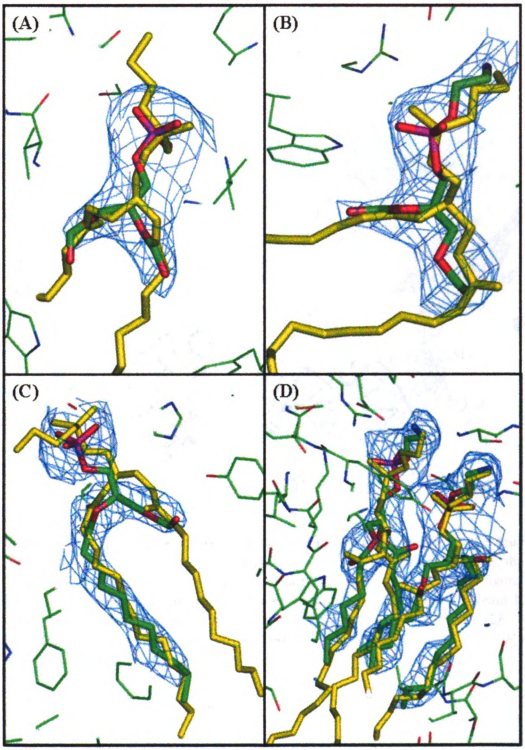

Figure 3.7: Partial lipids resolved in the structure of the four subunit *Rs*CcO. The resolved lipids are shown by sticks and colored by atom type (C: green; O: red; N: blue; P: purple), while those resolved in the published four subunit *Rs*CcO structure (PDB entry 1M56) are shown in yellow. Different portions of the lipids are resolved in the current structure compared with the published crystal structure as shown in (A), (B), (C), and (D).

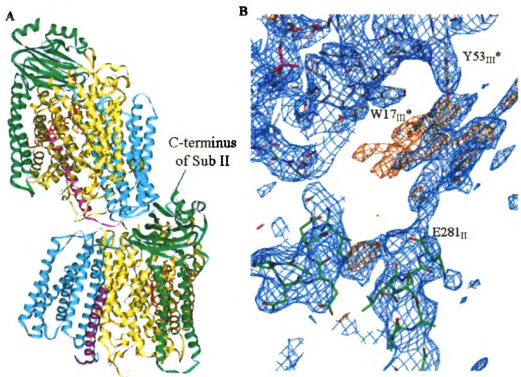

Figure 3.8: Major crystal contact regions in the crystal structure of the four subunit *Rs*CcO. (A): Although not directly involved in forming crystal contacts, the C-terminus of subunit II is close to the crystal contact regions as labeled in the figure. (B): Extra pieces of electron density are seen between the C-terminus of subunit II ($E281_{II}$) and regions of another *Rs*CcO molecule ($W17_{III}$* and $Y53_{III}$*) in the ($2F_o - F_c$) difference electron density map contoured at 1σ (blue) and in the ($F_o - F_c$) difference electron density map contoured at 2.5σ (orange).

from the conformation of the C-terminus of subunit II as seen in the published crystal structure. Analysis of the C*c*O crystal obtained from *R. s.* strain 167 seemed to suggest that it was possible that the engineered histidine-tag could be making new crystal contacts.

Figure 3.8 (B) shows the ($2F_o$ - F_c) difference electron density map contoured at 1σ (blue) and the (F_o - F_c) difference electron density map contoured at 2.5σ level (orange) in the area immediately adjacent to the shortened C-terminal residue of subunit II ($E281_{II}$) right before the histidine tag. A large electron density feature could be seen which seemed to connect the C-terminus of subunit II to areas from another molecule. This continuous piece of electron density could contain the engineered histidine tag, which might suggest that the histidine tag had been immobilized and contributed to crystal contacts. However, due to the limited resolution and the relatively poor quality of the electron density, the model building of the histidine tag was not aggressively pursued. Similar electron density was not observed in this area in the structure of the crystal obtained from *R. s.* strain 169 although it also possessed a histidine-tagged subunit II. When another refinement program, Refmac5, was used, this piece of electron density also disappeared.

3.1.5.4 Retention of Membrane Lipids in Detergent Solublization, Protein Purification and Crystallization

3.1.5.4.1 Identification of Lipid Species during Purification and Crystallization

The importance of native membrane lipids in membrane protein crystallization is getting more attention as more high resolution membrane protein crystal structures

are found to contain membrane lipids in them. Such tightly and specifically bound lipids stabilize the native conformations of membrane proteins and contribute to the homogeneity of membrane protein samples which is crucial to crystallization efforts. In the published crystal structure of the four subunit C*c*O, a total of 6 phospholipids were resolved, all of which were assigned as phosphatidyl ethanolamine (PE). They reside in the crevices and interfaces between subunits (Figure 1.4). Besides their obvious role of securing the presence of subunit IV, it is very conceivable that the complete or partial loss of these lipids might also lead to non-uniform conformations of the transmembrane helices and thus inhomogeneity of the protein samples. Therefore, efforts were made to analyze the lipid content during the protein purification processes and to modify protein preparation protocols in order to retain more important lipid species bound to protein complexes. Thin layer chromatography (TLC) analysis of lipid species of C*c*O samples at different purification stages showed diminishing amount of lipids as the purification steps went along. These included phospholipids PE, PC, PG, PS, and non-phospholipids such as SQDG and ornithine lipids (Hilmi, 2002). As the TLC requires relatively more sample (0.2 mg), as well as lipid extraction which could lead to its oxidation and loss, matrix-assisted laser desorption-ionization time of flight (MALDI-TOF) mass spectrometry was applied as an assay method to detect lipid species (Distler *et al.*, 2004). Different lipid species could be detected preferentially using MALDI mass spectrometry with the use of different matrix molecules in both linear positive and negative ion modes. Post source decay (PSD) ion mode was also used to confirm the identities of some of the lipid

species by matching fragmentation patterns with lipid standards.

Figure 3.9 shows the MALDI-TOF mass spectra of lipids detected in *R. s.* membranes and C*c*O samples at various stages of purification using both positive and negative ion modes. In the detergent solublized *R. s.* membrane sample, as shown in Figure 3.9(A), a variety of phospholipid species were detected using the positive ion mode, including PC, PE, PG and CDL, while PG, SQDG, and CDL were identified in the negative ion mode. It should be noted that an important phospholipid, CDL, which was not identified using the TLC system previously employed, presumably due to its comigration with pigments and hemes, and its tendency to run off the top of the TLC plate, was successfully detected by mass spectrometry, especially when the negative ion mode was used.

Figure 3.9 also shows the mass spectra of the lipid region of both the two-step column-purified C*c*O sample and the re-dissolved four subunit C*c*O crystals using positive ion mode (B) and negative ion mode (C). It can be seen that certain lipid species were selectively retained after the protein purification and crystallization procedures, including PC, PE, PG, SQDG, and CDL, all of which were detected in the mass spectra shown. Although the published crystal structure had only PEs in its model, mass spectra of re-dissolved crystals clearly showed the presence of more lipid species, including CDL, which had been previously suggested to play key roles in C*c*O activity (Robinson, 1982). Due to the lack of an accurate standard, quantification of each of the lipid species from the peak height was not reliable and thus no

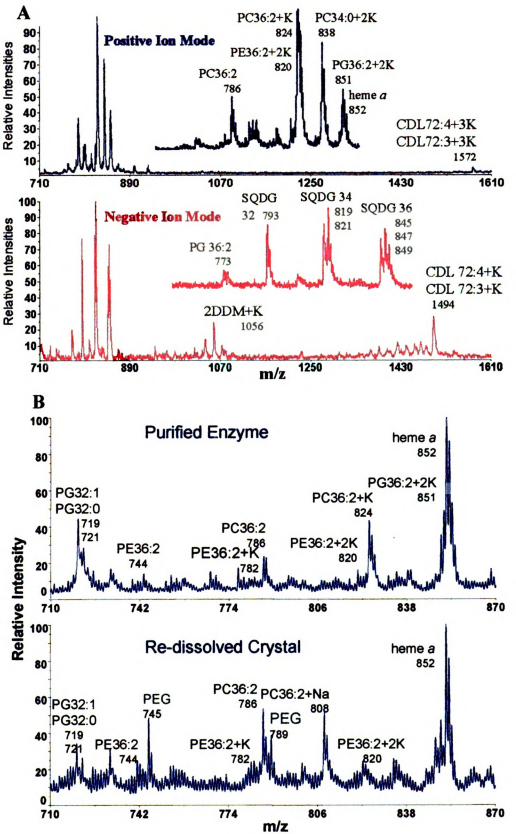
A
Positive Ion Mode
Relative Intensities
PC36:2+K
824
PC34:0+2K
838
PE36:2+2K
820
PG36:2+2K
851
PC36:2
786
heme a
852
CDL72:4+3K
CDL72:3+3K
1572
710
890
1070
1250
1430
1610
Negative Ion Mode
SQDG
32 793
SQDG 34
819
821
SQDG 36
845
847
849
PG 36:2
773
CDL 72:4+K
CDL 72:3+K
1494
2DDM+K
1056
m/z
B
Purified Enzyme
heme a
852
PG32:1
PG32:0
719
721
PE36:2
744
PC36:2
786
PE36:2+K
782
PE36:2+2K
820
PC36:2+K
824
PG36:2+2K
851
Relative Intensity
Re-dissolved Crystal
heme a
852
PG32:1
PG32:0
719
721
PE36:2
744
PEG
745
PC36:2
786
PC36:2+Na
808
PEG
789
PE36:2+K
782
PE36:2+2K
820
m/z

Figure 3.9

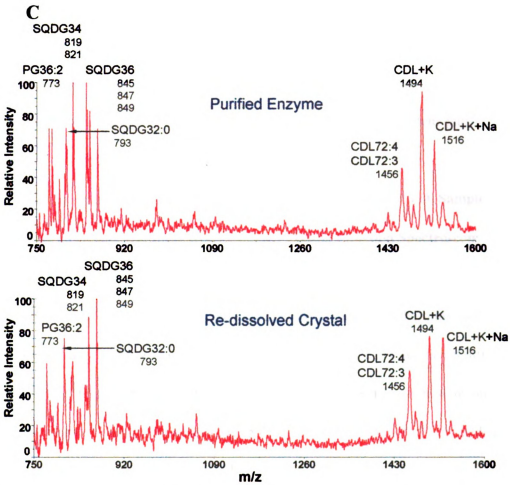

Figure 3.9: Lipids content analyses of *Rs*CcO samples at different purification stages using MALDI mass spectrometry. (A): MALDI mass spectra of detergent solubilized *R. s.* cell membranes using positive (blue) and negative (red) ion mode. The inset of each spectrum shows the detailed spectra of the m/z region from 710 to 850. Different lipid species are labeled as in the figure. (B): MALDI mass spectra of purified *Rs*CcO (top panel) and re-dissolved *Rs*CcO crystals (bottom panel) using positive ion mode. Different lipid species are labeled as in the figure. (C): MALDI mass spectra of purified *Rs*CcO (top panel) and re-dissolved *Rs*CcO crystals (bottom panel) using negative ion mode. Different lipid species are labeled as in the figure.

comparative analyses of the amounts of the lipid species between the purified CcO and CcO crystals were possible. However, approximate relative amounts of different lipids could be determined and due to its relative ease and quickness, and the fact that it only requires a very small amount of sample, mass spectrometry proved to be a valuable routine assay for detection of lipid species during the protein purification process.

3.1.5.4.2 Quantitative Analysis of Phospholipid Content of CcO Samples by Phosphorous Assay and Inductively Coupled Plasma Emission Spectroscopy

One quantitative method of analyzing phospholipid content was to perform a phosphorous assay to determine the relative content of phospholipids per CcO molecule. Table 3.2 shows the phosphorus content of a set of CcO samples at different stages of protein purification. It can be seen that as the purification went on, the number of phosphorous atoms per CcO molecule decreased from 15-18 immediately after the Ni column, to approximately 5-7 after the second column followed by washing and detergent exchange. When only the Ni column was used to purify the protein, the number of phosphorous per CcO molecule after washing and detergent exchange was similar or slightly higher ($\approx$ 7) than in the samples after two purification steps. Significant reduction in phosphorous was observed with increased number of washes (Table 3.2). Although the phosphorous assay gives important information about the relative amount of phospholipids (including CDL which has two phosphorous atoms per molecule), it requires relatively more sample (a few mg) and cannot give information about non-phosphorous lipids. Therefore, its usefulness

Sam-ple #	Sample Descriptions	[P](μM) / [C*c*O](μM)
1	*R. s.* cytoplasmic membrane	≈ 3600
2	C*c*O fractions after Ni Column	16.6
3	after Ni column + washing*	7
4	after Ni + Mono Q + washing*	6.9
5	after Ni + DEAE Sepharose + washing*	5.2 – 7.3
6	after Ni + Superdex 200 + washing*	6.8
7	after Ni + Mono Q column purification, 6x washing instead of 2-3x	3-5

*: washing involves first concentrating the volume of the pooled fractions from column chromatography to under 0.5 ml through ultrafiltration, then filling the concentrator with new solution and concentrating the solution to under 0.5ml again. The process is repeated a number of times to ensure complete exchange of buffer the sample is in. The number of times refilling the concentrator with new buffer solution is usually 2-3 times.

Table 3.2: Phosphorous contents of various *Rs*C*c*O samples measured by colorimetric method.

in routine lipid quantification is limited, particularly with limited protein samples.

Mineral analysis by inductively coupled plasma emission spectroscopy (ICP) was also performed to further quantity the elemental contents, including metals and phosphorous. Information on the phosphorous content could be obtained directly from the elemental analysis. Table 3.3 shows the result of ICP analysis of different C*c*O samples. In this table, the phosphorous content was calculated from the ratio of the molar concentration of phosphorous over the concentration of enzyme derived from the molar concentration of copper divided by three, since it is known that there are three coppers per one C*c*O molecule. The Cu concentration was used as the reference for phosphorous because it appeared most consistent with the known amount of enzyme used for the assay and also provided an internal standard. It can be seen from Table 3.3 that there were 6-8 phosphorous atoms per C*c*O molecule, which was close to what was measured using the phosphorous assay as described above, and that there was not a clear difference in the phosphorous contents among the samples purified with a Ni column only, Ni plus Mono Q columns, or Ni plus DEAE sepharose columns, as observed by phosphorous analysis. Also consistent with the phosphorous analysis (Table 3.2) is the observed reduction in phosphorous content with more washing (Table 3.3). Although ICP is an accurate method, it requires a lot of sample (approximately 10 mg) and time to obtain the results and thus is not suitable as a routine assay.

3.1.5.4.3 Modification of Protein Purification and Crystallization Procedures to Retain More Bound Membrane Lipids

Sample[1]	[Cu] (ppm)	[Cu] (μM)	[Cu]/3 (μM)	[Fe] (ppm)	[Fe] (μM)	[Fe]/2 (μM)	[Mg] (ppm)	[Mg] (μM)	[P] (ppm)	[P] (μM)	[P]/ [CcO][7]
buffer blank	0.27			0.58			0.15		<1.0		
Ni[2]	70.0	1097	366	41.6	734	367	6.82	278	94.1	3022	8.2
MQ-1[3]	61.4	962	321	30.6	538	269	5.92	240	71.0	2276	7.1
DS-1[4]	66.6	1044	348	31.5	554	277	6.53	266	64.0	2050	5.9
DS-2[5]	71.3	1121	374	41.7	747	374	9.80	381	98.2	3170	8.5
MQ-2[6]	64.9	1017	339	29.8	523	261	5.96	242	50.8	1624	4.8

1. All samples were from *R. s.* strain 167 but differently treated, and from different batches of enzyme, as indicated 2. C*c*O purified with Ni column only and washed for 2-3 times 3. C*c*O purified with Ni column and Mono Q column and washed for 2-3 times 4. C*c*O purified with Ni and DEAE sepharose column and washed for 2-3 times 5. Another batch of C*c*O sample purified with Ni column and DEAE sepharose column and washed for 2-3 times, tested separately 6. Another batch of C*c*O sample purified with Ni and Mono Q column, but the washing and detergent exchange procedures were performed 6 times rather than 2-3 times (details in later sections) 7. [p]/[CcO] is calculated from the ratio of the molar concentration of phosphorous over one third of the molar concentration of Cu.

Table 3.3: Phosphorous contents of various *Rs*C*c*O samples measured using ICP.

Since the retention of membrane lipids is of great importance, modifications of the protein purification and crystallization were made in order to retain the important lipid species bound to the protein complex.

3.1.5.4.3.1 Modification of Detergent Concentration used for Membrane Solublization

The first and possibly the most important way to retain bound native lipids was to control the amount of detergent used for membrane solublization. As described earlier in section 3.1.2, the protein concentration in the membrane sample was determined prior to membrane solublization and the detergent dodecyl maltoside was added at a final concentration of 1% to the membrane sample at a protein concentration of 10 mg/ml. This was important because too much detergent relative to protein would likely strip off the bound lipids and possibly subunit IV as well. In fact, when the detergent concentration was doubled, no crystals were obtained.

3.1.5.4.3.2 Modification of Column Purification Methods

Modifications during column purifications were also made in order to retain more bound lipids. In the hope of retaining more lipids, DEAE sepharose ion-exchange column was used instead of a Mono Q column, providing a different matrix support which might interact differently with lipids. Although phosphorous content measurements using colorimetric analysis and ISP analysis did not show any improvement in the phospholipid content in the purified protein complex, the diffraction limit of C*c*O crystals was improved slightly. The two best crystals obtained from *R. s.* strains 167 and 169 were both purified by the DEAE sepharose column

following the Ni column. It is possible that protein purification using the DEAE sepharose column helped retain some non-phospholipid which were specifically bound to C*c*O. These lipids may also be important in maintaining an overall stable and homogeneous conformation of C*c*O molecules. In fact, non-phospholipids, such as SQDG, were routinely found in all C*c*O samples and crystals using TLC and MALDI mass spectrometry, but not specifically resolved in the structure.

In other attempts to retain lipids, only a single column purification step (Ni column) was used. When a simple linear imidazole gradient was used, there were two very closely associated elution peaks which were very hard to separate as shown in Figure 3.10 (A). Fractions from the first peak were brownish in color and contained C*c*O bound to a major contaminating species with an absorption peak at around 560 nm (Figure 3.10 (B)), while the second peak was green and contained much purer C*c*O (Figure 3.10 (C)). A second ion exchange column purification was usually able to remove the contaminant when all fractions under the two peaks were pooled. However, without further column purification, crystals were difficult to obtain. Therefore, a step gradient method as described in the Methods section was developed to separate the two closely-associated elution peaks during Ni column purification in order to obtain a reasonably pure C*c*O sample without a second chromatography step. Complete separation of the two peaks was achieved as shown in Figure 3.10 (D) by using the step gradient. Green fractions from the second peak were pooled and washed and detergent was exchanged. The improved Ni purification protocol required less time and handling, and could contribute to retention of more lipids that might

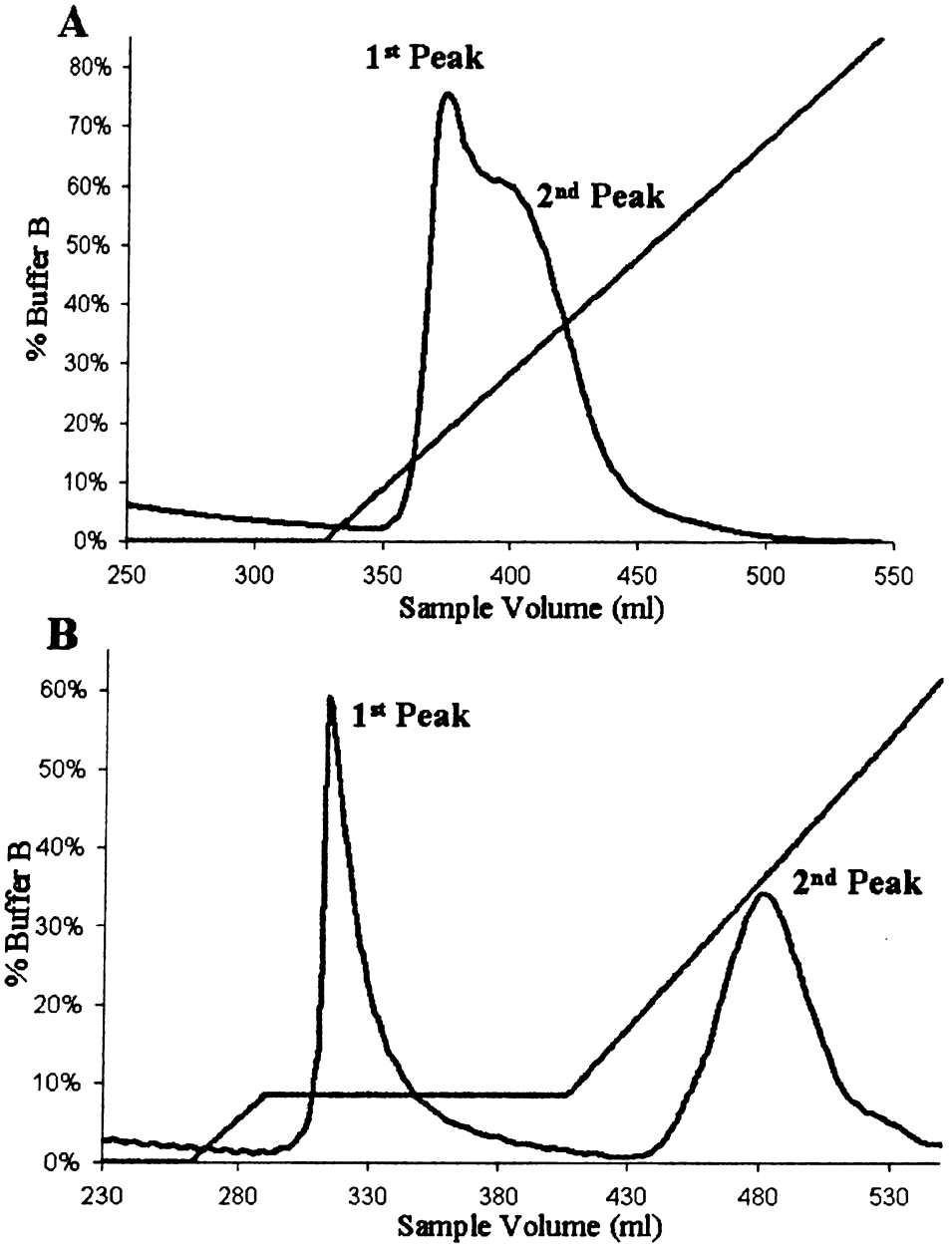
A
1st Peak
2nd Peak
% Buffer B
80%
70%
60%
50%
40%
30%
20%
10%
0%
250
300
350
400
450
500
550
Sample Volume (ml)
B
1st Peak
2nd Peak
% Buffer B
60%
50%
40%
30%
20%
10%
0%
230
280
330
380
430
480
530
Sample Volume (ml)

Figure 3.10

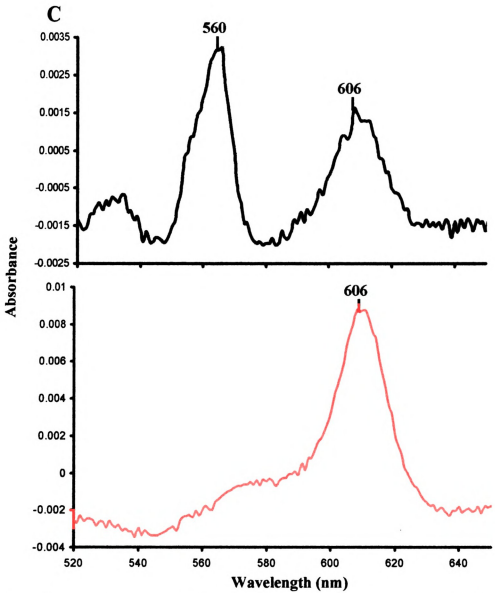

Figure 3.10: Elution profile of Ni-NTA affinity column purification of *Rs*C*c*O and the UV-visible spectra of the fractions under the two peaks during the elution process. (A): Two very closely related elution peaks (blue) were observed when a simple linear gradient of imidazole was applied (green). (B): The two peaks (blue) were completely separated when a step gradient of imidazole (green) was applied. (C): Comparison of the reduced minus oxidized spectra of the fractions under the first peak in the Ni column elution profile (top panel) and the fractions under the second peak (bottom panel). The wavelengths of the absorption peaks in each spectrum are labeled as in the figure.

otherwise be lost during a second column purification step. C*c*O crystals were routinely obtained from protein samples purified using the above method and the phosphorous content was similar to that after a two-column purification. However, the diffraction limit of the C*c*O crystals was worse compared with those obtained from C*c*O samples after the two-step column purification.

Comparing the phosphorous content of C*c*O samples immediately after the Ni column, and after the washing and detergent exchange, showed that the phosphorous content decreased significantly from 15-18 to 5-7 phosphorous atoms per C*c*O molecule. This result suggested that the washing and detergent exchange steps were responsible for stripping off the majority of the phospholipids. Therefore, efforts were made to optimize the procedure of enzyme washing and concentrating in order to retain more bound lipids. Previously, green fractions after the second ion exchange column purification were washed and concentrated 6 times by using a YM-100 filter (MW cutoff 100 kDa, maximum volume 15 ml) to ensure a thorough desalting and a complete detergent exchange. However, this washing procedure was found to lead to the loss of more lipids; the phosphorous content was lower (approximately 3-5 phosphorous atoms per C*c*O molecule) than when the sample was washed for 2 – 3 times (approximately 5-7 phosphorous atoms per C*c*O molecule). Thus, the number of times of washing was reduced to 2 – 3 times. The method of washing was later changed to the stirred ultrafiltration cell under nitrogen pressure (maximum volume 50 ml) with a YM-100 membrane disc (MW cutoff 100 kDa). The advantages of using this method included better efficiency of washing and detergent exchange due to a

larger working volume and thus fewer cycles of washing (2 x). Since the entire enzyme solution was constantly being stirred, there was no enzyme precipitate formed, which tended to happen when the enzyme solution was subjected to prolonged centrifugation. Moreover, oxidation of lipids should be lower during this process since there is little oxygen present in the ultrafiltration cell. The phosphorous content of the *Cc*O sample prepared in this way was similar to before and no improvement in X-ray diffraction quality was observed.

A different second chromatographic step, a Superdex 200 size exclusion column, was also tested and the effect on both the retention of lipids and X-ray diffraction quality was observed. The advantage of using this column was that the different matrix of the Superdex 200 column might bind to lipids less and thus not deplete lipids from the protein samples. Additionally, only a simple concentrating of *Cc*O sample was needed after the column since the detergent exchange was performed when the enzyme moved through the column pre-equilibrated with the new buffer. No improvement in crystal diffraction was observed by using *Cc*O prepared using this column.

3.1.5.4.3.3 Modification of Detergent and Lipids in the Crystallization Solution

In order to retain more bound lipids during crystallization, less detergent was used in the final enzyme solution with approximately 0.20% decyl maltoside instead of 0.24% decyl maltoside.The latter concentration was used by Iwata's group who published the first four subunit *Rs*C*c*O crystal structure. Crystals obtained with various concentrations of decyl maltoside suggested that if the decyl maltoside

concentration was lower than 0.16%, the crystal diffraction was worse, while there was no clear difference in diffraction among crystals obtained with conditions having 0.20% or 0.24% decyl maltoside. Therefore, the effect of such a modification was not clear.

In other attempts, dioleoyl-glycero-3-phosphoethanolamine (DOPE) or dioleoyl-glycero-3-phosphocholine (DOPC) were added into the crystallization mixture with the hope that they would bind to their native binding site(s) and contribute to the overall stable and homogeneous conformation of the protein sample. Unfortunately, addition of the membrane phospholipids did not lead to any crystals, or in a few instances led to crystals with almost no diffraction. This observation was in accordance with the observations made during the screening of secondary detergents when a few PCs with shorter acyl chain length (9-12) were used in the crystallization additive and no crystals were obtained. When a batch crystallization method was used, during which enzyme solution was mixed with crystallizing reagents and crystallization additives in a well, and the entire mixture was topped with immiscible oil, crystals were obtained with the addition of PE, but the diffraction was worse than without the addition of phospholipids.

3.1.5.5 Optimization of Detergent Choice, Crystallization Additives, Crystallization and Flashcooling Procedures

3.1.5.5.1 Optimization of Detergent(s)

Since crystallization of membrane proteins is essentially crystallization of protein-detergent complexes (PDCs), detergent molecules are the most important

variables in a membrane protein crystallization experiment, second only to the membrane protein itself. Crystallization of the four subunit *Rs*C*c*O requires two different detergents. First, dodecyl maltoside was used to solubilize the *R. s.* membrane and was also present in the buffers for the two-step column purification. After that, the detergent was exchanged to decyl maltoside by repeated washing and concentrating using either a centriplus filter unit or the stirred untrafiltration cell under nitrogen pressure (see Methods for details). However, during crystallization, a small amount of dodecyl maltoside was again added back to the crystallization mixture as an additive (1/20 of the concentration of decyl maltoside). It was difficult to control the exact concentration of each detergent in such a system, particularly during the detergent exchange step. The idea of having a simple, single detergent in the system seemed attractive, since the exact concentration would be known and it would be much easier to study the effect of the detergent concentration and repeat the conditions. Therefore, experiments were performed using only one detergent, either dodecyl maltoside or decyl maltoside, throughout the protein preparation and crystallization process. However, when dodecyl maltoside was used for the entire process of membrane solublization, protein purification and crystallization, only needle bundles of C*c*O crystals were obtained, while when decyl maltoside was used throughout the entire processes, no crystals were obtained at all. Therefore, it appeared that the two-detergent system was necessary for successful crystallization of *Rs*C*c*O. Decyl maltoside should be the primary detergent during crystallization because of the slightly smaller overall size of the PDCs. However, dodecyl

maltoside is more stabilizing than decyl maltoside for C*c*O as demonstrated by previous experiments (Hilmi, 2002); thus is used during the protein preparation.

The current protocol of using dodecyl maltoside for membrane solublization and decyl maltoside as the major detergent during crystallization was maintained and efforts were then made to search for another secondary detergent in the crystallization additive other than dodecyl maltoside. To do this, a group of secondary detergents, including decyl maltoside and dodecyl maltoside, were used in the crystallization trials at a concentration of approximately 3 x CMC and the diffraction limits of the C*c*O crystals obtained from such conditions were tested at the synchrotron.

Out of the 72 detergents tried as secondary detergents in the crystallization additives, crystals were obtained from 23 of them with varying X-ray diffraction quality. Table 3.4 shows the diffraction limits of C*c*O crystals using various secondary detergents. All of the crystals displayed strong anisotropic X-ray diffraction patterns and only the diffraction limits along the better directions (a^* and b^*) are listed. Some of the best detergents were from the series of cymals, including Cymal-4 and Cymal-5, as well as other maltosides with shorter chains lengths, including nonyl and octyl maltoside. The diffraction limits for C*c*O crystals with these secondary detergents were all similar to or slightly better than when dodecyl maltoside was used as the secondary detergent. When no secondary detergent was used, the diffraction limit observed was worse than when a suitable secondary detergent was used. Therefore, these very few secondary detergents were used for further crystallization trials.

detergent	Diffraction limit*
cymal-4	3.0 Å
cymal-5	3.0 Å
nonyl maltoside	3.0 Å
octyl thiomaltoside	3.1 Å
nonyl thiomaltoside	3.1 Å
deoxy bigCHAP	3.1 Å
$C_{12}E_9$	3.1 Å
dodecyl maltoside	3.1 Å
cymal-6	3.2 Å
nonyl glucoside	3.2 Å
undecyl maltoside	3.2 Å
Zwittergent3-14	3.2 Å
Sucrose monolaurate	3.3 Å
decyl maltoside	3.3 Å
decyl thiomaltoside	3.3 Å
Pluronic F-68	3.3 Å
nonyl thioglucoside	3.4 Å
LDAO	3.5 Å
prodecyl maltoside	3.5 Å
tetradecyl maltoside	3.5 Å
hexadecyl maltoside	3.6 Å
MEGA-9	3.6 Å
CTAB	–

*: diffraction limit of the best crystal along the best direction

Table 3.4: The effects of different secondary detergents on X-ray diffraction resolution limit of the four subunit *Rs*Cc*O* crystals.

3.1.5.5.2 Optimization of Crystallization Procedures and Additives

Since protein crystals generally diffract X-rays much more weakly than those of small molecules, efforts were made to obtain larger protein crystals which could diffract more strongly. Although in many cases protein crystals of larger size do not necessarily have better X-ray diffraction, in the case of *Rs*C*c*O it was indeed true that larger crystals (> 0.3 mm on the side of the triangle) diffracted better than the smaller ones. In an effort to increase the crystal size, the entire drop volume was increased significantly from 4 µl to 20 µl and the sitting-drop setup was used instead of the hanging-drop method. Larger C*c*O crystals that diffracted X-rays better could be obtained by the sitting-drop method that had a bigger drop size.

Metals have been known to promote protein-protein interactions during crystallization (Trakhanov and Quiocho, 1995). In the established crystallization protocol, the divalent cation Mg^{2+} (in the form of $MgCl_2$) was added to the crystallization mixture as a crystallization additive. In an effort to find the optimal metal ions in the crystallization mixture, a number of different chloride salts were used as crystallization additives and the X-ray diffraction was observed at the synchrotron. Out of the approximately 15 different metals tested, C*c*O crystals were successfully obtained with 6 of them, including Mn^{2+}, Cu^{2+}, Co^{2+}, Ca^{2+}, Gd^{2+}, and Sr^{2+}. However, none of these metals were found to lead to any improvements in crystal diffraction.

3.1.5.5.3 Optimization of Flashcooling Procedures and Cryoprotectants

The flashcooling method was also optimized. The concentration of PEG-400

in the cryoprotectant solution was increased to approximately 32%, which seemed to be the minimal concentration required to suppress ice formation. Also modified was the flashcooling procedure. Initially, the crystals were picked up from the original drop solution and soaked in the cryosolution directly for approximately 20 minutes. However, this procedure was found to be rather harsh on C*c*O crystals since many of the crystals displayed visible cracks upon being moved into the cryosolution due to a sudden rise in osmotic pressure. In order to decrease the pressure shock, a gradual, step-wise method for increasing the PEG-400 concentration was used (see Method section for details). The concentration of PEG-400 was increased slowly to 32% within a period of 8 – 10 minutes through several gradual steps. By using the new method, generally no crystal cracks were seen and the diffraction limit and quality of the crystals was improved slightly.

Crystal dehydration prior to flashcooling has been applied successfully to a number of crystals to improve the diffraction limit and decrease the crystals mosaicity including membrane proteins (Kuo *et al.*, 2003). Efforts were also made to try to dehydrate C*c*O crystals before flashcooling by either changing the well solution to a solution with higher PEG-400 concentration, or by soaking the crystals in a stabilizing solution and slowly increasing the concentration of PEG-400 over a period of a few weeks. Unfortunately, dehydration did not lead to any improvement in crystal diffraction, but led to deterioration of C*c*O crystals and a compete loss of X-ray diffraction.

Other efforts to optimize flashcooling of C*c*O crystals included adding small

molecules such as glycerol and/or ethylene glycol to the crystallization mixture to a final concentration of 5% - 10%. Since glycerol and ethylene glycol are cryoprotectants themselves, their presence in the crystallization drop, combined with approximately 22% PEG-400, provided enough cryoprotection to the crystals. Therefore, crystals were simply picked up and flashfrozen in liquid nitrogen without any soaking or handling. Unfortunately, although ice formation was suppressed, the crystals actually diffracted worse than when glycerol or ethylene glycol was not added, presumably due to the disturbing effects of glycerol or ethylene glycol on the crystals. Immiscible oil (Kwong and Liu, 1999) was also tried in flashcooling crystals of *Rs*Cc*O* but led to worse protein X-ray diffraction and extremely strong solvent background in the diffraction image.

3.1.5.6 Design of Site-Directed Mutants to Improve Crystal Diffraction

Site-directed mutagenesis of selected surface residues has been successfully applied to protein crystallography to improve the crystal diffraction in a number of different cases (Pautsch *et al.*, 1999). Figure 3.11 (A) shows the crystal packing in the unit cell of the four subunit *Rs*Cc*O*. There are three crystal contact regions in this crystal form as shown in Figure 3.11 (B). The first crystal contact region was the most extensive one, as described earlier. Besides this major contact region, two more crystal contact regions were also found on the protein surface, which involved fewer residues. Based on the analysis of the crystal structure, a few site-directed mutants of surface residues were designed and generated as listed in Table 3.5. The purpose of these surface mutants is to strengthen the crystal contacts in regions 2 and

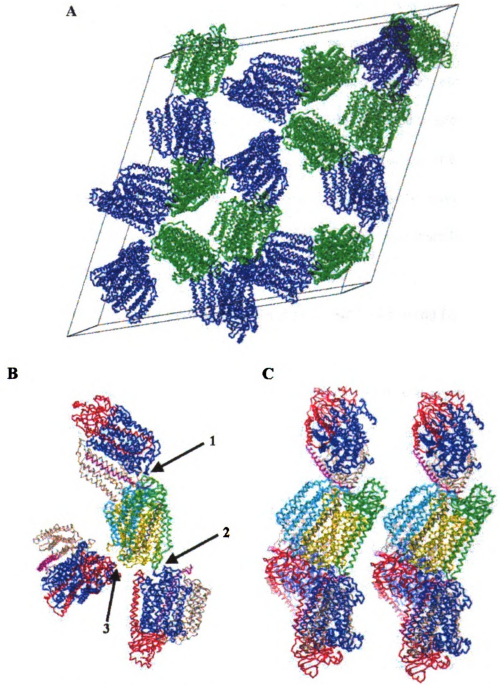

Figure 3.11: Crystal packing of the four subunit *Rs*CcO which belongs to a space group of *R*3. (A): Unit cell display of the *Rs*CcO crystal. There are two *Rs*CcO molecules (shown in blue and green) per asymmetric unit. (B): Detailed crystal contacts around each *Rs*CcO molecule. *Rs*CcO molecules are colored by different polypeptide chains. There are three regions where protein-protein contacts occur as labeled in the figure. (C): No direct protein-protein crystal contact exists along the c^* axis of the unit cell. Molecules of *Rs*CcO are from adjacent unit cells and they are viewed from a different angle approximately 90° away from the view in (B).

3 by favoring protein-protein interactions via side chain atoms. Moreover, since the crystal packing indicated that the crystals of the four subunit C*c*O were two-dimensional in nature, with no direct protein-protein interactions along the *c** axis as shown in Figure 3.11 (C), other mutants were also designed to generate new crystal contacts along the *c** axis, either by promoting ionic interactions or by creating new metal binding sites (See Table 3.5 for details). Unfortunately, some of these mutant proteins did not crystallize, while others did crystallize but did not lead to any improvements in crystal diffraction, as listed in Table 3.5.

3.1.5.7 Screening of New Crystallization Conditions and New Crystal Forms

Extensive screenings to find new crystallization conditions and possibly new crystal forms of C*c*O were also performed with various commercial crystallization screening kits. A few new crystallization conditions from the screening kits were found to produce very small crystals of C*c*O. One of them contained 20% PEG-1000, 200mM NaCl, 100mM Na/K phosphate, pH 6.2; and another screening solution contained 15% ethanol, 100 mM Tris, pH 7.0. However, further optimization of crystallization conditions by varying pH, precipitant and salt concentration failed to produce big enough crystals for X-ray diffraction tests despite repeated trials.

C*c*O crystals were also found growing from a screening solution containing 100 mM HEPES, pH 7.5, 100 mM $(NH_4)_2SO_4$, and 18% PEG-400. The majority of the crystals were thin tetragon plates in shape, which suggested that these crystals might belong to a completely new crystal form. Optimization of crystallization conditions by varying concentrations of precipitants and pH, combined with

R.s. strain	Mutation	Parental strains and plasmid	Objective	Cry-stal	Diffra-ction
196	$V90_{II}D$	Δ123[1], pCH167	Strengthen contact region #2	no	–
197	$V90_{II}D$	Δ123[1], pCH169	Strengthen contact region #2	no	–
200	$E66_{II}D$	Δ123[1], pCH167	Strengthen contact region #3	yes	3.4 Å
202	$E66_{II}D$	Δ123[1], pCH169	Strengthen contact region #3	yes	3.4 Å
207	$W56_{II}E$	Δ123[1], pCH167	Promote new contact along c* axis by promoting ionic interactions	yes	3.2 Å
208	$W56_{II}E$	Δ123[1], pCH169	Promote new contact along c* axis by promoting ionic interactions	yes	3.2 Å
233	$W56_{II}E$ $R229_{III}E$	Δ123[1], pCH167	Promote new contact along c* axis by creating new metal binding site	no	–
234	$W56_{II}E$ $R229_{III}E$	Δ123[1], pCH169	Promote new contact along c* axis by creating new metal binding site	no	–

Reference: (1) Hiser, *et al.* unpublished

Table 3.5: Different site-directed mutants of *Rs*CcO to strengthen crystal contacts and the X-ray diffraction resolution limit of crystals of these mutants.

micro-seeding procedures, yielded single crystals big enough for X-ray diffraction experiments as shown in Figure 3.12.

The new crystals of C*c*O were flashcooled and tested at the synchrotron for X-ray diffraction and a dataset was collected on the best crystal which diffracted to approximately 4.3 Å with very strong anisotropicity. The crystal cell parameters and statistics of data collection are listed in Table 3.6. The crystal belonged to the orthorhombic crystal system with a space group of $P2_12_12_1$. Although the crystal diffraction and the overall completeness of the dataset were rather poor, a molecular replacement was successfully performed using the published four subunit C*c*O structure as the search model and the molecular packing of this new form of crystal was solved as shown in Figure 3.13. It can be seen that, compared with the crystal packing in the regular rhombohedral forms of the four subunit C*c*O crystal, in which crystal contact were found in two dimensions in the a^*b^* plane, the crystal packing of this form of C*c*O crystal, however, seemed more one-dimensional. Crystal contacts occur primarily along the c^* axis involving only a restricted number of residues as shown in Figure 3.13. This poor packing of molecules was the likely reason why this form of C*c*O crystal diffracted poorly and extensive efforts were not made to improve the crystal diffraction of this form of crystal.

3.1.6 Potential Inhibition Sites of Zn^{2+}/Cd^{2+} and the Effects of Cd^{2+} Binding to C*c*O Crystals on X-ray Diffraction

3.1.6.1 Zn^{2+} / Cd^{2+} inhibition on C*c*O Activity

Zn^{2+} has been found to have a strong inhibitory effect on a number of proton

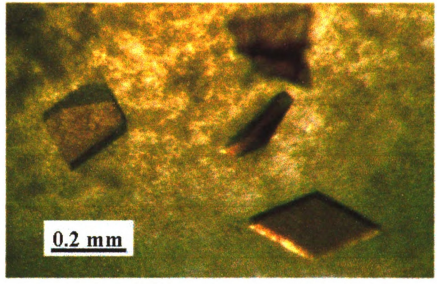

Figure 3.12: Crystals of the four subunit *Rs*Cc*O* which belong to a space group of $P2_12_12_1$.

Crystal Name	167 – tetragon
A. Unit Cell Parameters	
Space Group	$P\,2_1\,2_1\,2_1$
Cell Dimensions (Å)	a=126.3 b=151.8 c=206.6
No. Molecules per A.U.	2
B. Data Collection	
Resolution Range (Å)	20 – 4.3
Completeness (%)	67.2
No. Unique Reflections	18,392
Overall Redundancy	5.8
Overall R_{merge} (%)	7.1

$R_{merge} = \Sigma \mid I_h - \langle I_h \rangle \mid / \Sigma I_h$ over all h, where I_h is the intensity of reflection h. The completeness and number of unique reflections values were obtained from CNS refinement result file after F/sigma cutoff of 3 were applied.

Table 3.6: X-ray data collection and refinement statistics of the four subunit *Rs*C*c*O which belong to a space group of $P2_12_12_1$.

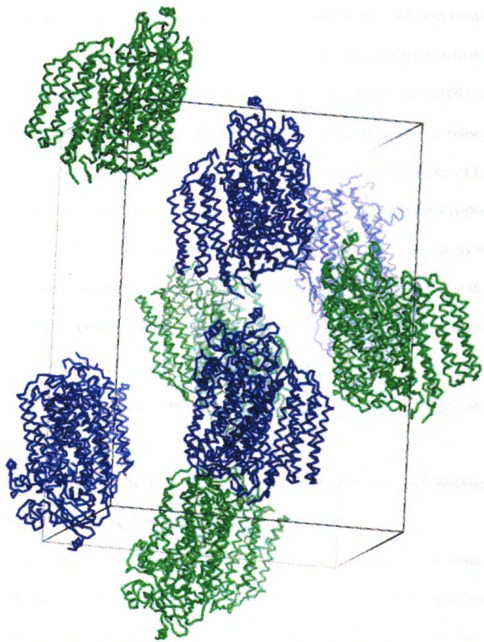

Figure 3.13: Unit cell display of the four subunit orthorhombic *Rs*C*c*O crystal which belongs to a space group of $P2_12_12_1$. There are two *Rs*C*c*O molecules (shown in blue and green) per asymmetric unit.

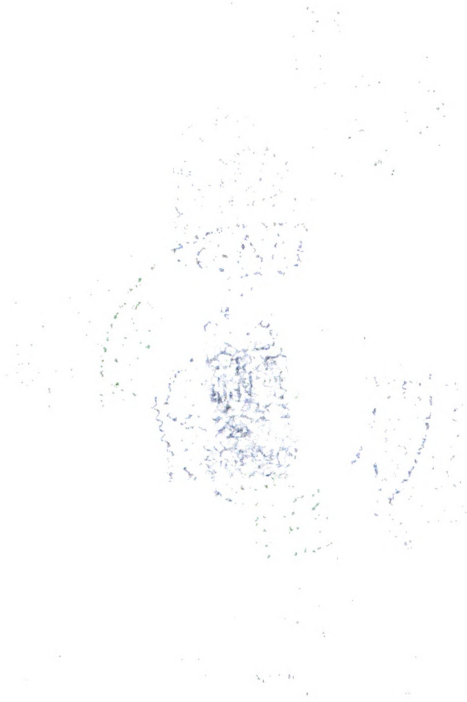

and ion channels by blocking a proton pathway, including cytochrome bc_1 complex (Link and von Jagow, 1995; Berry *et al.*, 2000) and bacterial photosynthetic reaction center (Paddock *et al.*, 1999; Axelrod *et al.*, 2000). Similarly, Zn^{2+} was also found to bind to the outside of *Rs*C*c*O reconstituted into lipid vesicles and inhibit its activity in the presence of a membrane potential with a K_I of ≤ 5 μM (Mills *et al.*, 2002). The inhibition is reversible, pH-dependent, and not competitive with the substrate cytochrome *c* (Mills *et al.*, 2002). The exact inhibition site(s) on the outside of C*c*O was unknown and was proposed to be at or close to the proton exit/backleak pathway (Mills *et al.*, 2002). Additional Zn^{2+} inhibition was observed on free enzyme as well with a much higher inhibition constant and the proposed inhibition site(s) was at the D proton uptake pathway based on the results of single turnover experiments (Aagaard *et al.*, 2002). The exact binding site(s) along D pathway is unknown.

Among all the other metals tested, Cd^{2+} was the only one found to exhibit similar inhibitory effects on C*c*O (Mills *et al.*, 2002).

3.1.6.2 Potential Inhibition Sites of Zn^{2+} / Cd^{2+} and the Effects of Cd^{2+} Binding to C*c*O Crystals on X-ray Diffraction

In order to find out the inhibition site(s) of Zn^{2+}, $ZnSO_4$ was added to crystallization mixture in an effort to obtain crystals of Zn^{2+}-bound CcO. However, it turned out that the presence of Zn^{2+} caused severe precipitation of C*c*O in the crystallization drop even at a very low concentration (approximately 0.5 mM), and no crystals were obtained. Co-crystallization experiments with Cd^{2+} yielded crystals but the X-ray diffraction was extremely poor (worse than 7 Å). Therefore, efforts were

made to soak the crystals of C*c*O formed under normal conditions in a stabilizing solution that contained either Zn^{2+} or Cd^{2+} as described in the Method section. The pH value of the soaking solution was slowly raised to close to 7.0 in order to allow tighter binding of Zn^{2+}/Cd^{2+} to the enzyme, and kept at 7.0 in the cryosolution before flashcooling. Unfortunately, the presence of Zn^{2+} in the soaking solution was found to be extremely damaging to the X-ray diffraction of C*c*O crystals as both the diffraction resolution limit and the completeness of data were much worse than when Zn^{2+} was not added. However, adding Cd^{2+} to the soaking solution appeared beneficial to the diffraction of C*c*O crystals.

Table 3.7 shows the data collection and structural refinement statistics of a C*c*O crystal, obtained from *R. s.* strain 169, which was soaked in stabilizing solution containing 6 mM $CdCl_2$ for 2 hours before flashcooling. It can be seen that, although the diffraction limit of the crystal did not improve (3.2 Å), the quality of the X-ray diffraction improved slightly as judged by the better completeness of the dataset, and the slightly lower overall B factors and very similar final R and R_{free} factors after refinement, despite a smaller F/sigma cutoff.

Figure 3.14 shows the amino acid backbone of the refined structure of *Rs*C*c*O colored by subunits. Superimposed on the structure is the $(F_o\text{-}F_c)$ omit difference electron density map contoured at 3.5 σ. It can be seen that there are electron density peaks (shown in purple) in three locations in the structure as labeled, which could indicate potential binding sites of Cd^{2+} in the crystal structure.

Crystal Name	169 – Cd Soak	169
A. Unit Cell Parameters		
Space Group	*R*3	*R*3
Cell Dimensions (Å)	*a*=*b*=339.5 *c*=89.4	*a*=*b*=339.4 *c*=89.3
No. Molecules per A.U.	2	2
B. Data Collection		
Resolution Range (Å)	30-3.2 (3.31-3.2)	30-2.9 (3.0-2.9)
Completeness (%)	86.7 (69.0)	74.7 (33.4)
No. Unique Reflections	54,839 (4,342)	63,444 (2,841)
Redundancy	8.5 (3.4)	5.1 (3.7)
R_{merge} (%)	10.3 (41.0)	8.2 (30.5)
C. Structural Refinement		
R-factor / R free (%)	26.5 / 31.4	26.7 / 31.5
Average B-factor	96.6	113.5
Non Cryst. Symmetry	restrain	restrain
F / sigma Cutoff	1.01	2.5
R.m.s.d Bond Lengths (Å)	0.009	0.011
R.m.s.d Bond Angles (°)	1.35	1.48
No. of Atoms	17764	17809

$R_{merge} = \Sigma | I_h - \langle I_h \rangle | / \Sigma I_h$ over all *h*, where I_h is the intensity of reflection *h*. R-factor= $\Sigma | |Fo| - |Fc| | / \Sigma |Fo|$; where F*o* and F*c* are the observed and calculated structure factors, respectively. The completeness and number of unique reflections values were obtained from CNS 1.1 refinement result file after F/sigma cutoff was applied. Redundancy and R_{merge} values were obtained from the program Scalepack. Values in parentheses are parameters for the highest resolution shell.

Table 3.7: X-ray data collection and refinement statistics of the four subunit *Rs*C*c*O crystals soaked in a solution containing cadmium. The column on the right is taken from Table 3.1 which shows the data collection and refinement statistics of crystals obtained from the same *R. s.* strain without being soaked in cadmium.

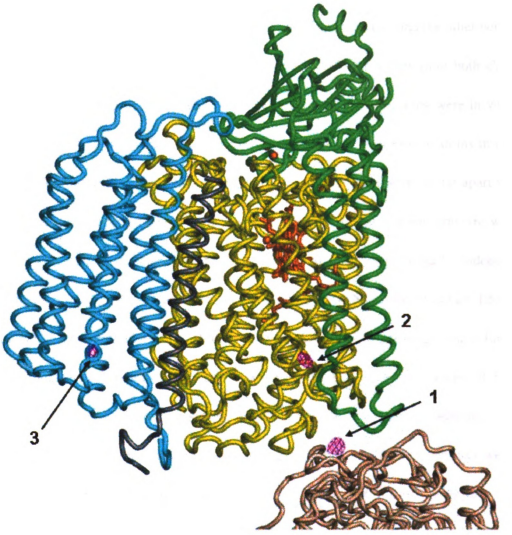

Figure 3.14: Cadmium binding sites found in the structure of the four subunit *Rs*CcO crystals soaked in a solution containing cadmium. *Rs*CcO molecule is colored by subunits (I: yellow; II: green; III: cyan; IV: gray) and the heme groups and coppers are colored orange. Part of another *Rs*CcO molecule is colored wheat. The (F_o-F_c) difference electron density map contoured at 3.5 σ are shown in purple. There are three cadmium binding sites found as labeled in the figure.

Figure 3.15 (A) shows the first potential Cd^{2+} binding site, which was right at the center of a crystal contact region. The cadmium ion was ligated to the side chains of two residues, one of them being $E533_I$ from one *Cc*O molecule, and the other being the same $E533_I$ residue from another molecule. Two $H534_I$ residues from both *Cc*O molecules were also likely to take part in the metal ligation since they were in very close proximity to the cadmium. However, the distances of the nitrogen atoms in the imidazole rings to the cadmium were around 3.3 – 4.5 Å, which were too far apart for this ligation to occur, although there was a possibility that the current structure was not exactly correct in details due to limited resolution, and there could be indeed a tetrahedral ligating coordination about the cadmium involving both residues $E533_I$ and $H534_I$ from both molecules. Both of the two residues had been suggested to form crystal contacts through electrostatic interactions between the side chains of the glutamic acid and histidine residues. However, in the absence of cadmium, the electrostatic interactions were not strong enough and thus the electron densities were not seen for the flexible side chains of residue $E533_I$ from the two molecules, as shown in Figure 3.15 (B). It appeared that the entering of a cadmium ion into this region strengthened this crystal contact by mediating the protein-protein interaction via the ligating interactions between the cadmium ion and the two $E533_I$ residue side chain atoms. Such a strong metal ligating interaction was responsible for the slightly improved crystal diffraction, and this potential cadmium site was probably not the inhibitory site that was observed experimentally.

Figure 3.15 (C) shows the second potential cadmium binding site and its

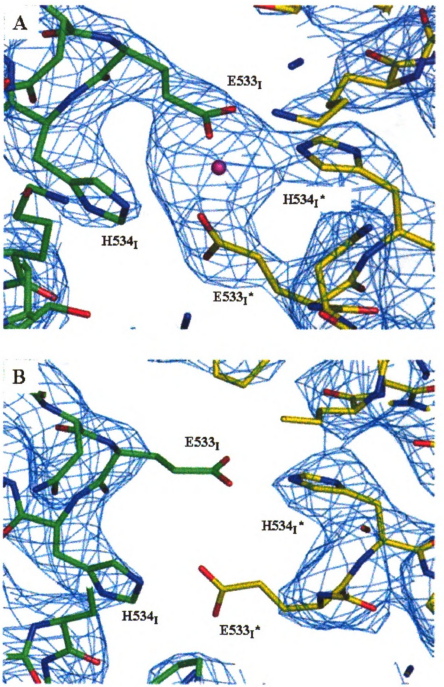

Figure 3.15

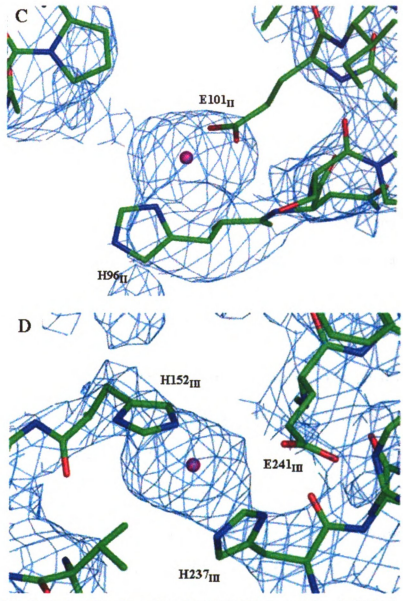

Figure 3.15: Cadmium binding sites found in the four subunit *Rs*C*c*O structure after the crystals were soaked in a solution containing cadmium. (A): The first cadmium binding site located at the intermolecular surface. One *Rs*C*c*O molecule is colored by atom type (C: green, O: red, N: blue) and the other *Rs*C*c*O molecule is colored by a different atom type scheme (C: yellow, O: red, N: blue). Cadmium ion is shown as a purple sphere. The $(2F_o - F_c)$ difference electron density map contoured at 1σ is shown in blue. The ligating residues of the cadmium ion from the two *Rs*C*c*O molecules are labeled as shown in the figure. (B): The same inter-molecular contact region without the bound cadmium, shown in the same color scheme. (C): The second cadmium binding site located close to the interface between subunits I and II, together with the ligating residues as labeled in the figure. (D): The third cadmium binding site buried inside subunit III, together with the ligating residues as labeled in the figure.

neighboring residues together with the ($2F_o$-F_c) difference electron density map contoured at 1 σ. Two nearby amino acid residues from subunit II, $E101_{II}$ and $H96_{II}$, were possible ligating residues to the cadmium ion. However, due to limited resolution and the possible presence of different conformations of the side chains due to partial binding, the side chain electron densities of these two residues were not clearly observed, especially for $E101_{II}$ (Figure 3.15 (C)). $E101_{II}$ has been suggested to be the entrance of the K proton uptake pathway (Branden *et al.*, 2002), and binding of cadmium at the $E101_{II}$ site could lead to the blockage of the K pathway and thus inhibit the enzymatic activity. Therefore, this site could be one of the Zn^{2+}/Cd^{2+} inhibition sites.

There was yet another potential cadmium binding site found inside the subunit III of the enzyme. Figure 3.15(D) shows the third potential binding site and its possible ligating residues, including $H152_{III}$, $H237_{III}$, and $E241_{III}$. This potential cadmium binding site did not seem to be one of the inhibition sites since it was found in subunit III, which is unlikely to be involved in Zn^{2+}/Cd^{2+} inhibition because *Rs*C*c*O without subunit III was still inhibited by Zn^{2+}/Cd^{2+} (Mills *et al.*, 2002).

Unfortunately, potential inhibition sites for Zn^{2+}/Cd^{2+} were not found on the outside of the protein in the crystal structure with crystals soaked with the cadmium solution. One possible reason is that the binding of Zn^{2+}/Cd^{2+} only becomes tight when there is a membrane potential (Mills *et al.*, 2002). Since there is no way to maintain a membrane potential in C*c*O crystals, the binding of Zn^{2+}/Cd^{2+} to the enzyme is likely too weak to be observed in the crystal structure using the above

method.

3.2 X-ray Crystallography of I-II Subunit *Rs*C*c*O

3.2.1 Engineering of an *R. s.* Strain with a single Form of Subunit IV

Upon realization that subunit IV is crucial in forming crystal contacts in the crystallization of the four subunit *Rs*C*c*O, we successfully engineered the long and short form of subunit IV, as described in section 3.1.1 and in Methods section. The assumption made was that the subunit IV expressed from these *R. s.* strains would be uniformly long or short, depending upon which gene sequence was inserted, and that the *Rs*C*c*O complex would contain only one form of subunit IV, either long or short. However, careful analyses on both purified enzyme and re-dissolved crystals with MALDI mass spectrometry clearly show that the gene expression and posttranslational modification lead to more forms of subunit IV in the *Rs*C*c*O complex than the originally engineered forms.

Figure 3.16 shows the MALDI mass spectra of purified *Rs*C*c*O and re-dissolved four subunit *Rs*C*c*O crystals in the subunit IV region. Since both positive and negative ion modes show the protein subunits equally well and the difference in m/z values due to different ionization modes is small, all mass spectra herein are displayed in one color. The conditions including positive and negative ion mode are indicated in figure legends. Figure 3.16 (A) shows the mass spectra of the subunit IV region from purified enzyme and re-dissolved crystals of *Rs*C*c*O obtained from *R. s.* strain 207, which has in its overexpression plasmid the gene for the long form of subunit IV, equivalent to that in *R. s.* strain 167 (see Table 2.1 and Table 3.5). It can be

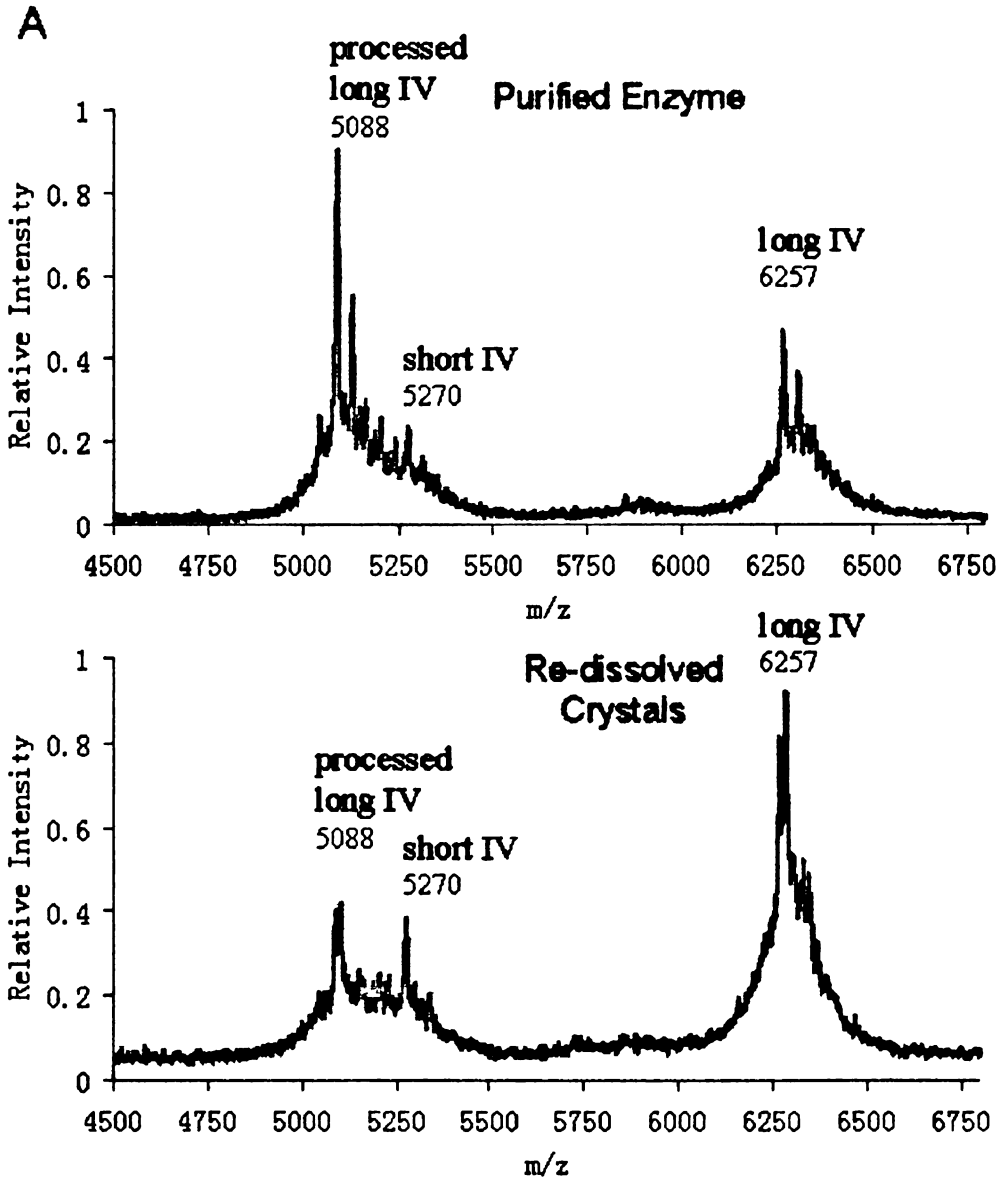
A
processed
long IV
5088
Purified Enzyme
long IV
6257
short IV
5270
Relative Intensity
1
0.8
0.6
0.4
0.2
0
4500
4750
5000
5250
5500
5750
6000
6250
6500
6750
m/z
long IV
6257
Re-dissolved
Crystals
processed
long IV
5088
short IV
5270
Relative Intensity
m/z

Figure 3.16

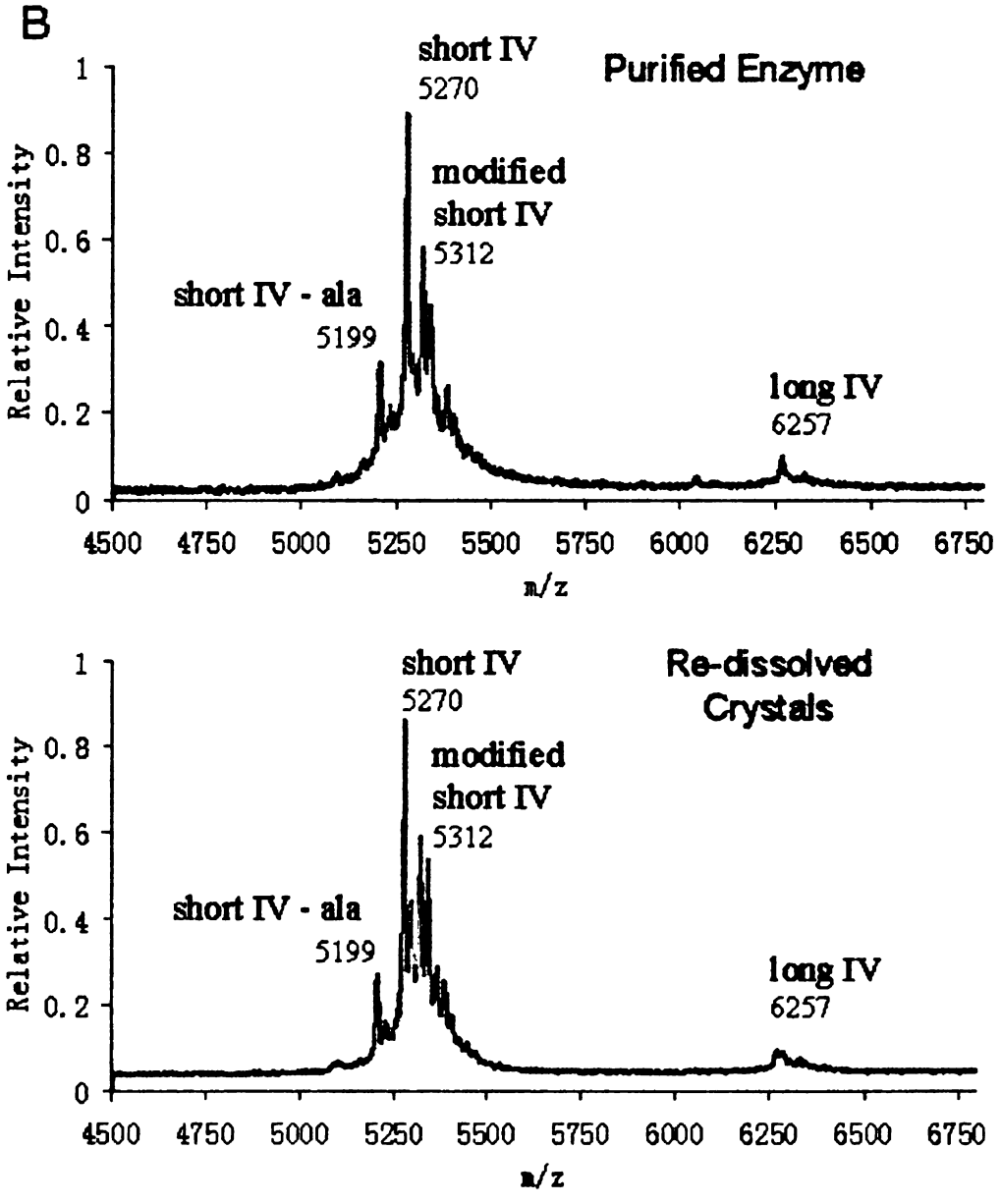
B
short IV
5270
Purified Enzyme
modified
short IV
5312
short IV - ala
5199
long IV
6257
Relative Intensity
1
0.8
0.6
0.4
0.2
0
4500
4750
5000
5250
5500
5750
6000
6250
6500
6750
m/z
short IV
5270
Re-dissolved
Crystals
modified
short IV
5312
short IV - ala
5199
long IV
6257
Relative Intensity
m/z

Figure 3.16

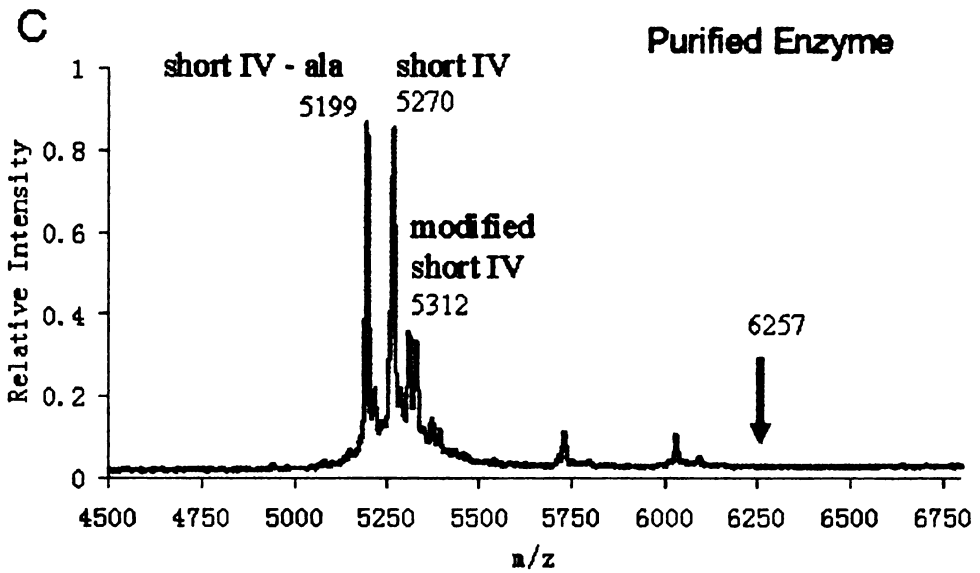

Figure 3.16: MALDI mass spectra of the subunit IV region of purified *Rs*CcO and re-dissolved four subunit *Rs*CcO crystals obtained from different *R. s.* strains. (A): MALDI mass spectra of purified *Rs*CcO (top, negative ion mode) and re-dissolved crystals (bottom, negative ion mode) obtained from *R. s.* strain 207, which overexpresses the long form of subunit IV in its overexpression plasmid. Different forms of subunit IV were observed and they are labeled as shown in the figure with their corresponding m/z values. (See text for detailed descriptions of each of the forms of subunit IV.) (B): MALDI mass spectra of purified *Rs*CcO (top, negative ion mode) and re-dissolved crystals (bottom, positive ion mode) obtained from *R. s.* strain 169, which overexpresses the short form of subunit IV in its overexpression plasmid. Different forms of subunit IV were observed and they are labeled as shown in the figure with their corresponding m/z values. (See text for detailed descriptions of each of the forms of subunit IV.) (C): MALDI mass spectra of purified *Rs*CcO obtained from *R. s.* strain 169Δ4 (positive ion mode), which has the native subunit IV DNA sequence deleted from its genome and has the short form of subunit IV in its overexpression plasmid. Different forms of subunit IV were observed and they are labeled as shown in the figure with their corresponding m/z values. (See text for detailed descriptions of each of the forms of subunit IV.)

seen that there are several major m/z peaks in the spectra for both the purified enzyme and re-dissolved crystals, which represents the long form of subunit IV (m/z = 6257), the short form of subunit IV (m/z = 5270), and a third form with m/z = 5088. (Additional peaks represents salt adducts of peptides). The third form with m/z = 5088 is the proteolytic cleaved long form of subunit IV (see later for reasoning), which corresponds to the short form of subunit IV without either the N-terminal alanine and aspartic acid or the C-terminal asparagine and alanine (see Figure 2.1 for complete amino acid sequence of subunit IV). Current evidence favors the first possibility since the electron density for the C-terminal two amino acid residues of subunit IV, $N50_{IV}$ and $A51_{IV}$, is always clearly visible in the crystal structure. This suggests their stable presence in stoichiometric amounts. On the other hand, no such evidence exists for the first two residues in the subunit IV, $A2_{IV}$ and $D3_{IV}$, since the entire N-terminal 9 residues are missing in the crystal structure. By comparing the peak heights in the spectra, it can also be seen from Figure 3.16 (A) that *Rs*C*c*O complex with the long form of subunit IV is selected more favorably during nucleation and/or crystal growth process, since the relative abundance of the long form of subunit IV is much higher in the crystal than it is in the purified enzyme. However, coexistence of different subunits IV would be expected to negatively affect the X-ray diffraction quality of the four subunit *Rs*C*c*O crystals; in fact, as observed in Part I, crystals obtained from *R. s.* strains overexpressing long subunit IV generally diffracted X-rays a bit worse than those obtained from strains overexpressing short subunit IV.

Figure 3.16 (B) shows the mass spectra of the subunit IV region from purified

enzyme and re-dissolved crystals of *Rs*CcO from *R. s.* strain 169, which has in its overexpression plasmid the gene for the short form of subunit IV (see Table 2.1). It can be seen from these spectra that, although there is no long subunit IV gene in the overexpression plasmid, there is a very small amount of long form of subunit IV in both the purified enzyme and re-dissolved crystals. This small amount of the long subunit IV is the expression product from the *R. s.* genome. Moreover, compared with the spectra in Figure 3.16 (A), there is no third form of subunit IV found in the Figure 3.16 (B), which strongly suggests that this form of subunit IV with m/z = 5088 is the proteolytic cleavage product of the long subunit IV. Interestingly, two extra peaks close to the peak representing short subunit IV with m/z = 5312 and m/z = 5199 are observed. The m/z value of the first extra peak is 42 units higher than that of the short subunit IV, which could indicate a chemical modification of the short subunit IV, such as acetylation. However, the exact nature and position of such a chemical modification is unclear. The m/z value of the second peak is 71 units lower than that of the short subunit IV, which could be caused by a proteolytic cleavage of a single alanine residue from either the N-terminus or the C-terminus of the short subunit IV. (Again, likely the unresolved N-terminus.)

Although *Rs*CcO obtained from strain 169 is more homogeneous in terms of subunit IV than that from strain 207, there is still a small amount of contamination of the long subunit IV present, which could negatively affect the homogeneity of protein product and crystal quality. In an effort to produce the ultimately homogeneous form of subunit IV, a new *R. s.* strain, 169Δ4, was made by conjugating the overexpression

plasmid having the short subunit IV into a new parental *R. s.* strain, ΔIΔIV, which had subunit I and subunit IV deleted from its genome (see Table 2.1). Figure 3.16 (C) shows the MALDI mass spectra of the subunit IV region from purified enzyme from *R. s.* strain 169Δ4. It can be seen that there is no long subunit IV with m/z=6257 in the enzyme complex, as expected. The assumed acetylated form of short subunit IV and the short subunit IV less an alanine are still present and interestingly, the relative amount of the proteolyzed short subunit IV becomes even greater as judged from the peak heights. There is evidence that additional peaks at m/z=5731 and m/z=6031 may be lipid complexes of the short subunit IV (Distler *et al.*, 2004). Although more than one form of subunit IV is present, the protein product from *R. s.* strain 169 is the closest to being completely homogeneous in that there are only very small variations among the different forms compared with the long and short forms of subunit IV. Unfortunately, crystals of the four subunit *Rs*C*c*O obtained from strain 169Δ4 showed slightly worse X-ray diffraction (3.3 Å) compared with those obtained from strains 167 or 169.

3.2.2 Crystallization of I-II Subunit *Rs*C*c*O and Diffraction Quality of I-II Subunit *Rs*C*c*O Crystals

*Rs*C*c*O obtained from strain 169Δ4 did not lead to crystals of the four subunit enzyme with improved X-ray diffraction, but instead a completely new and unexpected form of the crystals was produced after several weeks (see Method section). These crystals contained only the catalytic subunits I and II of *Rs*C*c*O, the enzyme was purified by using the imidazole step gradient method, with a small

amount of cadmium (1.3 mM) added into the crystallization mixture (see Methods section for details of the conditions). Figure 3.17 shows a picture of the I-II subunit *Rs*C*c*O crystals. It can be seen in the figure that there are two different crystal forms present in the crystallization drop. The background of tiny crystals are those of the four subunit *Rs*C*c*O and the bigger football-shaped ones are crystals with only the two catalytic subunits of *Rs*C*c*O.

A new *R. s.* strain named 37Δ4 was also made by conjugating a new overexpression plasmid which contained no subunit IV sequence into the parental strain ΔIΔIV (see Table 2.1). *Rs*C*c*O obtained from strain 37Δ4 contained no subunit IV at all. When the enzyme was used as a crystallization candidate, under similar crystallization conditions, crystals of the four subunit enzyme were not formed. However, crystals of the I-II subunit *Rs*C*c*O could be obtained with similar X-ray diffraction quality (approximately 2.4 – 2.5 Å resolution) although many of them appeared twinned.

Due to the lack of strong crystal contacts along the direction parallel to the native membrane, membrane protein crystals often display anisotropic diffraction behavior which leads to difficulties in data processing and subsequent structural refinement. The crystal of the four subunit *Rs*C*c*O diffracts X-rays anisotropically and the structure was solved to a resolution of 2.3Å along a^* and b^* and 2.8Å along c^* (Svensson-Ek *et al.*, 2002). On the other hand, the I-II subunit crystals displayed isotropic X-ray diffraction to 2.35 Å resolution. Table 3.8 shows the data collection and structural refinement statistics of the best crystal obtained from *R. s.* strain 169Δ4.

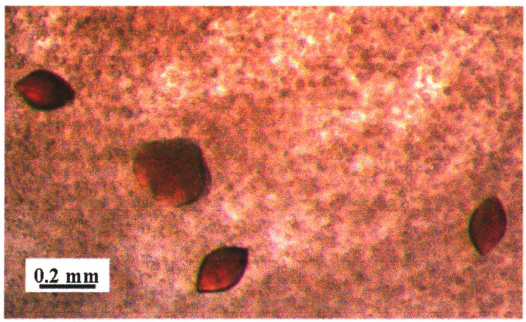

Figure 3.17: Crystals of the I-II subunit *Rs*CcO which belong to a space group of $P2_12_12_1$. Tiny particles are crystal showers of the four subunit *Rs*CcO immersed in a heavy protein precipitation.

Crystal Name	169Δ4, I-II subunit Crystal
A. Unit Cell Parameters	
Space Group	$P2_12_12_1$
Cell Dimensions (Å)	a=125.0 b=131.3 c=176.1
No. Molecules per A.U.	2
B. Data Collection	
Resolution Range (Å)	30 – 2.35 (2.43 – 2.35)
Completeness (%)	99.9 (99.9)
No. Unique Reflections	112,854 (12,046)
Overall Redundancy	8.5 (6.4)
Overall R_{merge} (%)	7.0 (63.5)
C. Structural Refinement	
R-factor / R free (%)	19.4 / 21.4 (24.5 / 27.5)
Average B-factor	34.0
Non Cryst. Symmetry	-
F / sigma Cutoff	-
R.m.s.d Bond Lengths (Å)	0.010
R.m.s.d Bond Angles (°)	1.16
No. of Atoms	13141

$R_{merge} = \Sigma | I_h - \langle I_h \rangle | / \Sigma I_h$ over all h, where I_h is the intensity of reflection h. R-factor= $\Sigma | |Fo| - |Fc| | / \Sigma |Fo|$; where Fo and Fc are the observed and calculated structure factors, respectively. Values in parentheses are parameters for the highest resolution shell.

Table 3.8: X-ray data collection and refinement statistics of the I-II subunit *Rs*CcO crystals.

It can be seen that compared with previous four subunit *Rs*CcO crystals, refinement of the I-II subunit crystals led to much improved R and R_{free} factors and lower B factors. Compared with the four subunit *Rs*CcO crystals, which were grown at 4°C and would quickly dissolve upon a rise in temperature, the I-II subunit *Rs*CcO crystals were also grown at 4°C but remained stable at room temperature, which could suggest tighter packing of molecules in this form. Besides using cadmium as the additive, crystallization experiments were also performed with other divalent cations such as mercury, nickel, manganese, and strontium. However, no I-II subunit *Rs*CcO crystals were obtained under similar conditions.

3.2.3 Biochemical Analysis of I-II Subunit *Rs*CcO Crystals

3.2.3.1 UV-visible Spectra and Activity Assays of Re-dissolved I-II Subunit *Rs*CcO Crystals

Several crystals of I-II subunit *Rs*CcO were removed from the crystallization drop and dissolved in buffer for biochemical analysis. Figure 3.18 shows the comparison of UV-visible absorption spectra of oxidized (blue) and reduced (purple) spectra of purified four subunit enzyme and re-dissolved I-II subunit crystals. The re-dissolved crystals show normal heme peaks at 445 nm and 606 nm in the reduced form compared with the purified four subunit enzyme, but the ratio of A_{280} / A_{421} is much lower (1.35 in Figure 3.18 (B) vs. 2.3 in Figure 3.18 (A)). The decreased A_{280} in the crystals compared with the whole enzyme indicates that a significant portion of enzyme molecules have shed subunits III and IV in the process of forming crystals.

The enzymatic activity of re-dissolved I-II subunit *Rs*CcO crystals was

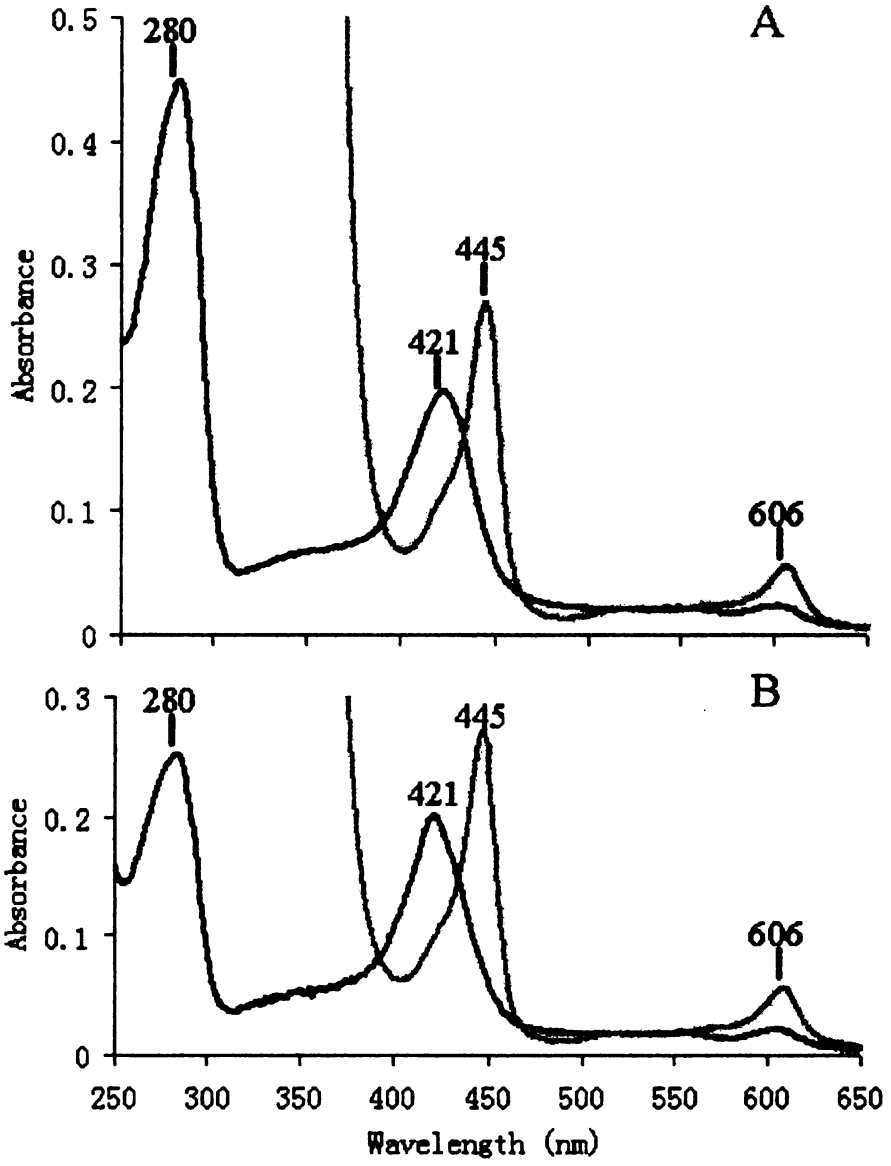

Figure 3.18: UV-visible spectra of purified *Rs*CcO (A, top panel) and re-dissolved I-II subunit *Rs*CcO crystals (B, bottom panel). The spectra of the oxidized CcO are shown in blue, and dithionite-reduced CcO spectra are shown in purple. Normal heme peaks are observed in the re-dissolved crystals as compared with those in the purified enzyme as labeled in the figures. However, the A_{280} / A_{421} ratio is much lower in the re-dissolved crystals than in the purified enzyme.

measured under steady state conditions using an oxygen electrode; the reaction traces showing the rates of oxygen consumption are shown in Figure 3.19. The initial oxygen consumption rates are listed in the inset of the figure. Note the activity decreases as the enzyme turns over, a phenomenon not seen with the wild type *Rs*C*c*O but typical of subunit III-less C*c*O (Bratton *et al.*, 1999; Hosler, 2004). Adding lipid and arachidonic acid protects the enzyme from undergoing suicide inactivation, as shown in the blue and red traces in the figure (Mills and Hosler, 2005). The initial rates measured are similar to those reported for purified subunit III-less enzyme (Mills and Hosler, 2005). It should be noted that these crystals had been maintained under crystallization conditions for approximately 3 months before being dissolved and assayed. The high activity observed strongly supports previous observations that the I-II oxidase is highly stable unless it is undergoing turnover. It was recently found that subunit III-less *Rs*C*c*O obtained by treatment of the four subunit enzyme with Triton X-100 actually retained subunit IV in the enzyme complex (Hosler, personal communication). Therefore, it would be useful to compare the results of structural and functional analyses between I-II-IV subunit *Rs*C*c*O and the re-dissolved I-II subunit crystals for better understanding of subunit IV, whose role is unknown to date.

3.2.3.2 MALDI Mass Spectrometry Analysis of Lipids

MALDI mass spectrometry was again used to analyze the bound lipids in both purified enzyme and in re-dissolved I-II subunit crystals. Figure 3.20 shows the comparison of lipid species present in purified enzyme obtained from *R. s.* strain 169Δ4 and in re-dissolved I-II subunit crystals. It can be seen that in the purified

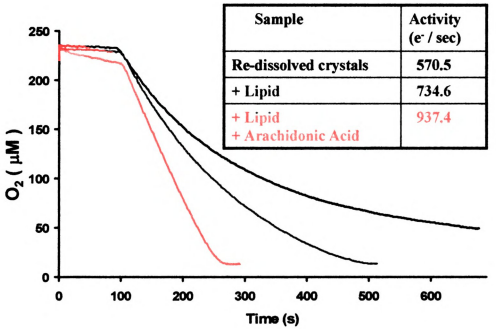

Figure 3.19: Enzymatic activity measurement of re-dissolved I-II subunit *Rs*CcO crystals under steady state conditions using an oxygen electrode. The reaction traces represent the oxygen consumption for re-dissolved crystals (black), re-dissolved crystals with asolectin added to the reaction mixture (blue), and re-dissolved crystals with asolectin and arachidonic acid added to the reaction mixture (red). The initial oxidase activity value under each condition is listed in the inset of the figure.

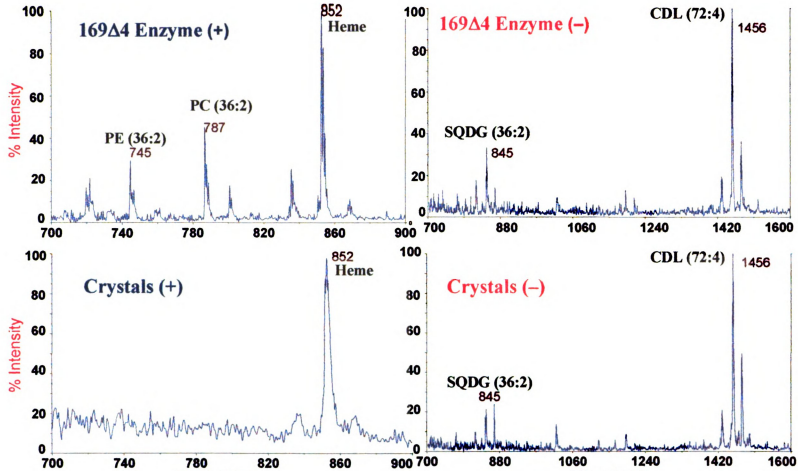

Figure 3.20: MALDI mass spectra of the lipid regions of purified *Rs*CcO and re-dissolved I-II subunit *Rs*CcO crystals in both positive and negative ion mode comparing the lipid species present in purified *Rs*CcO and in re-dissolved I-II subunit crystals.

enzyme sample, two phospholipids, PE and PC, were identified using the positive ion mode and CDL and SQDG were identified using the negative ion mode. Interestingly, in the re-dissolved I-II subunit crystals, no PE or PC was detected using the positive ion mode, while CDL and SQDG were identified in the spectra using negative ion mode. The above observation could be due to the fact that PE and PC are bound to the interfaces of subunits III and IV, and they were stripped off the enzyme complex along with subunits III and IV. This emphasizes the likely importance of the lipid in the structure of these two subunits.

3.2.4 Crystal Structure of the I-II Subunit *Rs*C*c*O

3.2.4.1 Overall Structure of I-II Subunit *Rs*C*c*O

The overall structure of the two subunit *Rs*C*c*O is almost identical to the structure of the subunits I and II in the four subunit structure, with an RMSD of approximately 0.5 Å over all the Cα atoms, as revealed by DALI homology search (Holm and Sander, 1993) (Figure 3.21). Such a strong similarity was also observed in the four subunit and I-II subunit structures of *Pd*C*c*O (Ostermeier *et al.*, 1997). This is reassuring since the results and conclusions drawn from the two subunit crystal structure can then be applied to understanding the four-subunit enzyme with reasonable confidence. The two iron heme molecules, copper centers, and non-redox active metal centers including Mg^{2+} and Ca^{2+} found in the four subunit structures are also found in the two subunit structure, with their ligating residues. Unlike the case of the four subunit crystal structure, the two molecules in the asymmetric unit of the two-subunit crystal are different from each other with respect to the arrangement of

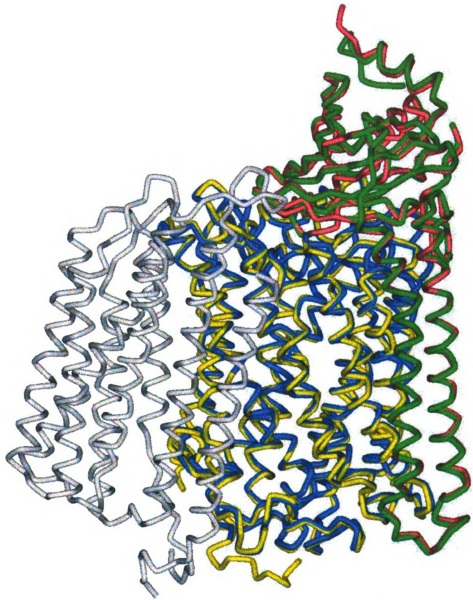

Figure 3.21: Comparison of the structure of the I-II subunit *Rs*CcO and the four subunit *Rs*CcO (PDB entry 1M56). The main chain peptide of subunits I and II from the I-II subunit crystal structure are shown in blue and red, respectively, while those from the four subunit structure are shown in yellow and green, respectively. Subunits III and IV from the four subunit *Rs*CcO structure are shown in gray. Note that the structure of subunits I and II from the two crystal structures are almost identical.

some water molecules and other bound molecules around and within them. Thus we have two independent I-II subunit *Rs*C*c*O crystal structures and the differences between the two molecules are likely due to different crystallographic environments.

3.2.4.2 Crystal Packing of I-II Subunit *Rs*C*c*O

Figure 3.22 shows the crystal packing of a unit cell of I-II subunit *Rs*C*c*O. It can be seen that, compared with the crystal packing in the four subunit *Rs*C*c*O, which occurs primarily within the a^*b^* plane (Figure 3.11), crystal packing of this form of *Rs*C*c*O crystal is 3-dimensional. Therefore, there was no anisotropic diffraction commonly observed with membrane proteins. As shown in Figure 3.22 and Figure 3.23, analysis of the crystal contacts reveals a new contact region involving the subunit II extramembrane domains, mediated by two cadmium ions as well as the two engineered histidine tags. As shown in Figure 3.23 (A), each cadmium ion is ligated in a tetrahedral coordination geometry by the side chains of three amino acid residues, including two histidines, $H283_{II}$ and $H285_{II}$, and one glutamic acid, $E280_{II}$, from one protein molecule and one other glutamic acid residue, $E152_{II}$*, from another protein molecule. Interestingly, the two participating histidine residues, $H283_{II}$ and $H285_{II}$, are from the engineered histidine tag. Another contact exactly like this exists close by, involving the same residues from the opposite protein molecule. The two crystal contacts display a quasi two-fold rotational symmetry as shown in Figure 3.23 (B). Such strong crystal contact mediated by cadmium ions is likely responsible for the superior X-ray diffraction compared with the 4 subunit protein crystals. This novel crystal contact involving an engineered histidine tag and a cadmium ion has rarely

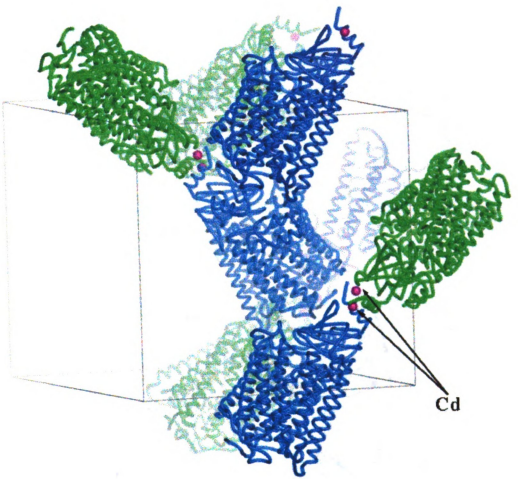

Figure 3.22: Unit cell display of I-II subunit *Rs*CcO. The crystal belongs to a space group of $P2_12_12_1$. There are two *Rs*CcO molecules per asymmetric unit and they are colored blue and green. Two cadmium ions (purple) were found at the molecular interface mediating key crystal contact.

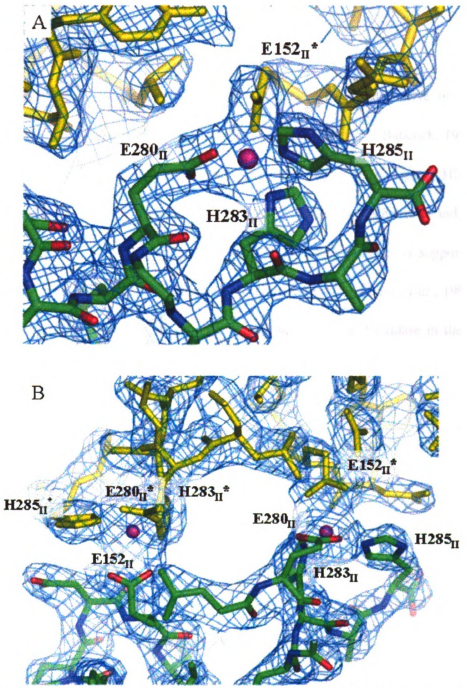

Figure 3.23: Major crystal contact region of I-II subunit *Rs*CcO contributed by the engineered histidine tag at the shortened C-terminus of subunit II and the cadmium ion. One molecule is colored by atom type (C: green, O: red, N: blue), while the other molecule is colored yellow. The ($2F_o - F_c$) electron density map contoured at 1.0 σ is shown in blue. (A): The participating amino acid residues from the two protein molecules form a tetrahedral coordination around the cadmium ion (purple) as labeled in the figure. (B): There are two identical crystal contact interactions at this interface with a quasi-two-fold rotational symmetry axis at the center.

been seen (see Discussion).

3.2.4.3 The Binuclear Center

The binuclear center consisting of heme a_3 and Cu_B is the active site of the enzyme where oxygen is reduced to water (Ferguson-Miller and Babcock, 1996). A covalent linkage between the $C\varepsilon_2$ of $Y288_I$ and the $N\varepsilon_2$ of a Cu_B ligand, $H284_I$, is observed in the crystal structures of C*c*O from bovine mitochondria and *P. d.* (Ostermeier *et al.*, 1997; Yoshikawa *et al.*, 1998), and its presence is supported by mass spectrometry analysis of C*c*O from a variety of sources (Buse *et al.*, 1999), as well as by FTIR studies on the *E. Coli* cytochrome bo_3 quinol oxidase in the same family of heme-copper oxidases (Tomson *et al.*, 2002). Such a covalent linkage was not observed unequivocally in the wild type four subunit *Rs*C*c*O crystal structure. It was suggested that there was a mixture of covalently linked and non-covalently linked species in the crystal (Svensson-Ek *et al.*, 2002). In the current structure, however, a covalent linkage is clearly observed. Figure 3.24 shows the simulated annealing omit map contoured at 5.5 σ. In this figure, clear electron density is observed between the $N\varepsilon_2$ of $H284_I$ and the $C\varepsilon_2$ of $Y288_I$. Model building of this linkage did not lead to significant distortion of the bond geometry and planarity of the two involving residues. This observation further supports the presence of this covalent linkage and its likely importance in chemical catalysis. Such a covalent linkage is believed to lower the pKa of the tyrosine OH group and facilitate free radical formation of $Y288_I$. The tyrosine free radical is postulated to form during turnover, allowing the 2-electron

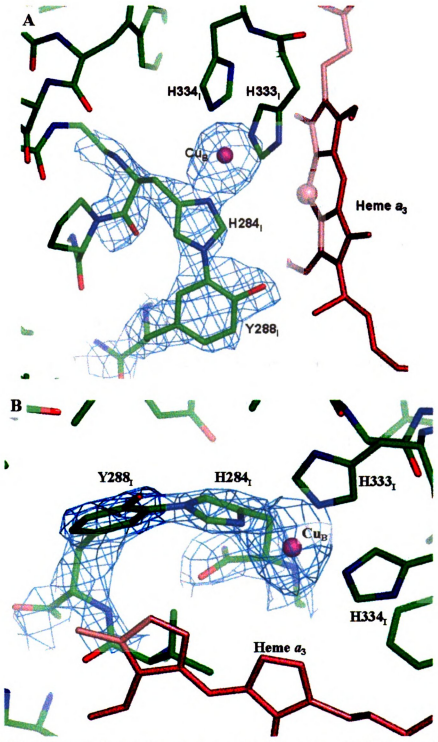

Figure 3.24: The covalent linkage between the ring atoms of $Y288_I$ and $H284_I$ of *Rs*CcO. The ($F_o - F_c$) difference simulated annealing omit map contoured at 5.5 σ is shown in blue. The amino acid residues are colored by atom type (C: green; O: red; N: blue), the heme a_3 and its Fe atom are colored light red, and the Cu_B atom is colored purple. (A) and (B) are from two different views.

reduced enzyme [Fea_3^{2+} - Cu_B^{1+}] to carry out a 4-electron reduction of oxygen, and avoid the production of a peroxy intermediate (Proshlyakov *et al.*, 1998).

Between the Fe in the heme a_3 and the Cu_B center, there is residual density in the (F_o-F_c) map. Previously observed density in this region has been interpreted as a water molecule ligated to Fea_3 and a hydroxide ion to Cu_B (Ostermeier *et al.*, 1997) or a peroxy-bridge the binuclear center (Yoshikawa *et al.*, 1998). However, the fact that four electrons are required to fully reduce the active site contradicts the presence of such a peroxy form (Steffens *et al.*, 1993). Efforts to fit two separate ligands between Fea_3 and Cu_B also turned out to be difficult leading to the two ligands being too close (1.5 Å) to each other. According to a recently proposed proton pumping mechanism (Sharpe *et al.*, 2005), there is likely to be a fixed hydroxide on the copper and a less well defined water between the heme iron and Cu_B center in the oxidized enzyme. Such a dynamic feature is likely why it was hard to build in models in this region.

3.2.4.4 Proton Uptake Pathways

There are two established proton pathways in the enzyme: the D and K pathways, named after the residues $D132_I$ and $K362_I$, respectively, whose mutational replacement blocks each path, respectively (Ostermeier *et al.*, 1995; Svensson-Ek *et al.*, 2002). In the four subunit *Rs*C*c*O crystal structure, a clear chain of 10 water molecules was resolved in the D pathway from $D132_I$ leading to the vicinity of $E286_I$, a residue thought to be critical in conducting protons from the D path to the active site and the external bulk phase (Hofacker and Schulten, 1998). Such a chain of waters is not as clearly resolved in the current structure. Figure 3.25 shows the comparison of

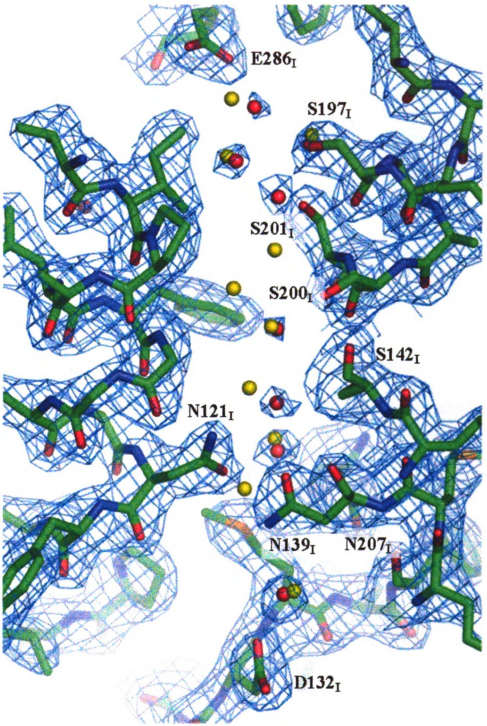

Figure 3.25: Comparison of the resolved waters in D proton uptake pathway in the crystal structures of I-II subunit *Rs*CcO and the four subunit *Rs*CcO (PDB entry 1M56). Amino acid residues from the I-II subunit *Rs*CcO structure are colored by atom type (C: green; O: red; N: blue). Waters resolved in the D pathway from the I-II subunit *Rs*CcO are shown in red and those from the four subunit enzyme in yellow. The ($2F_o - F_c$) difference electron density map contoured at 1 σ is shown in blue.

the resolved D channel waters in the I-II subunit and four subunit *Rs*CcO structures colored in red and yellow, respectively. The conformations of the amino acid residues along the pathway are very similar between the two structures and only the residues from the current I-II subunit *Rs*CcO structure are shown. It can be seen that there are 3 fewer resolved waters near the important residues along the pathway; the former are shown in red, and they are hydrogen bonded to $D132_I$, $N121_I$, $N139_I$, $S200_I$, $S201_I$, $S197_I$, and $E286_I$. Although plausible, it is not likely that the fewer number of resolved water molecules are due to insufficient X-ray diffraction resolution since this structure has better resolution in 3 dimensions than the previous one. Interestingly, the *Pd*CcO I-II subunit structure was also lacking in resolved waters in the D channel (Ostermeier *et al.*, 1997). Subunit III, although not directly involved in either electron transfer or proton pumping, appears to play a role in the kinetics of the D channel (Hosler, 2004). Its close proximity to the D pathway, mediated via the phospholipid molecules, may account for this effect. A less well-defined arrangement of water in the D pathway could contribute to a less effective proton transfer.

Compared with the D pathway, the K pathway has very few waters resolved in the four subunit *Rs*CcO structure, although molecular dynamics studies suggest that there are many more in the pathway (Cukier, 2005; Seibold *et al.*, 2005). The I-II subunit *Rs*CcO crystal structure shows a similar water arrangement to the four subunit *Rs*CcO structure, as shown in Figure 3.26.

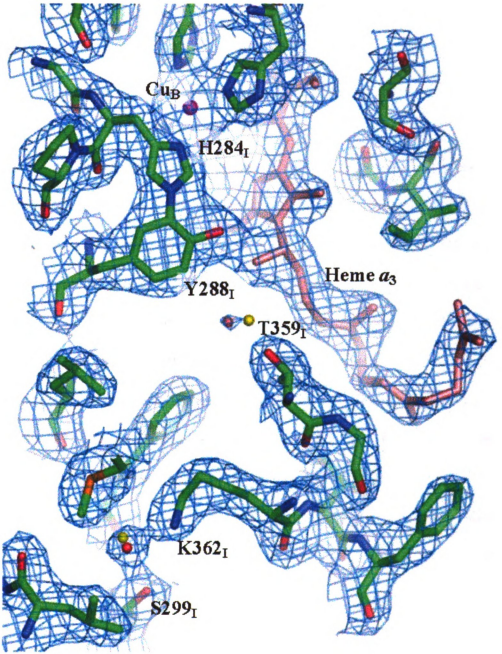

Figure 3.26: Comparison of the resolved waters in K proton uptake pathway in the crystal structures of I-II subunit *Rs*C*c*O and the four subunit *Rs*C*c*O (PDB entry 1M56). Amino acid residues from the I-II subunit *Rs*C*c*O structure are colored by atom type (C: green; O: red; N: blue). Heme a_3 is shown in light red. Waters resolved in the K pathway from the I-II subunit *Rs*C*c*O are shown in red and those from the four subunit enzyme in yellow. The $(2F_o - F_c)$ difference electron density map contoured at 1 σ is shown in blue.

3.2.4.5 Additional Cadmium Binding Site

Besides the cadmium binding site found at the protein-protein interface as shown in Figure 3.22, an additional cadmium binding site was identified which was ligated to side chain atoms of $E101_{II}$ and $H96_{II}$, as shown in Figure 3.27. It can be seen from this figure that the conformations of the two ligating residues (colored by atom type) changed significantly from the unliganded state (yellow) (published four subunit *Rs*C*c*O structure, PDB entry 1M56) upon binding of the cadmium ion at this site. This cadmium binding site was also observed in the structure of the four subunit *Rs*C*c*O when the crystal was soaked in a $CdCl_2$ solution before flashcooling (see 3.1.6.2). $E101_{II}$ has been suggested to be the proton entry point for the K proton uptake pathway in *Rs*C*c*O (Branden *et al.*, 2002; Tomson *et al.*, 2003). It was also found previously that Zn^{2+}/Cd^{2+} inhibits the C*c*O activity both in reconstituted lipid vesicles and under steady state turnovers (Mills *et al.*, 2002). Therefore, it is likely that this cadmium binding site could be the inhibition site on the inside of the membrane responsible for the lower activity under steady state turnovers. Binding of Zn^{2+}/Cd^{2+} at this site may lead to inhibition of the enzymatic activity by blocking the K pathway, which would contradict a previous conclusion that the Zn^{2+}/Cd^{2+} inhibition site(s) on the inside of the membrane is at the D pathway (Aagaard *et al.*, 2002). Site-directed mutants which eliminate the binding of cadmium at this site are currently being generated and their effects on Zn^{2+}/Cd^{2+} inhibition will be studied.

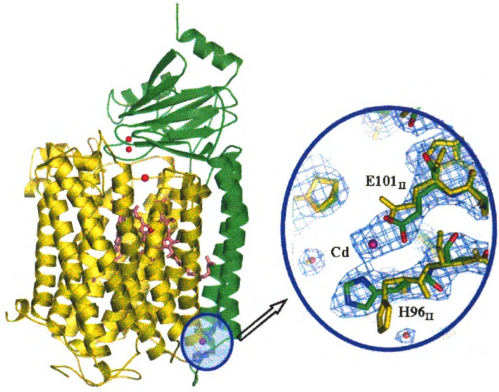

Figure 3.27: Additional cadmium binding site in the structure of I-II subunit *Rs*CcO. The additional cadmium binding site is located on the inside of the membrane close to the subunit I (yellow) and II (green) interface, as shown in the left panel. The ($2F_o - F_c$) difference electron density map contoured at 1.0 σ (blue) is shown in the right panel. In the current structure (colored by atom type), cadmium (purple) is bound to $E101_{II}$ and $H96_{II}$ of subunit II. Binding of cadmium alters the conformations of the ligating residues compared to that found in the unliganded four subunit *Rs*CcO crystal structure (yellow) (PDB entry 1M56).

3.2.4.6 Detergents and Lipids

A number of alkyl chains and detergent head groups were also resolved in the current structure. There are 3 complete detergent molecules resolved, two of them decyl maltoside based on the length of the resolved alkyl chain, and the third dodecyl maltoside. Both detergents were present in the crystallization mixture. Figure 3.28 shows the two decyl maltoside molecules which reside at the interface of two protein molecules. Interestingly, the positions of the two detergent molecules suggest that they may be involved in mediating contacts: their hydrophobic tails interact with the transmembrane region of one molecule and their polar head groups interact with the extramembrane soluble domain of another molecule.

Membrane lipids play important roles in transmembrane proteins. They not only provide a hydrophobic matrix and diffusion barrier, but also contribute to functional aspects of membrane proteins, a subject of ongoing investigation. In the crystal structure of the four subunit *Rs*C*c*O, a total of 6 phosphatidyl ethanolamines were identified. Four of them were found surrounding subunit IV, virtually isolating it from protein contacts, and the two others were found in the crevice within subunit III and associated with subunit I (Svensson-Ek *et al.*, 2002). In fact, subunit IV lacks direct contact with its neighboring subunits I and III, and its interaction appears to be mediated via the membrane lipid molecules (Svensson-Ek *et al.*, 2002). Somewhat surprisingly, in the current structure, we did not find any lipid molecules that correspond to any of the six lipid molecules found in the four subunit structure, despite our efforts to retain lipids by using less detergent, combined with fewer steps

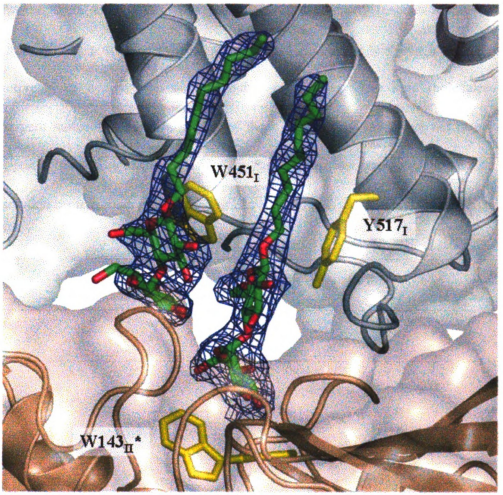

Figure 3.28: Two decyl maltoside detergent molecules resolved at the interface of two *Rs*C*c*O molecules (gray and wheat). The detergent molecules are colored by atom type (C: green; O: red; N: blue). Two different *Rs*C*c*O molecules are colored wheat and gray, respectively. The ($2F_o - F_c$) difference electron density map (blue) surrounding the decyl maltosides contoured at 1.0 σ is shown. Tyrosine and tryptophan residues (yellow) were found nearby the two decyl maltosides forming stacking interactions with the detergent sugar ring.

of column chromatography. It appears that when subunits III and IV dissociated from the enzyme complex, they take the associated lipids with them. In other locations, however, there were quite a few tube-like electron density features found in the transmembrane portion of the enzyme (Figure 3.29). These tube-like features were interpreted as hydrocarbon tails of either native membrane lipid molecules or detergent molecules. The headgroups of these hydrocarbon tails were not resolved, suggesting flexibility as in the case of the partial lipids identified even in the 1.55 Å resolution bacteriorhodopsin (Luecke *et al.*, 1999).

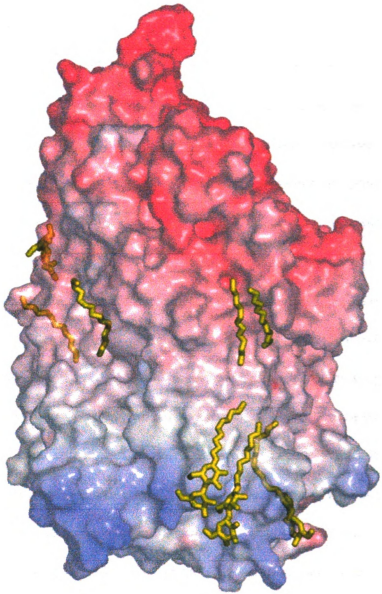

Figure 3.29: Structure of I-II subunit *Rs*CcO showing the resolved detergent molecules, detergent headgroups, and alkyl tails of detergents or membrane lipids. The protein surface is colored by charge (blue: positive; red: negative) and the resolved detergent molecules, detergent headgroups, and alkyl tails are shown in yellow.

Chapter 4. DISCUSSION

4.1 Importance of Homogeneous Subunits in the X-ray Diffraction of *Rs*CcO Crystals

X-ray crystallography of a membrane protein continues to be an extremely difficult task despite significant progresses made during recent years (Loll, 2003; Torres *et al.*, 2003; White, 2004). Besides the difficulty associated with working with protein detergent complexes, which is usual for membrane proteins (Garavito and Ferguson-Miller, 2001; Seddon *et al.*, 2004), the efforts to successfully crystallize *Rs*CcO, a multi-subunit integral membrane protein, have also been complicated by the fact that incomplete post-translational modification and processing of the enzyme subunits often leaves an inhomogeneous enzyme complex, which is detrimental to obtaining well ordered protein crystals. Such processing events include proteocleavage of the C-terminal 13 amino acid residues of the subunit II, as well as two different potential translation starting codons in the subunit IV gene and further proteocleavage processing of each form of subunit IV (see Results Section and Figure 2.1). In a systematic approach to improving the X-ray diffraction quality of the four subunit *Rs*CcO crystals, these inhomogeneities in subunits II and IV were remedied by molecular engineering of unique *R. s.* strains. Table 4.1 shows the different *R. s.* strains made and the different types of subunits II and IV in their expression products, as well as the protein expression levels and the diffraction limits of crystals obtained. It can be seen that in general, more homogeneous subunits lead to better diffraction of the four subunit *Rs*CcO crystals. This is particularly true in the case of

R. s. Strain	His-tag	Subunit II	Subunit IV	Expression	Best Crystal
120	Sub I	natural + processed[1]	long[4] + short[5] + processed long[6]	good	> 4 Å[8]
157	Sub I	natural + processed[1]	short[5] + processed short[7] + long[4]	good	4 Å[8]
119	Sub I	natural + processed[1] + truncated[2]	short[5] + processed short[7] + long[4]	poor	3.6 Å[8]
156	Sub I	truncated[2]	long[4] + processed long[6] + short[5]	poor	3.3 Å[8]
163	Sub I	truncated[2]	short[5] + processed short[7] + long[4]	poor	3.2 Å[8]
167	Sub II	his-tagged[3]	long[4] + processed long[6] + short[5]	good	3.05 Å[8]
169	Sub II	his-tagged[3]	short[5] + processed short[7] + long[4]	good	2.9 Å[8]
169Δ4	Sub II	his-tagged[3]	short[5] + processed short[7]	fair	3.3 Å[8] 2.35 Å[9]
37Δ4	Sub II	his-tagged[3]	-	fair	2.4 Å[9]

1, 2, 3, 4, 5 see Table 2.1
6 long subunit IV – N-terminal 13 aa (short subunit IV – N-terminal ala-asp).
7 short subunit IV – ala.
8 diffraction limit of the four subunit crystal along the best direction
9 diffraction limit of the I-II subunit crystal

Table 4.1: Summary of different *R. s.* strains with different types of subunits II and IV in their expression products, their protein expression levels and the diffraction resolution limits of crystals obtained.

subunit II, deduced by comparing the diffraction limit of crystals obtained from *R. s.* strain 120, 119, and 156, which shows significant improvements in X-ray diffraction limit (from worse than 4 Å to approximately 3.2 Å) upon removing the inhomogeneity in subunit II.

In the case of subunit IV, similar observations could also be made by pair-wise comparison between *Rs*CcO crystals obtained from strains 120 and 157, 156 and 163, and 167 and 169, in which cases a slight improvement the in X-ray diffraction limit (0.1 – 0.2 Å) was observed when the short subunit IV gene was inserted into the overexpression plasmid rather than the complete subunit IV gene. If the MALDI mass spectrometry analyses of different forms of subunit IVs from *R. s.* strain 169 can be applied to other strains of *R. s.* which have the same subunit IV gene in their overexpression plasmids, (see 3.2.1, Figure 3.16 (A) and (B) and Table 2.1), then in the protein product from the *R. s.* strains 157, 163 and 169, the short and proteolytic cleaved short form (difference of an alanine residue) should be the predominant species of subunit IV. Likewise, if the MALDI mass spectrometry analyses of different forms of subunit IVs from *R. s.* strain 207 can be applied to other strains of *R. s.* which have the same long subunit IV gene in their overexpression plasmids, (see 3.2.1, Figure 3.16 (A) and (B) and Table 2.1), then in the protein product from the *R. s.* strains 120, 156 and 167, the long and proteolytic cleaved long form (difference of 12 amino acid residues) were the predominant subunit IV species. In the former case, the inhomogeneity in subunit IV is much less severe than that in the latter case, which could lead to slightly better X-ray diffraction in the crystals.

Somewhat surprisingly, when *Rs*CcO obtained from strain 169Δ4 was used as a crystallization candidate, the crystal diffraction resolution limit was worse than that obtained from strain 169 and 167 (3.3 Å vs. 2.9 Å and 3.1 Å, respectively), although the subunit IV in *Rs*CcO obtained from strain 169Δ4 was more homogeneous than that from strain 169 (see Figure 3.16(C)). Since *Rs*CcO obtained from strain 169Δ4 did not contain any long form of subunit IV, whereas *Rs*CcO from strain 169 contained a very small amount of subunit IV, the observed difference in diffraction limit could be due to the long form of subunit IV being somehow beneficial for obtaining well-ordered crystals, since the long form of subunit IV seems to be selected more favorably during nucleation/crystal growth processes. It is also observed that four subunit *Rs*CcO crystals obtained from strain 169Δ4 are generally smaller than those obtained from strains 167 and 169. In fact, no crystals similar to the sizes of the best crystals obtained from 167 and 169 have been obtained, which could be another reason why the diffraction was worse, since it has been found that larger *Rs*CcO crystals generally diffract further than the smaller ones. Therefore, it seems that a homogeneous long form of subunit IV could be more helpful in obtaining well diffracting four subunit *Rs*CcO crystals. Generation of such a strain of *R. s.* would require at least a few mutations to remove the second starting codon as well as the proteolytic cleavage site 3 amino acids downstream, which could be technically challenging and time consuming.

Although *R. s.* strain 169Δ4 did not lead to improvement in X-ray diffraction of the four subunit *Rs*CcO crystal, its use as the crystallization candidate did lead to

formation of the I-II subunit crystal. The more homogeneous and long subunit IV-free *Rs*C*c*O complex obtained from strain 169Δ4 turned out to be important since *Rs*C*c*O obtained from strain 167 failed to produce any I-II subunit crystals under similar crystallization conditions. It is possible that the long form of subunit IV binds to the enzyme complex more tightly than the short form of subunit IV, and is therefore harder to be removed from the enzyme complex under the crystallization conditions for the I-II subunit *Rs*C*c*O crystal to form.

One puzzling observation made is that the protein expression level of *R. s.* strains 119, 156 and 163 were extremely low, presumably due to deletion of the C*c*O gene(s) from its overexpression plasmid while keeping the drug resistance gene(s) during bacterial growth. As a result, *R. s.* cells that have successfully deleted the C*c*O gene will gain a growth advantage over other cells and thus self-replicate much faster and consume almost all the nutrients in the growth media with no production of *Rs*C*c*O. A cursory examination of those *R. s.* strains revealed that they all have genes for the artificially truncated form of subunit II (see Figure 2.1 and Table 2.1) and either long or short subunit IV in their overexpression plasmid, although it is not clear if these characteristics are important. The exact reasons for the occurrence of C*c*O gene deletion to occur and ways to prevent it have not been found.

4.2 Effects of the Histidine Tag and Metal Ions on X-ray Diffraction of *Rs*C*c*O Crystals

Table 4.1 also shows the effects of the position of the histidine tag on the diffraction resolution limit of *Rs*C*c*O crystals. It can be seen that, in general, crystals

of the four subunit *Rs*C*c*O with a histidine tag attached to the shortened C-terminus of subunit II have better X-ray diffraction than those with the histidine tag attached to the C-terminus of subunit I. One of the reasons for such an improvement is that the histidine-tagged subunit II is homogeneous. Another potential reason could be that the engineered histidine tag might have helped to form a new crystal contact. As observed in the crystal structure obtained from strain 167, shown in Figure 3.8, extra electron density could be seen which appeared to connect the C-terminus of subunit II to another molecule. This continuous piece of electron density might suggest that the histidine tag was immobilized and contributed to making new crystal contacts, although the modeling of the histidine tag was not completed. However, similar electron density was not observed in this area in the structure of the crystal obtained from *R. s.* strain 169, although it also possessed a histidine-tagged subunit II. A possible explanation of this discrepancy could be that the difference in subunit IV contents between *Rs*C*c*O obtained from 167 and 169 leads to the observed differences seen in this area, since the extra piece of electron density observed in the crystal structure of *Rs*C*c*O from strain 167 (Figure 3.8) is too large and consistent to be purely noise. However, when a different X-ray crystallographic refinement program, Refmac5, was used, no such large electron density was observed after a TLS refinement followed by a restrained refinement.

The role of the engineered histidine tag at the near C-terminus of subunit II in forming crystal contacts in the I-II subunit *Rs*C*c*O crystallization is unequivocal. As shown in Figure 3.23, the major crystal contacts between two adjacent *Rs*C*c*O

molecules are mediated through the exogenous cadmium ions. Each cadmium ion is ligated in a tetrahedral coordination geometry by the side chains of three amino acid residues, including two histidines and one glutamic acid, from one protein molecule and one other glutamic acid residue from another protein molecule. Interestingly, the two participating histidine residues, $H283_{II}$ and $H285_{II}$, are from the engineered histidine tag.

One of the commonly used divalent cation crystallization additives, cadmium, has the ability to coordinate with amino acid residues, water, or other solutes in the crystallization mixture with different degrees of coordination. As a result, cadmium ions have been resolved in a large number of crystal structures, many of them occurring in the crystal contact regions as seen in the current structure (Trakhanov and Quiocho, 1995; Trakhanov *et al.*, 1998). What is more interesting about this crystal structure is that two of the ligating amino acid residues for each cadmium are from the engineered histidine tag. Histidine tags have rarely been resolved in crystal structures, except for a few instances (Zhou *et al.*, 2000; Brych *et al.*, 2001; O'Neill *et al.*, 2001; Stroebel *et al.*, 2003), because they are generally flexible and it is often times beneficial for crystallographers to cleave off the histidine tag before crystallization (Ma and Chang, 2004 , Harman, personal communication). However, the analysis of the I-II subunit *Rs*C*c*O crystal structure clearly indicates the essential role of the engineered histidine tag in forming key crystal contacts. Similar observations were made in the crystal structure of the B1 domain of a mutant protein L from *Peptostreptococcus magnus*, in which case the entire histidine tag was found

coordinated with zinc ions at the protein-protein interface (O'Neill *et al.*, 2001), and in the crystal structure of ArsA ATPase, in which case the histidine tag was involved in a crystal contact via a tetrahedral coordination of cadmium with one of the ligands being a water molecule (Zhou *et al.*, 2000). An engineered internal, rather than N- or C- terminal histidine tag, was successful in aiding purification and crystallization of the membrane protein siderophore receptor FhuaA. In the crystal structure, a nickel ion was found at the molecular interface coordinating with residues from the histidine tag (Ferguson *et al.*, 1998; Ferguson *et al.*, 1998). Therefore histidine tags, through strong interaction with other species, particularly metals, can be of general use in protein crystallization under the right conditions.

4.3 Effects of Membrane Lipids on the X-ray Diffraction Quality of *Rs*CcO Crystals

4.3.1 Importance of Lipid Retention in Obtaining High Resolution Crystal of *Rs*CcO

It has been generally realized that the role of lipids in the crystallization of membrane proteins is to maintain a more stable and homogeneous conformation of membrane proteins. Lipid molecules are resolved in many high resolution membrane protein crystal structures including that of *Rs*CcO (Svensson-Ek *et al.*, 2002). During detergent solublization and protein purification steps, efforts were made to retain the specifically bound lipid molecules on *Rs*CcO, including measuring the protein concentration and calculating the amount of dodecyl maltoside detergent to be added to the membrane sample, the use of different columns for protein purification,

decreasing the number of times of washing and detergent exchange, and using a lower concentration of decyl maltoside detergent in the buffer for crystallization. Lipids were also added to the crystallization mixtures. Measurements of lipids by using mass spectrometry, phosphorous analysis and ICP were also taken during different stages of protein purification in an effort to monitor the lipid content. Although no remarkable improvement in X-ray diffraction was achieved in the four subunit *Rs*C*c*O crystals, such critical experiments should be performed routinely in order to understand the lipid content changes when different purification techniques are used and at different stages during the protein production process.

4.3.2 Use of Mass Spectrometry in Monitoring Lipid Contents during Protein Preparation of *Rs*C*c*O for Crystallization

In order to study the lipid contents during different stages of protein production of *Rs*C*c*O using different column purifications, MALDI-TOF mass spectrometry has been used to monitor the lipid contents directly from protein samples during each step of purification without the need for lipid extraction since lipid extraction using organic solvents might lead to oxidation of lipid molecules. Because of its very high sensitivity and relative ease, MALDI-TOF mass spectrometry could be used as an analytical tool for providing us with critical information on lipid content. Careful analysis of the m/z peaks, together with tandem MS/MS analysis can provide great details on the exact lipid species, including the headgroup type, acyl chain length and its degree of unsaturation. However, because the amount of each species desorbed from the probe may not be proportional to the

amount in the sample, MALDI-TOF analysis is not a quantitative method. Although accurate identification on lipid species can be obtained, direct comparisons of lipid contents in different samples cannot be made. Once a reliable standard control can be established, the peak heights of each lipid species can then be compared to those of standards to compare the lipid contents directly among different samples. Another useful ionization technique used in mass spectrometry, electrospray ionization (ESI), has the advantage of being both sensitive and quantitative. However, this method involves lipid extraction from the sample, which could lead to the oxidation and degradation of lipids. Extraction protocols which could lead to little or no lipid loss are being developed.

4.3.3 Conserved Lipid Binding Sites Found in the Structure of I-II Subunit *Rs*CcO and Potential Substitution of Lipids by Detergents

It was somewhat surprising that in the I-II subunit *Rs*CcO crystals, no lipids were found that corresponded to any of the 6 PEs found in the published four subunit *Rs*CcO crystal structure despite efforts to retain more lipids during the protein purification process. However, there are a few detergent molecules, detergent headgroups and other linear molecules which could be hydrocarbon tails of detergents/lipids resolved at the surface of the I-II subunit structure. A very interesting observation was made when the crystal structures of the two I-II subunit CcOs from *R. s.* and *P. d.* (PDB entry 1AR1) were overlaid, including the resolved partial detergent/lipid molecules. Figure 4.1 (A) and (B) shows the surface representations of

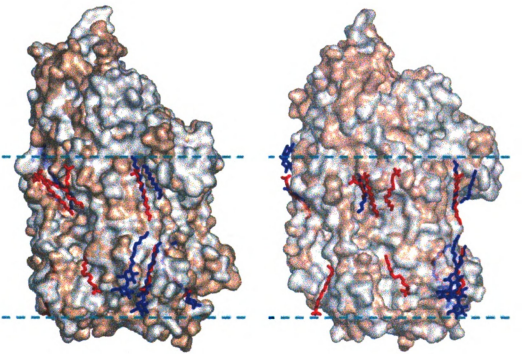

Figure 4.1: Superimposed surface representations of I-II subunit *Rs*CcO (gray) and *Pd*CcO (wheat) together with the detergent molecules, maltose headgroups and alkyl chains resolved from the structure of *Rs*CcO (blue) and the resolved detergent LDAOs from *Pd*CcO (red). The two figures represent views from two different angles. Note that quite a few of these linear molecules from the two structures occupy the same sites on protein surface.

the superimposed structures of *Rs*C*c*O (grey) and *Pd*C*c*O (salmon) together with the detergent molecules, maltose headgroups and alkyl chains of *Rs*C*c*O (blue) and the resolved detergent LDAOs from *Pd*C*c*O (red) (Ostermeier *et al.*, 1997). The two figures represent views from two different angles. The positions and orientations of these linear molecules likely represent where membrane lipids reside. Moreover, many of these linear molecules from the two different organisms occupy the same positions on the surface of the protein, although the two protein structures were from two different species and the protein underwent different purification and crystallization procedures. This suggests that these locations could be conserved sites for specific interactions between the membrane lipids and the transmembrane protein surface. In fact, analyses of our structure superimposed with the 1.8 Å resolution bovine mitochondrial C*c*O structure revealed that one of the proposed alkyl chains in *Rs*C*c*O not only coincides with an LDAO molecule from *Pd*C*c*O structure as shown in the Figure 4.1, but also coincides with the glycerol backbone and part of the acyl tail of a lipid molecule, triacylglcerol, resolved in the bovine C*c*O crystal structure, as shown in Figure 4.2. The physiological role of triacylglycerol in mitochondrial C*c*O is not completely understood; also unclear is whether triacylglycerol is present in the *R. s.* cytoplasmic membrane. Direct examples of specific, conserved lipids on the membrane protein surface also come from the published crystal structures of C*c*O from *R. sphaeroides* (PDB entry 1M56), *P. denitrificans* (PDB entry 1QLE), and bovine mitochondria (PDB entry 1V54), in which case a phospholipid molecule was found to reside at the same position within the corner of the V-shaped cleft formed by

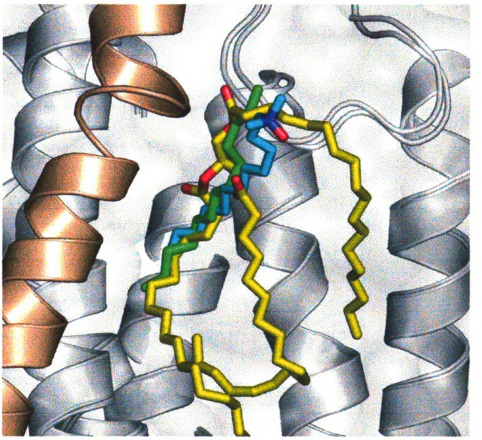

Figure 4.2: Structure overlay of I-II subunit *Rs*CcO, I-II subunit *Pd*CcO (PDB entry 1AR1), and bovine heart mitochondrial CcO (PDB entry 1V54). The transmembrane helices of subunits I and II of these CcOs are very similar and they are shown in gray. Subunit VIc from bovine CcO is shown in wheat. Resolved alkyl tail from the I-II subunit *Rs*CcO is shown in green, the detergent LDAO in *Pd*CcO is shown by atom color (carbon: cyan; oxygen: red; nitrogen: blue), and the resolved triacyl glycerol in the bovine CcO structure is shown by a different atom color scheme (carbon: yellow; oxygen: red).

helix bundles of subunit III in all three structures as shown in Figure 4.3. At a nearby site at the interface of subunits I and III, a conserved lipid was also found in the structures of both *Rs*C*c*O and bovine heart mitochondria C*c*O (Figure 4.3). Similarly, in the crystal structures of cytochrome bc_1 complex from yeast (PDB entry 1KB9), chicken (PDB entry 1BCC) and bovine (PDB entry 1PP9), a conserved phosphatidyl ethanolamine was found to reside at the same position on the protein surfaces in all three structures as shown in Figure 4.4 (Zhang *et al.*, 1998; Lange *et al.*, 2001).

In our structure where detergents were resolved, tyrosine and tryptophan residues were found nearby forming a stacking interaction between the sugar ring and the aromatic rings as shown in Figure 3.28. Such stacking interactions are often found involved in sugar binding in carbohydrate metabolizing enzymes (Roujeinikova *et al.*, 2001; Roujeinikova *et al.*, 2002), and the same intimate interactions between the headgroup of sugar-based detergent and aromatic residue rings have also been observed in a number of other membrane protein structures as well (Snijder *et al.*, 2001; Sui *et al.*, 2001; Okada *et al.*, 2002; Tajkhorshid *et al.*, 2002). Tryptophan and tyrosine, in addition to other amino acid residues such as arginine, lysine, histidine, and threonine, have been found to reside at the membrane interface and associate themselves with the phosphatidyl head groups of lipids (Yau *et al.*, 1998). Therefore, detergent headgroups that can mimic phosphatidyl headgroups, both by polar interactions with surrounding residues and rigid stacking interactions with aromatic rings, could occupy the same sites. The success of alkyl glycoside detergents such as maltosides and glucosides in both stabilizing and crystallizing

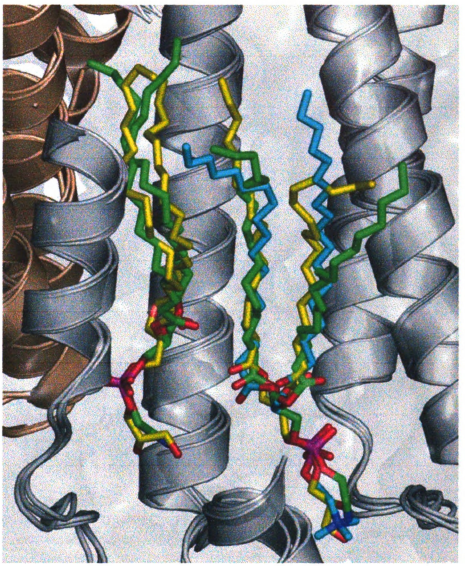

Figure 4.3: Structure overlay of *Rs*C*c*O (PDB entry 1M56), *Pd*C*c*O (PDB entry 1QLE) and bovine heart mitochondrial C*c*O (PDB entry 1V54) showing the conserved phospholipid molecules. The transmembrane helices of subunits I and III from the three crystal structures are very similar and they are shown in wheat and gray, respectively. There are two conserved lipid sites shown in the picture. The one on the right is found in the C*c*O crystals structures from *R. s.*, *P. d.*, and bovine. The one on the left is found in the C*c*O crystal structures of *R. s.* and bovine. The resolved phosphatidyl ethanolamine molecule in the *Rs*C*c*O structure is shown by atom type (C: green; O: red; N: blue; P: purple), resolved phosphatidyl choline molecule in the *Pd*C*c*O structure is shown by a different atom type scheme (C: cyan; O: red; N: blue; P: purple) and resolved phosphatidyl glycerol molecule in the bovine C*c*O structure is shown by another different atom type scheme (C: yellow; O: red; N: blue; P: purple).

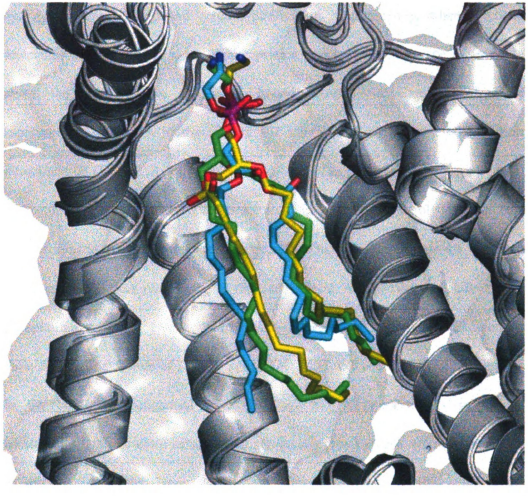

Figure 4.4: Structure overlay of cytochrome bc_1 complexes from yeast (PDB entry 1KB9), chicken (PDB entry 1BCC), and bovine (PDB entry 1PP9) showing the conserved phosphatidyl ethanolamine molecule. The transmembrane helices from the three crystal structures shown are very similar and they are shown in gray. Resolved phosphatidyl ethanolamine molecule in the crystal structure from yeast is shown by atom type (C: cyan; O: red; N: blue; P: purple). Resolved phosphatidyl ethanolamine molecule in chicken is shown by a different atom type scheme (C: yellow; O: red; N: blue; P: purple). Resolved phosphatidyl ethanolamine molecule in bovine is shown by another different atom type scheme (C: green; O: red; N: blue; P: purple).

membrane proteins may be due to their ability to interact in a manner similar to phospholipids, and therefore partially replace those specifically bound lipids that are lost during solublization and column purification. Consequently, when detergent molecules are resolved in a membrane protein structure, they may be expected to reveal the position of a specifically bound phospholipid. Careful analysis of superimposed structures of the current I-II subunit *Rs*C*c*O and the bovine heart mitochondrial C*c*O (PDB entry 1V54) indicated that in the sites where the two decyl maltosides are found in the *Rs*C*c*O structure, a phosphatidyl glycerol (PG) molecule was resolved in the bovine heart mitochondrial C*c*O as shown in Figure 4.5 with each decyl maltoside occupying roughly the site of each of the two acyl tails of the phospholipid molecule. (As shown in Figure 4.1, there is a resolved LDAO detergent molecule in the structure of I-II subunit *Pd*C*c*O (PDB entry 1AR1) at this same site). In the bovine mitochondrial C*c*O structure, the PG molecule is surrounded additionally by three small subunits that are not found in bacterial enzymes as shown in wheat color in the figure. These extra subunits probably further stabilize the binding of the lipid through additional interactions. It is plausible that initially a phospholipid molecule was occupying the same site in *Rs*C*c*O, but was lost during detergent solublization and protein purification partially due to the absence of the extra subunits that are found in the bovine mitochondrial enzyme. Two decyl maltoside molecules bound to this conserved phospholipid site because of their ability to mimic the lost lipid. Similarly, in the structure of cytochrome bc_1 complex from chicken and bovine, a phosphatidyl ethanolamine (PE) from the bovine structure and

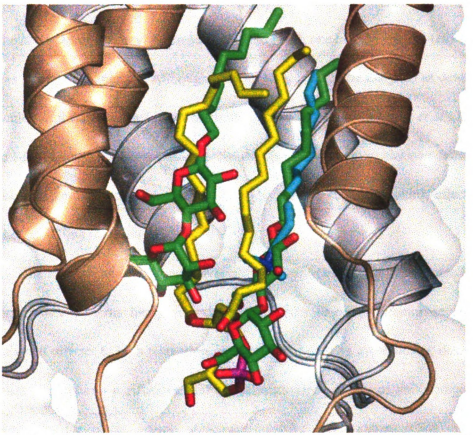

Figure 4.5: Structure overlay of I-II subunit *Rs*C*c*O, I-II subunit *Pd*C*c*O (PDB entry 1AR1), and bovine heart mitochondrial C*c*O (PDB entry 1V54). The transmembrane helices of subunits I and II these C*c*Os are very similar and they are shown in gray. Subunits IV, VIIb, and VIII from bovine C*c*O are shown in wheat. Resolved decyl maltosides from the I-II subunit *Rs*C*c*O is shown by atom color (carbon: green; oxygen: red), the detergent LDAO in *Pd*C*c*O is shown by a different atom color scheme (carbon: cyan; oxygen: red; nitrogen: blue), and the resolved phosphatidyl glycerol molecule in the bovine C*c*O structure is shown by a third atom color scheme (carbon: yellow; oxygen: red; phosphorous: purple).

a detergent octyl glucoside molecule from the chicken structure were found at the same positions with the glucoside head group superimposed onto the phosphate group and the alkyl tail of the octyl glucoside coinciding with one of the two acyl tails of the lipid as shown in Figure 4.6. Although lipid molecules could be assigned as detergent molecules until the advent of structures with higher resolution (McAuley *et al.*, 1999), in the I-II subunit *Rs*C*c*O structure, the clear detergent head group electron density is unequivocal and the structure overlay strongly suggest such mimicking effects of detergents on lipid molecules.

The above findings suggest that specific interactions between membrane lipids and membrane proteins likely do exist and in order to obtain membrane protein crystals that diffract to high resolution, special care should be given during detergent solublization, column purification and crystallization procedures to retain important lipid species for better overall structural integrity and stability (Garavito and Ferguson-Miller, 2001).

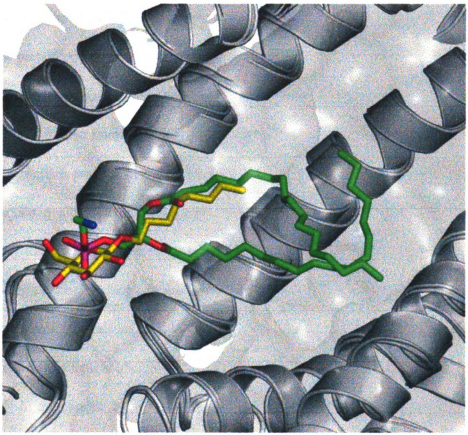

Figure 4.6: Structure overlay of cytochrome bc_1 complexes from chicken (PDB entry 1BCC), and bovine (PDB entry 1PP9). The transmembrane helices from the two crystal structures shown are very similar and they are shown in gray. Resolved phosphatidyl ethanolamine molecule in the crystal structure from bovine cytochrome bc_1 complex is shown by atom type (C: green; O: red; N: blue; P: purple). At the same site, an octyl glycoside shown by a different atom color scheme (C: yellow; O: red; P: purple) was resolved in the chicken cytochrome bc_1 complex structure. Note that the headgroup of the detergent correspond to the headgroup of the phosphatidyl ethanolamine molecule and the alkyl tail of the detergent corresponded to one of the two acyl tails of the lipid.

Chapter 5. FUTURE PLANS

5.1 Improvement of the X-ray Diffraction of Crystals of *Rs*C*c*O

Although current I-II *Rs*C*c*O crystals diffract X-rays isotropically up to 2.35 Å resolution, and the structure has been refined with satisfactory R and R_{free} factors, more experiments need to be performed in order to obtain crystals of *Rs*C*c*O that diffract beyond the current resolution to better resolve changes that occur in mutant forms, particularly in water organization.

5.1.1 New Strains of *Rhodobacter sphaeroides* with Different Subunit Contents

It has been found that removing flexible loops on the surface of a protein can help crystallize proteins that are otherwise hard to crystallize and/or improve crystal diffraction quality (Derewenda, 2004). This can be done by limited proteolysis to identify the flexible surface loop regions, followed by removing the DNA sequences encoding the flexible loops. In the case of the crystallization of the ammonia channel from *E. coli*, crystals of artificially truncated protein diffract X-rays to 1.35 Å resolution (Khademi *et al.*, 2004).

In the current *Rs*C*c*O structure, there are terminal amino acid sequences that are not resolved, especially in subunit I, most likely due to their being flexible. Therefore, these sequences are good candidates for being excised for optimized crystal packing. Efforts to make protein complexes with excised portions of subunits are currently underway and the effects will be tested should the new protein complex successfully crystallize.

New strains of *R. s.* can also be made which coexpress the membrane

associated cytochrome c_y with C*c*O. The N-terminal membrane anchor domain of cytochrome c_y (Myllykallio *et al.*, 1997; Myllykallio *et al.*, 1999) could be linked to the C-terminus of subunit I of *Rs*C*c*O, allowing stoichiometric coexpression and copurification of the *Rs*C*c*O-cytochrome c_y complex. Crystallization experiments can then be performed with the complex, with the aim of testing the location of proposed binding sites of cytochrome *c* to C*c*O based on molecular modeling studies (Roberts and Pique, 1999). It is also conceivable that the larger, more hydrophilic cytochrome *c*-C*c*O complex will also produce higher resolution crystals.

5.1.2 Screening New Conditions for Detergents, Protein Production, Crystallization and Crystal Handling / Flashcooling

Previous results (see Chapters 3 and 4) have indicated that many factors, including detergent solublization, protein purification and crystallization, and crystal handling/flashcooling, affect the crystal diffraction quality greatly. Further modification of all these steps can be tried and their effects can be studied in order to find the optimal conditions for maximum crystal diffraction quality.

For example, new detergents, such as 3-oxatridecyl-α-D-mannoside, as well as the glucoside and maltoside derivatives, which were successfully used for crystallization of C*c*O from bovine heart mitochondria at 1.6 Å resolution (Yoshikawa, personal communication), can be tested for membrane solublization, protein purification and crystallization.

A novel technique for cryocooling protein crystals has recently been developed (Kim *et al.*, 2005). Flashcooling protein crystals under pressure up to 200

MPa in He gas without the use of cryoprotectant has been shown to improve the diffraction quality for a number of protein crystals (Kim *et al.*, 2005). This novel technique can be tested on crystals of *Rs*C*c*O with the hope of improving their diffraction resolution and decreasing the crystal mosaicity.

5.1.3 Purification of I-II Subunit *Rs*C*c*O as a Crystallization Candidate

Currently, the I-II subunit crystals of *Rs*C*c*O are obtained from a crystallization drop containing purified three subunit (from *R. s.* strain 37Δ4) or four subunit (from *R. s.* strain 169Δ4) enzyme after several weeks, conditions that are hard to control. Moreover, the crystals of the I-II subunit *Rs*C*c*O obtained from *R. s.* strain 169Δ4 emerged from showers of the four subunit *Rs*C*c*O crystals. Coexistence of these two crystal forms in the drop can lead to difficulties in crystal handling. It is also conceivable that during crystal growth, the incorporation of three or four subunit *Rs*C*c*O might negatively affect the quality of growing I-II subunit crystals. Therefore, experiments can be performed to try to purify the I-II subunit *Rs*C*c*O for crystallization trials. The I-II subunit *Rs*C*c*O, if successfully obtained and purified, maybe a better candidate for crystallization trials due to its homogeneity.

Previously, I-II subunit *Pd*C*c*O was obtained by the use of the harsh detergent LDAO (Ostermeier *et al.*, 1997). Similar experiments can also be performed on *Rs*C*c*O in order to obtain pure I-II subunit enzyme by using LDAO and other detergents. The gene encoding subunit III can also be removed from the *R. s.* genome with no detrimental effects on bacterial growth and C*c*O expression as previously reported (Haltia *et al.*, 1989; Bratton *et al.*, 2000); the resulting subunit III-less protein

complex might be a good crystallization candidate, although subunit IV is still present (Hosler *et al.*, personal communication). Therefore, crystallization trials can be performed on protein complexes obtained from subunit III-deleted and subunits III/IV-deleted *R. s.* strains if the I-II subunit enzyme can be successfully expressed and purified.

5.2 Crystal Structure of *Rs*C*c*O Complexed with Arachidonic Acid

Arachidonic acid is found to increase the activity of D-pathway mutants, such as D132A (Fetter *et al.*, 1996), and to prevent suicide inactivation of subunit III-less *Rs*C*c*O (Fetter *et al.*, 1996; Mills and Hosler, 2005). The proposed mechanism is that binding of arachidonic acid in the vicinity of the D pathway enhances the proton uptake through the D pathway and therefore offsets the effects of mutation and loss of subunit III on the D pathway (Fetter *et al.*, 1996; Mills and Hosler, 2005). However, the exact binding site(s) for arachidonic acid remains unclear. A crystal structure of *Rs*C*c*O complexed with arachidonic acid could help locate the binding site(s) for arachidonic acid and help our understanding of the D proton pathway and proton transport along this pathway.

In order to obtain a crystal structure of *Rs*C*c*O complexed with arachidonic acid, two approaches will be used. First, arachidonic acid will be added to the crystallization solution and hopefully will cocrystallize with *Rs*C*c*O from the solution. Alternatively, crystals of I-II subunit *Rs*C*c*O can be soaked in a solution containing arachidonic acid for a period of time for arachidonic acid to bind before cryocooling.

5.3 Crystal Structures of Key Mutants of *Rs*C*c*O

Great progress has been made in our understanding of the structure/function of C*c*O during the past decade, especially after the crystal structures of C*c*Os from a variety of different sources were solved (Iwata *et al.*, 1995; Tsukihara *et al.*, 1995; Tsukihara *et al.*, 1996; Ostermeier *et al.*, 1997; Yoshikawa *et al.*, 1998; Svensson-Ek *et al.*, 2002). However, these high resolution crystal structures of wild type C*c*Os have not been able to help elucidate the exact proton pumping mechanism and how electron transfer and proton translocation are coordinated in time and space. In order to understand this central issue in bioenergetics, more high resolution crystal structures of various forms of C*c*O are needed, with their resolved water molecules. The latter can provide us with important information on amino acid side chain and proton movements during the process. Thus, obtaining high resolution crystal structures of various key mutants of *Rs*C*c*O is a high priority.

Table 5.1 shows some of the mutant *Rs*C*c*Os whose structure determination will be attempted using the established method. These mutants all exhibit, or are predicted to exhibit, pronounced functional changes as measured by kinetic and spectroscopic methods, and it is proposed that different water arrangements may be involved in the observed changes. It is also important to choose mutants that are structurally stable and likely to withstand purification and crystallization.

For example, one of the most interesting mutants involves the Cu_A ligand, $M263_{II}L$. The missing Cu_A ligand Met is envisioned to be replaced with a water molecule. As a result, the two Cu_A atoms are still in place but exhibit perturbed

Mutants	Position	Observed/Predicted Functional Changes
$M263_{II}L$	Cu_A center ligand	increased redox potential of Cu_A decreased electron transfer rate to heme *a*
$R481_IK$	heme a/a_3 ligand	increased respiratory control ratio decreased heme *a* redox potential
$K362_IM$	K-pathway	blocked proton uptake through K pathway
$T359_IA$	K-pathway	slowed proton uptake through K pathway
$D132_IA$	D-pathway	blocked proton uptake through D pathway
$D132_IA/R481_IK$	D-pathway and H^+ exit pathway	blocked D pathway proton uptake and blocked proton exit/backflow pathway
$Q276_IR$	H^+ backflow path	blocked proton back flow pathway (predicted)
$T352_IS$	H-bonded to a Cu_B ligand, $H333_I$	perturbed oxidase reaction and proton translocation
$V330_IS/D$	ligand of a water chain between the D path and the binuclear center	changes in proton delivery to the binuclear center through D pathway during the oxidative phase of oxygen chemistry (predicted)

Table 5.1: Mutants of *Rs*C*c*O whose crystal structure determinations will be attempted using the established method and their observed/predicted functional changes.

spectral properties and an approximately 100mV increase in their redox potential. Electron transfer from Cu_A to heme *a* is severely hindered without much effect on proton transfer (Zhen *et al.*, 2002). A crystal structure of this mutant will lead to elucidation of the localized effect on the Cu_A center within this region and better understanding of the coupling between proton pumping and electron transfer.

Other interesting mutant forms of *Rs*C*c*O are mutants of the arginine pair ($R481_I$, $R482_I$) which are associated with the propionate groups of the heme groups either directly or via hydrogen-bonded networks of water molecules. These arginines are along the proposed proton exit channel, as well as involved in electron transport from Cu_A center to heme *a* (Mills *et al.*, 2000; Qian *et al.*, 2004). Mutants of these two arginines lead to severely perturbed electron transfer from Cu_A to heme *a*, as in the case of $R482_IP$, or very subtle changes in activity and proton pumping, as found in $R481_IK$ (Qian *et al.*, 2004). Based on MD calculations (Seibold *et al.*, 2005), the $R481_IK$ mutant was proposed to lead to conformational changes in residues in the loop between helix III and helix IV and altered water arrangements. Because of the central position of the arginine pairs, a high resolution crystal structure of the arginine mutants with resolved water molecules can help us understand the structural basis of the observed functional changes and understand the entire processes of electron transfer and proton translocation.

Mutants that impair proton uptake pathways would also be desirable for structural determination. These include mutants that impaired the proton uptake through the K pathway, such as $K362_IM$ and $T359_IA$ (Fetter *et al.*, 1995), as well as

$T359_I$D/N (Sharpe *et al.*, personal communication), and mutants that impaired the D pathway, $D132_I$A (Fetter *et al.*, 1995) and $D132_I$A/$R481_I$K double mutant (Mills *et al.*, 2005). Besides the mutants that affect the proton uptake pathway, several other mutants that are predicted to be involved in proton translocation have been designed and the structure determination of them will be attempted. These include: $Q276_I$R, which is proposed to block the proton backflow pathway (Sharpe *et al.*, personal communication); $T352_I$S, which is proposed to affect one of the Cu_B ligands, $H333_I$, central in both the oxygen reduction reaction and proton translocation (Sharpe *et al.*, 2005); and $V330_I$S/D, which is proposed to lead to changes in the proton transfer to the active site from the D pathway (Sharpe *et al.*, personal communication).

5.4 Kinetic and Crystallographic Studies of K-pathway Mutants Which Abolish Cd^{2+} Binding

As shown in the Results section (Chapter 3), the proposed binding site for Cd^{2+} on the inside of the enzyme is at the entrance of the K proton pathway. The proposed Cd^{2+} binding ligands are $H96_{II}$ and $E101_{II}$ (Figure 3.11). Mutants that are designed to abolish the potential binding sites for Cd^{2+} at the entrance of the K proton pathway are currently being made, including $H96_{II}$A, $E101_{II}$A, and $H96_{II}$A/$E101_{II}$A double mutant. Kinetic studies of enzymatic activity in the presence of Zn^{2+}/Cd^{2+} will be performed to test if this site is indeed the inhibitory site of Zn^{2+}/Cd^{2+} and crystal structure of these mutants will be solved to confirm that no Cd^{2+} can bind to this site due to such mutations.

5.5 Summary

In summary, high resolution crystal structures with the resolved water molecules will help determine the structural basis of the mechanism of energy conservation. The currently established protein purification, crystallization and crystal handling protocols make this goal achievable. Knowledge and experiences gained from these studies can also help us understand how to obtain high resolution membrane protein crystals in general, and to elucidate the biology of membrane protein - lipid interactions.

BIBLIOGRAPHY

Aagaard, A., Namslauer, A., and Brzezinski, P. (2002). Inhibition of proton transfer in cytochrome c oxidase by zinc ions: delayed proton uptake during oxygen reduction. Biochimica et Biophysica Acta *1555*, 133-139.

Antunes, F., Boveris, A., and Cadenas, E. (2004). On the mechanism and biology of cytochrome oxidase inhibition by nitric oxide. Proceedings of the National Academy of Sciences of the United States of America *101*, 16774-16779.

Axelrod, H. L., Abresch, E. C., Paddock, M. L., Okamura, M. Y., and Feher, G. (2000). Determination of the binding sites of the proton transfer inhibitors Cd2+ and Zn2+ in bacterial reaction centers. Proceedings of the National Academy of Sciences of the United States of America *97*, 1542-1547.

Bailey, S. (1994). The CCP4 suite: programs for protein crystallography. Acta Crystallographica, Section D: Biological Crystallography *D50*, 760-763.

Bartlett, G. R. (1959). Phosphorus assay in column chromatography. Journal of Biological Chemistry *234*, 466-468.

Beauvoit, B., and Rigoulet, M. (2001). Regulation of cytochrome c oxidase by adenylic nucleotides. Is oxidative phosphorylation feedback regulated by its end-products? IUBMB Life *52*, 143-152.

Benning, C., Huang, Z.-H., and Gage, D. A. (1995). Accumulation of a novel glycolipid and a betaine lipid in cells of Rhodobacter sphaeroides grown under phosphate limitation. Archives of Biochemistry and Biophysics *317*, 103-111.

Berry, E. A., Zhang, Z., Bellamy, H. D., and Huang, L. (2000). Crystallographic location of two Zn2+-binding sites in the avian cytochrome bc1 complex. Biochimica et Biophysica Acta *1459*, 440-448.

Borisov, V. B. (2002). Defects in mitochondrial respiratory complexes III and IV, and human pathologies. Molecular Aspects of Medicine *23*, 385-412.

Bottcher, B., Scheide, D., Hesterberg, M., Nagel-Steger, L., and Friedrich, T. (2002). A novel, enzymatically active conformation of the Escherichia coli NADH:ubiquinone oxidoreductase (complex I). Journal of Biological Chemistry *277*, 17970-17977.

Branden, M., Tomson, F., Gennis, R. B., and Brzezinski, P. (2002). The Entry Point of the K-Proton-Transfer Pathway in Cytochrome c Oxidase. Biochemistry *41*, 10794-10798.

Bratton, M. R., Hiser, L., Antholine, W. E., Hoganson, C., and Hosler, J. P. (2000). Identification of the Structural Subunits Required for Formation of the Metal Centers in Subunit I of Cytochrome c Oxidase of Rhodobacter sphaeroides. Biochemistry *39*, 12989-12995.

Bratton, M. R., Pressler, M. A., and Hosler, J. P. (1999). Suicide Inactivation of Cytochrome c Oxidase: Catalytic Turnover in the Absence of Subunit III Alters the Active Site. Biochemistry *38*, 16236-16245.

Brookes, P. S. (2005). Mitochondrial H+ leak and ROS generation: An odd couple. Free Radical Biology & Medicine *38*, 12-23.

Brunger, A. T., Adams, P. D., Clore, G. M., DeLano, W. L., Gros, P., Grosse-Kunstleve, R. W., Jiang, J.-S., Kuszewski, J., Nilges, M., Pannu, N. S., *et al.* (1998). Crystallography & NMR System: a new software suite for macromolecular structure determination. Acta Crystallographica, Section D: Biological Crystallography *D54*, 905-921.

Brych, S. R., Blaber, S. I., Logan, T. M., and Blaber, M. (2001). Structure and stability effects of mutations designed to increase the primary sequence symmetry within the core region of a b-trefoil. Protein Science *10*, 2587-2599.

Buse, G., Soulimane, T., Dewor, M., Meyer, H. E., and Bluggel, M. (1999). Evidence for a copper-coordinated histidine-tyrosine crosslink in the active site of cytochrome oxidase. Protein Science *8*, 985-990.

Bushnell, G. W., Louie, G. V., and Brayer, G. D. (1990). High-resolution three-dimensional structure of horse heart cytochrome c. Journal of Molecular Biology *214*, 585-595.

Byrne, B., Abramson, J., Jansson, M., Holmgren, E., and Iwata, S. (2000). Fusion protein approach to improve the crystal quality of cytochrome bo3 ubiquinol oxidase from Escherichia coli. Biochimica et Biophysica Acta *1459*, 449-455.

Capaldi, R. A. (1990). Structure and function of cytochrome c oxidase. Annual Review of Biochemistry *59*, 569-596.

Chang, G., and Roth, C. B. (2001). Structure of MsbA from E. coli: A homolog of the multidrug resistance ATP binding cassette (ABC) transporters. Science (Washington, DC, United States) *293*, 1793-1800.

Cukier, R. I. (2004). Quantum molecular dynamics simulation of proton transfer in cytochrome c oxidase. Biochimica et Biophysica Acta *1656*, 189-202.

Cukier, R. I. (2005). A molecular dynamics study of water chain formation in the proton-conducting K channel of cytochrome c oxidase. Biochimica et Biophysica Acta *1706*, 134-146.

Daldal, F., Deshmukh, M., and Prince, R. C. (2003). Membrane-anchored cytochrome c as an electron carrier in photosynthesis and respiration: past, present and future of an unexpected discovery. Photosynthesis Research *76*, 127-134.

Daldal, F., Mandaci, S., Winterstein, C., Myllykallio, H., Duyck, K., and Zannoni, D. (2001). Mobile cytochrome c2 and membrane-anchored cytochrome cy are both efficient electron donors to the cbb3- and aa3-type cytochrome c oxidases during respiratory growth of Rhodobacter sphaeroides. Journal of Bacteriology *183*, 2013-2024.

Derewenda, Z. S. (2004). The use of recombinant methods and molecular engineering in protein crystallization. Methods (San Diego, CA, United States) *34*, 354-363.

Distler, A. M., Allison, J., Hiser, C., Qin, L., Hilmi, Y., and Ferguson-Miller, S. (2004). Mass spectrometric detection of protein, lipid and heme components of cytochrome c oxidase from R. sphaeroides and the stabilization of non-covalent complexes from the enzyme. European Journal of Mass Spectrometry *10*, 295-308.

Dowhan, W., Mileykovskaya, E., and Bogdanov, M. (2004). Diversity and versatility of lipid-protein interactions revealed by molecular genetic approaches. Biochimica et Biophysica Acta *1666*, 19-39.

Ferguson-Miller, S., and Babcock, G. T. (1996). Heme/Copper Terminal Oxidases. Chemical Reviews (Washington, D C) *96*, 2889-2907.

Ferguson-Miller, S., Brautigan, D. L., and Margoliash, E. (1978). Definition of cytochrome c binding domains by chemical modification. III. Kinetics of reaction of carboxydinitrophenyl cytochromes c with cytochrome c oxidase. Journal of Biological Chemistry *253*, 149-159.

Ferguson, A. D., Breed, J., Diederichs, K., Welte, W., and Coulton, J. W. (1998). An internal affinity-tag for purification and crystallization of the siderophore receptor FhuA, integral outer membrane protein from Escherichia coli K-12. Protein Science *7*, 1636-1638.

Ferguson, A. D., Hofmann, E., Coulton, J. W., Diederichs, K., and Welte, W. (1998). Siderophore-mediated iron transport: crystal structure of FhuA with bound lipopolysaccharide. Science (Washington, D C) *282*, 2215-2220.

Fetter, J., Sharpe, M., Qian, J., Mills, D., Ferguson-Miller, S., and Nicholls, P. (1996). Fatty acids stimulate activity and restore respiratory control in a proton channel mutant of cytochrome c oxidase. FEBS Letters *393*, 155-160.

Fetter, J. R., Qian, J., Shapleigh, J., Thomas, J. W., Garcia-Horsman, A., Schmidt, E., Hosler, J., Babcock, G. T., Gennis, R. B., and Ferguson-Miller, S. (1995). Possible proton relay pathways in cytochrome c oxidase. Proceedings of the National Academy of Sciences of the United States of America *92*, 1604-1608.

Flock, D., and Helms, V. (2002). Protein-protein docking of electron transfer complexes: cytochrome c oxidase and cytochrome c. Proteins: Structure, Function, and Genetics *47*, 75-85.

Florens, L., Schmidt, B., McCracken, J., and Ferguson-Miller, S. (2001). Fast Deuterium Access to the Buried Magnesium/Manganese Site in Cytochrome c Oxidase. Biochemistry *40*, 7491-7497.

Fromme, P., and Witt, H. T. (1998). Improved isolation and crystallization of Photosystem I for structural analysis. Biochimica et Biophysica Acta *1365*, 175-184.

Garavito, R. M., and Ferguson-Miller, S. (2001). Detergents as tools in membrane biochemistry. Journal of Biological Chemistry *276*, 32403-32406.

Garavito, R. M., and Picot, D. (1990). The art of crystallizing membrane proteins. Methods (San Diego, CA, United States) *1*, 57-69.

Gast, P., Hemelrijk, P., and Hoff, A. J. (1994). Determination of the number of detergent molecules associated with the reaction center protein isolated from the photosynthetic bacterium Rhodopseudomonas viridis. Effects of the amphiphilic molecule 1,2,3-heptanetriol. FEBS Letters *337*, 39-42.

Gilderson, G., Salomonsson, L., Aagaard, A., Gray, J., Brzezinski, P., and Hosler, J. (2003). Subunit III of cytochrome c oxidase of Rhodobacter sphaeroides is required to maintain rapid proton uptake through the D pathway at physiologic pH. Biochemistry *42*, 7400-7409.

Gohon, Y., and Popot, J.-L. (2003). Membrane protein-surfactant complexes. Current Opinion in Colloid & Interface Science *8*, 15-22.

Gordeliy, V. I., Labahn, J., Moukhametzianov, R., Efremov, R., Granzin, J., Schlesinger, R., Bueldt, G., Savopol, T., Scheidig, A. J., Klare, J. P., and Engelhard, M. (2002). Molecular basis of transmembrane signalling by sensory rhodopsin II-transducer complex. Nature (London, United Kingdom) *419*, 484-487.

Green, K., and Brand, M. D. (2004). The significance of uncoupling proteins in diabetes. Canadian Journal of Diabetes *28*, 50-58.

Haltia, T., Finel, M., Harms, N., Nakari, T., Raitio, M., Wikstrom, M., and Saraste, M. (1989). Deletion of the gene for subunit III leads to defective assembly of bacterial cytochrome oxidase. EMBO Journal *8*, 3571-3579.

Harper, M. E., Bevilacqua, L., Hagopian, K., Weindruch, R., and Ramsey, J. J. (2004). Ageing, oxidative stress, and mitochondrial uncoupling. Acta Physiologica Scandinavica *182*, 321-331.

Harrenga, A., and Michel, H. (1999). The cytochrome c oxidase from Paracoccus

denitrificans does not change the metal center ligation upon reduction. Journal of Biological Chemistry *274*, 33296-33299.

Haselkorn, R., Lapidus, A., Kogan, Y., Vlcek, C., Paces, J., Paces, V., Ulbrich, P., Pecenkova, T., Rebrekov, D., Milgram, A., *et al.* (2001). The Rhodobacter capsulatus genome. Photosynthesis Research *70*, 43-52.

Hilmi, Y. (2002) Use of mutagenesis, novel detergents, and lipid analysis to optimize conditions for achieving high resolution 3-dimensional crystal structure of Rhodobacter sphaeroides cytochrome c oxidase.

Hiser, C., Mills, D. A., Schall, M., and Ferguson-Miller, S. (2001). C-Terminal Truncation and Histidine-Tagging of Cytochrome c Oxidase Subunit II Reveals the Native Processing Site, Shows Involvement of the C-Terminus in Cytochrome c Binding, and Improves the Assay for Proton Pumping. Biochemistry *40*, 1606-1615.

Hofacker, I., and Schulten, K. (1998). Oxygen and proton pathways in cytochrome c oxidase. Proteins: Structure, Function, and Genetics *30*, 100-107.

Holm, L., and Sander, C. (1993). Protein structure comparison by alignment of distance matrixes. Journal of Molecular Biology *233*, 123-138.

Hosler, J. P. (2004). The influence of subunit III of cytochrome c oxidase on the D pathway, the proton exit pathway and mechanism-based inactivation in subunit I. Biochimica et Biophysica Acta *1655*, 332-339.

Hosler, J. P., Fetter, J., Tecklenburg, M. M. J., Espe, M., Lerma, C., and Ferguson-Miller, S. (1992). Cytochrome aa3 of Rhodobacter sphaeroides as a model for mitochondrial cytochrome c-oxidase. Purification, kinetics, proton pumping, and spectral analysis. Journal of Biological Chemistry *267*, 24264-24272.

Hunte, C., Koepke, J., Lange, C., Rossmanith, T., and Michel, H. (2000). Structure at 2.3.ANG. resolution of the cytochrome bc1 complex from the yeast Saccharomyces cerevisiae co-crystallized with an antibody Fv fragment. Structure (London) *8*, 669-684.

Imhoff, J. F. (1991). Polar lipids and fatty acids in the genus Rhodobacter. Systematic and Applied Microbiology *14*, 228-234.

Iverson, T. M., Luna-Chavez, C., Cecchini, G., and Rees, D. C. (1999). Structure of the Escherichia coli fumarate reductase respiratory complex. Science (Washington, D C) *284*, 1961-1966.

Iwata, S., Lee, J. W., Okada, K., Lee, J. K., Iwata, M., Rasmussen, B., Link, T. A., Ramaswamy, S., and Jap, B. K. (1998). Complete structure of the 11-subunit bovine mitochondrial cytochrome bc1 complex. Science (Washington, D C) *281*, 64-71.

Iwata, S., Ostermeier, C., Ludwig, B., and Michel, H. (1995). Structure at 2.8.ANG. resolution of cytochrome c oxidase from Paracoccus denitrificans. Nature (London) *376*, 660-669.

Kadenbach, B. (1986). Regulation of respiration and ATP synthesis in higher organisms: hypothesis. Journal of Bioenergetics and Biomembranes *18*, 39-54.

Kadenbach, B., and Arnold, S. (2000). 3,5-Diiodothyronine binds to subunit Va of cytochrome c oxidase: possible mechanism of short-term effects of thyroid hormones. Membrane Structure in Disease and Drug Therapy, 271-281.

Kadenbach, B., Jarausch, J., Hartmann, R., and Merle, P. (1983). Separation of mammalian cytochrome c oxidase into 13 polypeptides by a sodium dodecyl sulfate-gel electrophoretic procedure. Analytical Biochemistry *129*, 517-521.

Khademi, S., O'Connell, J., III, Remis, J., Robles-Colmenares, Y., Miercke, L. J. W., and Stroud, R. M. (2004). Mechanism of Ammonia Transport by Amt/MEP/Rh: Structure of AmtB at 1.35.ANG. Science (Washington, DC, United States) *305*, 1587-1594.

Kim, C. U., Kapfer, R., and Gruner, S. M. (2005). High-pressure cooling of protein crystals without cryoprotectants. Acta Crystallographica, Section D: Biological Crystallography *D61*, 881-890.

Kim, E., Chufan, E. E., Kamaraj, K., and Karlin, K. D. (2004). Synthetic Models for Heme-Copper Oxidases. Chemical Reviews (Washington, DC, United States) *104*, 1077-1133.

Kolbe, M., Besir, H., Essen, L.-O., and Oesterhelt, D. (2000). Structure of the light-driven chloride pump halorhodopsin at 1.8.ANG. resolution. Science (Washington, D C) *288*, 1390-1396.

Konstantinov, A. A., Siletsky, S., Mitchell, D., Kaulen, A., and Gennis, R. B. (1997). The roles of the two proton input channels in cytochrome c oxidase from Rhodobacter sphaeroides probed by the effects of site-directed mutations on time-resolved electrogenic intraprotein proton transfer. Proceedings of the National Academy of Sciences of the United States of America *94*, 9085-9090.

Krauss, S., Zhang, C.-Y., and Lowell, B. B. (2005). The mitochondrial uncoupling-protein homologues. Nature Reviews Molecular Cell Biology *6*, 248-261.

Kuo, A., Bowler, M. W., Zimmer, J., Antcliff, J. F., and Doyle, D. A. (2003). Increasing the diffraction limit and internal order of a membrane protein crystal by dehydration. Journal of Structural Biology *141*, 97-102.

Kwong, P. D., and Liu, Y. (1999). Use of cryoprotectants in combination with immiscible oils for flash cooling macromolecular crystals. Journal of Applied

Crystallography *32*, 102-105.

Landau, E. M., and Rosenbusch, J. P. (1996). Lipidic cubic phases: a novel concept for the crystallization of membrane proteins. Proceedings of the National Academy of Sciences of the United States of America *93*, 14532-14535.

Lange, C., Nett, J. H., Trumpower, B. L., and Hunte, C. (2001). Specific roles of protein-phospholipid interactions in the yeast cytochrome bc1 complex structure. EMBO Journal *20*, 6591-6600.

Larsen, R. W., Pan, L. P., Musser, S. M., Li, Z., and Chan, S. I. (1992). Could CuB be the site of redox linkage in cytochrome c oxidase? Proceedings of the National Academy of Sciences of the United States of America *89*, 723-727.

le Maire, M., Champeil, P., and Moller, J. V. (2000). Interaction of membrane proteins and lipids with solubilizing detergents. Biochimica et Biophysica Acta *1508*, 86-111.

Lee, H.-m., Das, T. K., Rousseau, D. L., Mills, D., Ferguson-Miller, S., and Gennis, R. B. (2000). Mutations in the Putative H-Channel in the Cytochrome c Oxidase from Rhodobacter sphaeroides Show That This Channel Is Not Important for Proton Conduction but Reveal Modulation of the Properties of Heme a. Biochemistry *39*, 2989-2996.

Link, T. A., and von Jagow, G. (1995). Zinc ions inhibit the QP center of bovine heart mitochondrial bc1 complex by blocking a protonatable group. Journal of Biological Chemistry *270*, 25001-25006.

Loll, P. J. (2003). Membrane protein structural biology: the high throughput challenge. Journal of Structural Biology *142*, 144-153.

Loll, P. J., Allaman, M., and Wiencek, J. (2001). Assessing the role of detergent-detergent interactions in membrane protein crystallization. Journal of Crystal Growth *232*, 432-438.

Ludwig, B., Bender, E., Arnold, S., Huttemann, M., Lee, I., and Kadenbach, B. (2001). Cytochrome C oxidase and the regulation of oxidative phosphorylation. Chembiochem: a European journal of chemical biology *2*, 392-403.

Luecke, H., Schobert, B., Richter, H.-T., Cartailler, J.-P., and Lanyi, J. K. (1999). Structure of bacteriorhodopsin at 1.55.ANG. resolution. Journal of Molecular Biology *291*, 899-911.

Ma, C., and Chang, G. (2004). Crystallography of the integral membrane protein EmrE from Escherichia coli. Acta Crystallographica, Section D: Biological Crystallography *D60*, 2399-2402.

MacMillan, F., Kannt, A., Behr, J., Prisner, T., and Michel, H. (1999). Direct Evidence

for a Tyrosine Radical in the Reaction of Cytochrome c Oxidase with Hydrogen Peroxide. Biochemistry *38*, 9179-9184.

Malatesta, F., Nicoletti, F., Zickermann, V., Ludwig, B., and Brunori, M. (1998). Electron entry in a CuA mutant of cytochrome c oxidase from Paracoccus denitrificans. Conclusive evidence on the initial electron entry metal center. FEBS Letters *434*, 322-324.

Maneg, O., Malatesta, F., Ludwig, B., and Drosou, V. (2004). Interaction of cytochrome c with cytochrome oxidase: two different docking scenarios. Biochimica et Biophysica Acta *1655*, 274-281.

Marone, P. A., Thiyagarajan, P., Wagner, A. M., and Tiede, D. M. (1999). Effect of detergent alkyl chain length on crystallization of a detergent-solubilized membrane protein: correlation of protein-detergent particle size and particle-particle interaction with crystallization of the photosynthetic reaction center from Rhodobacter sphaeroides. Journal of Crystal Growth *207*, 214-225.

McAuley, K. E., Fyfe, P. K., Ridge, J. P., Isaacs, N. W., Cogdell, R. J., and Jones, M. R. (1999). Structural details of an interaction between cardiolipin and an integral membrane protein. Proceedings of the National Academy of Sciences of the United States of America *96*, 14706-14711.

Michel, H. (1982). Three-dimensional crystals of a membrane protein complex. The photosynthetic reaction center from Rhodopseudomonas viridis. Journal of Molecular Biology *158*, 567-572.

Michel, H. (1999). Cytochrome c Oxidase: Catalytic Cycle and Mechanisms of Proton Pumping-A Discussion. Biochemistry *38*, 15129-15140.

Michel, H., Behr, J., Harrenga, A., and Kannt, A. (1998). Cytochrome c oxidase: structure and spectroscopy. Annual Review of Biophysics and Biomolecular Structure *27*, 329-356.

Mills, D. A., and Ferguson-Miller, S. (2003). Understanding the mechanism of proton movement linked to oxygen reduction in cytochrome c oxidase: lessons from other proteins. FEBS Letters *545*, 47-51.

Mills, D. A., Florens, L., Hiser, C., Qian, J., and Ferguson-Miller, S. (2000). Where is 'outside' in cytochrome c oxidase and how and when do protons get there? Biochimica et Biophysica Acta *1458*, 180-187.

Mills, D. A., Geren, L., Hiser, C., Schmidt, B., Durham, B., Millett, F., and Ferguson-Miller, S. (2005). An arginine to lysine mutation in the vicinity of the heme propionates affects the redox potentials of the hemes and associated electron and proton transfer in cytochrome c oxidase. Biochemistry *44*, 10457-10465.

Mills, D. A., and Hosler, J. P. (2005). Slow Proton Transfer through the Pathways for Pumped Protons in Cytochrome c Oxidase Induces Suicide Inactivation of the Enzyme. Biochemistry *44*, 4656-4666.

Mills, D. A., Schmidt, B., Hiser, C., Westley, E., and Ferguson-Miller, S. (2002). Membrane potential-controlled inhibition of cytochrome c oxidase by zinc. Journal of Biological Chemistry *277*, 14894-14901.

Mills, D. A., Tan, Z., Ferguson-Miller, S., and Hosler, J. (2003). A role for subunit III in proton uptake into the D pathway and a possible proton exit pathway in Rhodobacter sphaeroides cytochrome c oxidase. Biochemistry *42*, 7410-7417.

Murshudov, G. N., Vagin, A. A., and Dodson, E. J. (1997). Refinement of macromolecular structures by the maximum-likelihood method. Acta Crystallographica, Section D: Biological Crystallography *D53*, 240-255.

Myllykallio, H., Jenney, F. E., Jr., Moomaw, C. R., Slaughter, C. A., and Daldal, F. (1997). Cytochrome cy of Rhodobacter capsulatus is attached to the cytoplasmic membrane by an uncleaved signal sequence-like anchor. Journal of Bacteriology *179*, 2623-2631.

Myllykallio, H., Zannoni, D., and Daldal, F. (1999). The membrane-attached electron carrier cytochrome cy from Rhodobacter sphaeroides is functional in respiratory but not in photosynthetic electron transfer. Proceedings of the National Academy of Sciences of the United States of America *96*, 4348-4353.

Napiwotzki, J., Shinzawa-Itoh, K., Yoshikawa, S., and Kadenbach, B. (1997). ATP and ADP bind to cytochrome c oxidase and regulate its activity. Biological Chemistry *378*, 1013-1021.

O'Neill, J. W., Kim, D. E., Baker, D., and Zhang, K. Y. J. (2001). Structures of the B1 domain of protein L from Peptostreptococcus magnus with a tyrosine to tryptophan substitution. Acta Crystallographica, Section D: Biological Crystallography *D57*, 480-487.

Okada, T., Fujiyoshi, Y., Silow, M., Navarro, J., Landau, E. M., and Shichida, Y. (2002). Functional role of internal water molecules in rhodopsin revealed by x-ray crystallography. Proceedings of the National Academy of Sciences of the United States of America *99*, 5982-5987.

Ostermeier, C., Harrenga, A., Ermler, U., and Michel, H. (1997). Structure at 2.7.ANG. resolution of the Paracoccus denitrificans two-subunit cytochrome c oxidase complexed with an antibody Fv fragment. Proceedings of the National Academy of Sciences of the United States of America *94*, 10547-10553.

Ostermeier, C., Iwata, S., Ludwig, B., and Michel, H. (1995). Fv fragment-mediated crystallization of the membrane protein bacterial cytochrome c oxidase. Nature

Structural Biology *2*, 842-846.

Otwinowski, Z., and Minor, W. (1997). Processing of x-ray diffraction data collected in oscillation mode. Methods in Enzymology *276*, 307-326.

Paddock, M. L., Graige, M. S., Feher, G., and Okamura, M. Y. (1999). Identification of the proton pathway in bacterial reaction centers: inhibition of proton transfer by binding of Zn2+ or Cd2+. Proceedings of the National Academy of Sciences of the United States of America *96*, 6183-6188.

Pan, L. P., Hibdon, S., Liu, R. Q., Durham, B., and Millett, F. (1993). Intracomplex electron transfer between ruthenium-cytochrome c derivatives and cytochrome c oxidase. Biochemistry *32*, 8492-8498.

Pautsch, A., Vogt, J., Model, K., Siebold, C., and Schulz, G. E. (1999). Strategy for membrane protein crystallization exemplified with OmpA and OmpX. Proteins: Structure, Function, and Genetics *34*, 167-172.

Peiffer, W. E., Ingle, R. T., and Ferguson-Miller, S. (1990). Structurally unique plant cytochrome c oxidase isolated from wheat germ, a rich source of plant mitochondrial enzymes. Biochemistry *29*, 8696-8701.

Proshlyakov, D. A., Pressler, M. A., and Babcock, G. T. (1998). Dioxygen activation and bond cleavage by mixed-valence cytochrome c oxidase. Proceedings of the National Academy of Sciences of the United States of America *95*, 8020-8025.

Qian, J., Mills, D. A., Geren, L., Wang, K., Hoganson, C. W., Schmidt, B., Hiser, C., Babcock, G. T., Durham, B., Millett, F., and Ferguson-Miller, S. (2004). Role of the Conserved Arginine Pair in Proton and Electron Transfer in Cytochrome c Oxidase. Biochemistry *43*, 5748-5756.

Ramirez, B. E., Malmstrom, B. G., Winkler, J. R., and Gray, H. B. (1995). The currents of life: the terminal electron-transfer complex of respiration. Proceedings of the National Academy of Sciences of the United States of America *92*, 11949-11951.

Regan, J. J., Ramirez, B. E., Winkler, J. R., Gray, H. B., and Malmstrom, B. G. (1998). Pathways for electron tunneling in cytochrome c oxidase. Journal of Bioenergetics and Biomembranes *30*, 35-39.

Rich, P. R., Meunier, B., Mitchell, R., and Moody, A. J. (1996). Coupling of charge and proton movement in cytochrome c oxidase. Biochimica et Biophysica Acta *1275*, 91-95.

Roberts, V. A., and Pique, M. E. (1999). Definition of the interaction domain for cytochrome c on cytochrome c oxidase.: III. Prediction of the docked complex by a complete, systematic search. Journal of Biological Chemistry *274*, 38051-38060.

Robinson, B. H. (2000). Human cytochrome oxidase deficiency. Pediatric Research *48*, 581-585.

Robinson, N. C. (1982). Specificity and binding affinity of phospholipids to the high-affinity cardiolipin sites of beef heart cytochrome c oxidase. Biochemistry *21*, 184-188.

Rosenow, M. A., Brune, D., and Allen, J. P. (2003). The influence of detergents and amphiphiles on the solubility of the light-harvesting I complex. Acta Crystallographica, Section D: Biological Crystallography *D59*, 1422-1428.

Roujeinikova, A., Raasch, C., Burke, J., Baker, P. J., Liebl, W., and Rice, D. W. (2001). The Crystal Structure of Thermotoga maritima Maltosyltransferase and its Implications for the Molecular Basis of the Novel Transfer Specificity. Journal of Molecular Biology *312*, 119-131.

Roujeinikova, A., Raasch, C., Sedelnikova, S., Liebl, W., and Rice, D. W. (2002). Crystal structure of Thermotoga maritima 4-a-glucanotransferase and its acarbose complex: implications for substrate specificity and catalysis. Journal of Molecular Biology *321*, 149-162.

Sack, J. S., and Quiocho, F. A. (1997). CHAIN: A crystallographic modeling program. Methods in Enzymology *277*, 158-173.

Schagger, H., Hagen, T., Roth, B., Brandt, U., Link, T. A., and von Jagow, G. (1990). Phospholipid specificity of bovine heart bc1 complex. European journal of biochemistry / FEBS *190*, 123-130.

Schmidt, B., McCracken, J., and Ferguson-Miller, S. (2003). A discrete water exit pathway in the membrane protein cytochrome c oxidase. Proceedings of the National Academy of Sciences of the United States of America *100*, 15539-15542.

Seddon, A. M., Curnow, P., and Booth, P. J. (2004). Membrane proteins, lipids and detergents: not just a soap opera. Biochimica et Biophysica Acta *1666*, 105-117.

Sedlak, E., and Robinson, N. C. (1999). Phospholipase A2 Digestion of Cardiolipin Bound to Bovine Cytochrome c Oxidase Alters Both Activity and Quaternary Structure. Biochemistry *38*, 14966-14972.

Seibold, S. A., Mills, D. A., Ferguson-Miller, S., and Cukier, R. I. (2005). Water Chain Formation and Possible Proton Pumping Routes in Rhodobacter sphaeroides Cytochrome c Oxidase: A Molecular Dynamics Comparison of the Wild Type and R481K Mutant. Biochemistry *44*, 10475-10485.

Shapleigh, J. P., and Gennis, R. B. (1992). Cloning, sequencing and deletion from the chromosome of the gene encoding subunit I of the aa3-type cytochrome c oxidase of Rhodobacter sphaeroides. Molecular Microbiology *6*, 635-642.

Sharpe, M., Perin, I., Wrigglesworth, J., and Nicholls, P. (1996). Fatty acids as modulators of cytochrome c oxidase in proteoliposomes. Biochemical Journal *320*, 557-561.

Sharpe, M., Qin, L., and Ferguson-Miller, S. (2005). Proton entry, exit and pathways in cytochrome oxidase: Insight from "Conserved" Water, In Biophysical and Structural Aspects of Bioenergetics, M. Wikstroem, ed. (Cambridge, accepted: Royal Society of Chemistry).

Shinzawa-Itoh, K., Ueda, H., Yoshikawa, S., Aoyama, H., Yamashita, E., and Tsukihara, T. (1995). Effects of ethyleneglycol chain length of dodecyl polyethyleneglycol monoether on the crystallization of bovine heart cytochrome c oxidase. Journal of Molecular Biology *246*, 572-575.

Smith, P. K., Krohn, R. I., Hermanson, G. T., Mallia, A. K., Gartner, F. H., Provenzano, M. D., Fujimoto, E. K., Goeke, N. M., Olson, B. J., and Klenk, D. C. (1985). Measurement of protein using bicinchoninic acid. Analytical Biochemistry *150*, 76-85.

Snijder, H. J., Van Eerde, J. H., Kingma, R. L., Kalk, K. H., Dekker, N., Egmond, M. R., and Dijkstra, B. W. (2001). Structural investigations of the active-site mutant Asn156Ala of outer membrane phospholipase A: Function of the Asn-His interaction in the catalytic triad. Protein Science *10*, 1962-1969.

Steffens, G. C. M., Soulimane, T., Wolff, G., and Buse, G. (1993). Stoichiometry and redox behavior of metals in cytochrome-c oxidase. European Journal of Biochemistry *213*, 1149-1157.

Steinrucke, P., Steffens, G. C., Panskus, G., Buse, G., and Ludwig, B. (1987). Subunit II of cytochrome c oxidase from Paracoccus denitrificans. DNA sequence, gene expression and the protein. European journal of biochemistry / FEBS *167*, 431-439.

Stock, D., Leslie, A. G. W., and Walker, J. E. (1999). Molecular architecture of the rotary motor in ATP synthase. Science (Washington, D C) *286*, 1700-1705.

Storoni, L. C., McCoy, A. J., and Read, R. J. (2004). Likelihood-enhanced fast rotation functions. Acta Crystallographica, Section D: Biological Crystallography *D60*, 432-438.

Stroebel, D., Choquet, Y., Popot, J.-L., and Picot, D. (2003). An atypical haem in the cytochrome b6f complex. Nature (London, United Kingdom) *426*, 413-418.

Sui, H., Han, B.-G., Lee, J. K., Walian, P., and Jap, B. K. (2001). Structural basis of water-specific transport through the aqp1 water channel. Nature (London, United Kingdom) *414*, 872-878.

Svensson-Ek, M., Abramson, J., Larsson, G., Tornroth, S., Brzezinski, P., and Iwata, S.

(2002). The X-ray Crystal Structures of Wild-type and EQ(I-286) Mutant Cytochrome c Oxidases from Rhodobacter sphaeroides. Journal of Molecular Biology *321*, 329-339.

Tajkhorshid, E., Nollert, P., Jensen, M. O., Miercke, L. J. W., O'Connell, J., Stroud, R. M., and Schulten, K. (2002). Control of the selectivity of the aquaporin water channel family by global orientational tuning. Science (Washington, DC, United States) *296*, 525-530.

Tan, M.-L., Balabin, I., and Onuchic, J. N. (2004). Dynamics of electron transfer pathways in cytochrome c oxidase. Biophysical Journal *86*, 1813-1819.

Timmins, P. A., Hauk, J., Wacker, T., and Welte, W. (1991). The influence of heptane-1,2,3-triol on the size and shape of LDAO micelles. Implications for the crystallization of membrane proteins. FEBS Letters *280*, 115-120.

Tomson, F., Bailey, J. A., Gennis, R. B., Unkefer, C. J., Li, Z., Silks, L. A., Martinez, R. A., Donohoe, R. J., Dyer, R. B., and Woodruff, W. H. (2002). Direct Infrared Detection of the Covalently Ring Linked His-Tyr Structure in the Active Site of the Heme-Copper Oxidases. Biochemistry *41*, 14383-14390.

Tomson, F. L., Morgan, J., Gu, G., Barquera, B., Vygodina, T. V., and Gennis, R. B. (2003). Substitutions for Glutamate 101 in Subunit II of Cytochrome c Oxidase from Rhodobacter sphaeroides Result in Blocking the Proton-Conducting K-Channel. Biochemistry *42*, 1711-1717.

Torres, J., Stevens, T. J., and Samso, M. (2003). Membrane proteins: the \"Wild West\" of structural biology. Trends in Biochemical Sciences *28*, 137-144.

Toyoshima, C., Nakasako, M., Nomura, H., and Ogawa, H. (2000). Crystal structure of the calcium pump of sarcoplasmic reticulum at 2.6.ANG. resolution. Nature (London) *405*, 647-655.

Trakhanov, S., Kreimer, D. I., Parkin, S., Ames, G. F.-L., and Rupp, B. (1998). Cadmium-induced crystallization of proteins: II. Crystallization of the Salmonella typhimurium histidine-binding protein in complex with L-histidine, L-arginine, or L-lysine. Protein Science *7*, 600-604.

Trakhanov, S., and Quiocho, F. A. (1995). Influence of divalent cations in protein crystallization. Protein Science *4*, 1914-1919.

Tsukihara, T., Aoyama, H., Yamashita, E., Tomizaki, T., Yamaguchi, H., Shinzawa-Itoh, K., Nakashima, R., Yaono, R., and Yoshikawa, S. (1995). Structures of metal sites of oxidized bovine heart cytochrome c oxidase at 2.8.ANG. Science (Washington, D C) *269*, 1069-1074.

Tsukihara, T., Aoyama, H., Yamashita, E., Tomizaki, T., Yamaguchi, H.,

Shinzawa-Itoh, K., Nakashima, R., Yaono, R., and Yoshikawa, S. (1996). The whole structure of the 13-subunit oxidized cytochrome c oxidase at 2.8.ANG. Science (Washington, D C) *272*, 1136-1144.

Tsukihara, T., Shimokata, K., Katayama, Y., Shimada, H., Muramoto, K., Aoyama, H., Mochizuki, M., Shinzawa-itoh, K., Yamashita, E., Yao, M., *et al.* (2003). The low-spin heme of cytochrome c oxidase as the driving element of the proton-pumping process. Proceedings of the National Academy of Sciences of the United States of America *100*, 15304-15309.

Vygodina, T. V., Capitanio, N., Papa, S., and Konstantinov, A. A. (1997). Proton pumping by cytochrome c oxidase is coupled to peroxidase half of its catalytic cycle. FEBS Letters *412*, 405-409.

Wang, K., Geren, L., Zhen, Y., Ma, L., Ferguson-Miller, S., Durham, B., and Millett, F. (2002). Mutants of the CuA site in cytochrome c oxidase of Rhodobacter sphaeroides: II. Rapid kinetic analysis of electron transfer. Biochemistry *41*, 2298-2304.

Wang, K., Zhen, Y., Sadoski, R., Grinnell, S., Geren, L., Ferguson-Miller, S., Durham, B., and Millett, F. (1999). Definition of the interaction domain for cytochrome c on cytochrome c oxidase.: II. Rapid kinetic analysis of electron transfer from cytochrome c to Rhodobacter sphaeroides cytochrome oxidase surface mutants. Journal of Biological Chemistry *274*, 38042-38050.

White, S. H. (2004). The progress of membrane protein structure determination. Protein Science *13*, 1948-1949.

Wiener, M. C., and Snook, C. F. (2001). The development of membrane protein crystallization screens based upon detergent solution properties. Journal of Crystal Growth *232*, 426-431.

Wikstrom, M., Bogachev, A., Finel, M., Morgan, J. E., Puustinen, A., Raitio, M., Verkhovskaya, M., and Verkhovsky, M. I. (1994). Mechanism of proton translocation by the respiratory oxidases. The histidine cycle. Biochimica et Biophysica Acta *1187*, 106-111.

Wikstrom, M., and Verkhovsky, M. I. (2002). Proton translocation by cytochrome c oxidase in different phases of the catalytic cycle. Biochimica et Biophysica Acta *1555*, 128-132.

Wikstrom, M. K. (1977). Proton pump coupled to cytochrome c oxidase in mitochondria. Nature *266*, 271-273.

Winkler, J. R., Malmstroem, B. G., and Gray, H. B. (1995). Rapid electron injection into multisite metalloproteins: intramolecular electron transfer in cytochrome oxidase. Biophysical Chemistry *54*, 199-209.

Winn, M. D., Isupov, M. N., and Murshudov, G. N. (2001). Use of TLS parameters to model anisotropic displacements in macromolecular refinement. Acta Crystallographica, Section D: Biological Crystallography *D57*, 122-133.

Witt, H., and Ludwig, B. (1997). Isolation, analysis, and deletion of the gene coding for subunit IV of cytochrome c oxidase in Paracoccus denitrificans. Journal of Biological Chemistry *272*, 5514-5517.

Witt, H., Malatesta, F., Nicoletti, F., Brunori, M., and Ludwig, B. (1998). Tryptophan 121 of subunit II is the electron entry site to cytochrome-c oxidase in Paracoccus denitrificans. Involvement of a hydrophobic patch in the docking reaction. Journal of Biological Chemistry *273*, 5132-5136.

Yau, W.-M., Wimley, W. C., Gawrisch, K., and White, S. H. (1998). The Preference of Tryptophan for Membrane Interfaces. Biochemistry *37*, 14713-14718.

Yoshikawa, S., Shinzawa-itoh, K., Nakashima, R., Yaono, R., Yamashita, E., Inoue, N., Yao, M., Fei, M. J., Libeu, C. P., Mizushima, T., *et al.* (1998). Redox-coupled crystal structural changes in bovine heart cytochrome c oxidase. Science (Washington, D C) *280*, 1723-1729.

Yu, C.-A., and Yu, L. (1980). Structural role of phospholipids in ubiquinol-cytochrome c reductase. Biochemistry *19*, 5715-5720.

Zaslavsky, D., and Gennis, R. B. (2000). Proton pumping by cytochrome oxidase: progress, problems and postulates. Biochimica et Biophysica Acta *1458*, 164-179.

Zhang, H., Kurisu, G., Smith, J. L., and Cramer, W. A. (2003). A defined protein-detergent-lipid complex for crystallization of integral membrane proteins: The cytochrome b6f complex of oxygenic photosynthesis. Proceedings of the National Academy of Sciences of the United States of America *100*, 5160-5163.

Zhang, Z., Huang, L., Shulmeister, V. M., Chi, Y.-I., Kim, K. K., Hung, L.-W., Crofts, A. R., Berry, E. A., and Kim, S.-H. (1998). Electron transfer by domain movement in cytochrome bc1. Nature (London) *392*, 677-684.

Zhen, Y., Hoganson, C. W., Babcock, G. T., and Ferguson-Miller, S. (1999). Definition of the interaction domain for cytochrome c on cytochrome c oxidase: I. Biochemical, spectral, and kinetic characterization of surface mutants in subunit II of Rhodobacter sphaeroides cytochrome aa3. Journal of Biological Chemistry *274*, 38032-38041.

Zhen, Y., Qian, J., Follmann, K., Hayward, T., Nilsson, T., Dahn, M., Hilmi, Y., Hamer, A. G., Hosler, J. P., and Ferguson-Miller, S. (1998). Overexpression and purification of cytochrome c oxidase from Rhodobacter sphaeroides. Protein Expression and Purification *13*, 326-336.

Zhen, Y., Schmidt, B., Kang, U. G., Antholine, W., and Ferguson-Miller, S. (2002).

Mutants of the CuA site in cytochrome c oxidase of Rhodobacter sphaeroides: I. Spectral and functional properties. Biochemistry *41*, 2288-2297.

Zhou, T., Radaev, S., Rosen, B. P., and Gatti, D. L. (2000). Structure of the ArsA ATPase: the catalytic subunit of a heavy metal resistance pump. EMBO Journal *19*, 4838-4845.

Zhou, Y., Morals-Cabral, J. H., Kaufman, A., and MacKinnon, R. (2001). Chemistry of ion coordination and hydration revealed by a K+ channel-Fab complex at 2.0.ANG resolution. Nature (London, United Kingdom) *414*, 43-48.